Formulation and evaluation of finite element discretization schemes for high Reynolds number incompressible fluid flows

by

Juan Pablo Pontaza

B.S. in Mechanical Engineering, Texas A&M University (1999)

Submitted to the Department of Mechanical Engineering
in partial fulfillment of the requirements for the degree of

Master of Science in Mechanical Engineering

at the

MASSACHUSETTS INSTITUTE OF TECHNOLOGY

May 2001 [June 2001]

Author .....
Department of Mechanical Engineering
May 23, 2001

Certified by .....
Klaus-Jürgen Bathe
Professor
Thesis Supervisor

Accepted by .....
Ain A. Sonin
Chairman, Department Committee on Graduate Students

Formulation and evaluation of finite element discretization schemes for high Reynolds number incompressible fluid flows

by

Juan Pablo Pontaza

Submitted to the Department of Mechanical Engineering
on May 23, 2001, in partial fulfillment of the
requirements for the degree of
Master of Science in Mechanical Engineering

Abstract

Four finite element procedures for the analysis of high Reynolds number incompressible fluid flows are presented. The procedures are developed in detail for two-dimensional analysis and are based on the use of the mixed 9-node element, optimal for incompressible analysis (the 9/3 and 9/4-c elements). In the first procedure the Navier-Stokes equations are discretized using the local analytic solution of the advection-diffusion equation, while the incompressibility constraint (the continuity equation) is enforced in a weighted residual fashion. The other three procedures are based on Petrov-Galerkin formulations for the Navier-Stokes equations. These procedures differ from each other in the way the test functions are established. Here we consider two approaches. In the first approach the test functions are endowed with properties of the local analytic solution of the advection-diffusion equation. The test functions respond to the flow conditions and give more weight to upstream nodes, the amount of weighting and upstream direction being completely determined by the local analytic properties. In the second approach the test functions are obtained by taking the tensor product of exponential functions along the element edge- and midlines. For low Reynolds number these test functions collapse to the usual biquadratic functions, and as the Reynolds number increases they automatically skew in the upstream direction to provide the necessary stability. An important feature of all the procedures considered here is that no artificial constants or tunable parameters need to be used or set. The capability of the formulations is demonstrated in the solution of several test problems.

Thesis Supervisor: Klaus-Jürgen Bathe
Title: Professor

Acknowledgments

I would like to take this opportunity to thank my supervisor, Prof. K. J. Bathe, for the patience, guidance, and support that he has extended towards me during the course of this research. His critical reviews of my work and his dedication to teaching made my graduate studies at MIT an enjoyable and rewarding experience.

I would like to thank my mother, Dalila de Pontaza, for her support and encouragement throughout my academic life. I thank my wife, María José, for her love and encouragement which allowed me to remain focused on my research. Finally, I thank my colleagues at the MIT Finite Element Research Laboratory for the many fruitful discussions throughout the course of my research.

Contents

List of Figures

List of Tables

Chapter 1

Introduction

1.1 Background

Computational fluid dynamics (CFD) is beginning to play a major role in the analysis and design of engineering systems. In some CFD circles the finite element method has not yet achieved the same level of acceptance as other numerical solution schemes, such as finite difference and control volume based methods. This is probably partly due to the fact that the finite element method originated in the field of solid mechanics. Indeed, it is well known that finite element procedures are optimal for elliptic problems and can be applied for arbitrarily complex geometries.

Much effort has been directed towards the development of effective and efficient finite element procedures for the solution of fluid flow problems. However, to date, most fluid flow analyses are being performed using finite difference methods with body-fitted coordinate transformations and control volume methods, the latter being a low-order weighted residual method for approximating the solution via local conservation. While it is recognized that finite element procedures have a strong mathematical basis, it has also been established that they are not computationally as efficient. However, largely low-order finite elements have been used.

In the finite element solution of incompressible fluid flows, using the Bubnov-Galerkin formulation in which the test and trial functions are the same, there are two main sources of potential numerical instabilities. The first is due to inappropriate

discretization of the convection term. The Bubnov-Galerkin formulation treats the convection term symmetrically, which can result in spurious node-to-node oscillations if the discretization scale is too large to resolve subgrid phenomena, in particular boundary layers. Such oscillations become significant as the Reynolds number increases. They can be suppressed by refining the mesh, but the necessary degree of refinement is often prohibitive. Also, in many cases, it may not be necessary to resolve all boundary layers present.

Various finite element procedures have been proposed to eliminate this numerical instability, starting in the 1970s when Christie et al. [1] proposed a stable scheme for the one-dimensional, steady-state advection-diffusion equation without source terms. The stabilization was controlled to give the analytic nodal solution for the one-dimensional case. The scheme was based on the Petrov-Galerkin formulation, in which the trial and test functions are different and the test functions would give more weight to upstream nodes. Shortly after, Heinrich et al. [2] proposed a two-dimensional scheme, which was a straightforward extension of Christie's earlier work. The scheme applied one-dimensional stabilization along the edges of the two-dimensional element. However, several difficulties were encountered with this generalization of the scheme to multi-dimensions. These were attributed to cross-wind diffusion, which manifests itself when the flow is skewed to the mesh lines. Moreover, when the scheme was applied to more complicated situations (transient problems and/or when source terms were present) it was found to be far from optimal, and in many instances the Bubnov-Galerkin formulation would give more accurate results [3].

In the 1980s Brooks and Hughes [3] introduced the SUPG (Streamline Upwind Petrov Galerkin) scheme for piecewise linear elements, which reduced the oscillations by adding an artificial diffusion term in the streamline direction. Later, Hughes et al. [4] generalized the formulation by adding the least-squares form of residuals to the Galerkin formulation. The Galerkin/Least-Squares (GLS) formulation coincides with the SUPG scheme for the hyperbolic case. Test results using the SUPG, GLS, and a higher order artificial diffusion method embedded in parabolic elements are given by Hendriana and Bathe [5], where shortcomings of these methods are demonstrated.

The amount of the artificial diffusion introduced in the streamline direction in the SUPG scheme is tuned by a parameter τ, but a suitable argument to guide the proper choice of τ was still lacking. Brezzi et al. [6, 7] translated the problem of choosing the optimal τ to that of finding the volume of a suitable bubble function in the approach called the residual-free bubbles method. The bubble function is obtained by solving a boundary value problem with homogeneous essential boundary conditions on each element.

The second source of numerical instability is due to inappropriate enforcement of the incompressibility condition, or in other words an inappropriate combination of interpolation functions for the velocity and pressure. This instability does not arise if the combination satisfies the *inf-sup* condition [8], and indeed optimal elements are available. Considering two-dimensional flow, the mixed-interpolated 9-node velocity-based elements with either a linear discontinuous pressure interpolation (the 9/3 element) or a bilinear pressure interpolation (the 9/4-c element) are optimal [9], and hence very attractive candidates for a solution procedure.

1.2 Present work

While much research has been conducted to develop stable finite element schemes for high Reynolds number flow, an evaluation of available schemes has shown that major advances are still needed in the field [5]. The objective of this work is to present new procedures to treat high Reynolds number incompressible flow. These procedures are described in detail and evaluated for the case of two-dimensional flow.

We use elements that are optimal in performance regarding the incompressibility constraint – (the 9/3 and 9/4-c elements) – and concentrate on the first source of numerical instability. The first proposed formulation uses the local analytic solution of the two-dimensional advection-diffusion equation to suppress this instability. The procedure uses the local analytic solution directly to discretize the momentum equations, while the incompressibility constraint (the continuity equation) is enforced using the standard Galerkin approach.

The other three formulations can be classified as Petrov-Galerkin formulations, in which the test functions are different from the trial functions and the test functions give more weight to upstream nodes. In the first two of the three Petrov-Galerkin formulations, the test functions are endowed with properties from the local analytic solution of the advection-diffusion equation. The enhanced test functions inherit the ability to respond to the flow conditions. In the case of pure diffusion the test function will be symmetric, giving equal weight to the surrounding nodes. If convection is present the test function will skew as to give more weight to upstream nodes, the upstream direction and amount of weight given to upstream nodes being determined completely by the local analytic properties. Cross-wind diffusion does not seem to be a problem because the test functions inherit the ability to automatically respond to any skewed velocity vector.

In the last of the three Petrov-Galerkin formulations the test functions are established by taking the tensor product of exponential functions that respond to the flow conditions along the edge- and mid-lines of the element. For low Reynolds number these test functions conveniently collapse to the usual biquadratic functions, and as the Reynolds number increases they automatically skew in the upstream direction to provide the necessary stability. Hence, this solutions scheme is a simple and natural extension of a procedure known to be optimal for low Reynolds number flow solutions.

An important and salient feature of all the procedures considered here is that no artificial constants or tunable parameters need to be used or set. The schemes result in consistent formulations and we demonstrate their performance by numerically solving several test problems.

The thesis is organized as follows. In Chapter 2, we derive the governing equations for incompressible fluid flow using a continuum hypothesis and discuss their behavior in the limiting cases in terms of the Reynolds number. We quote results regarding the self-consistency of the deterministic equations in terms of the Reynolds number to establish a validity domain where we expect the stabilized numerical schemes to work. We then derive the variational form of the governing equations and review some classic mathematical work on existence and uniqueness of weak solutions.

In Chapter 3, we present local analytic procedures as means to develop numerical schemes for high Reynolds number fluid flows and give details of four discretization schemes based on such procedures. In Chapter 4, solutions of several test problems are shown to demonstrate the capabilities of the proposed schemes. We compare our results with available/benchmark solutions. Finally in Chapter 5, conclusions and recommendations for future research are given.

Chapter 2

Governing equations

2.1 Introduction

In this chapter we derive the incompressible Navier-Stokes equations based on the conservation of mass and Newton's second law. In doing so, we assume that the volume of each fluid particle is infinitely small compared to the whole volume occupied by the fluid. This assumption forms the basis of the *continuum hypothesis*. Under this hypothesis we consider the fluid particle to be a *material point* and the density (and other properties) of the fluid to be continuous functions of space and time. We present the dimensionless form of the equations and comment on their high Reynolds number behavior. We then formally state the initial, boundary-value problem of the incompressible Navier-Stokes equations and quote results regarding the validity domain of the continuum hypothesis in terms of the Reynolds number. We develop the variational form of the equations, which we will use as a starting point for the finite element discretization using the proposed numerical schemes, and discuss the existence and uniqueness of weak solutions.

To formulate the conservation laws we identify a cluster of molecules contained in a control volume. The control volume always consists of the same fluid particles (material points) and its volume is therefore a material volume. The material volume is deformed in time and translated according to the local velocity $\mathbf{u}(\mathbf{x}, t)$ of the flow. We denote by $\Omega(t)$ the volume that is occupied by the cluster of molecules at time t.

Assuming a continuum, we consider an arbitrary function $f(\mathbf{x}, t)$ to be a continuous function of position. The rate of change of the material integrals are conveniently evaluated by means of the Reynolds transport theorem:

$$\begin{aligned}\frac{D}{Dt}\int_{\Omega(t)} f(\mathbf{x},t)\, d\Omega &= \int_{\Omega} \frac{\partial f}{\partial t} + \mathbf{u}\cdot\nabla f + f\,(\nabla\cdot\mathbf{u})\, d\Omega \\ &= \int_{\Omega} \frac{\partial f}{\partial t} + \nabla\cdot(f\mathbf{u})\, d\Omega \end{aligned} \tag{2.1}$$

If $f(\mathbf{x}, t)$ is a tensor field of any degree, which together with its partial derivatives is continuous in Ω, then the Gauss divergence theorem holds and

$$\int_{\Omega} \nabla\cdot(f\mathbf{u})\, d\Omega = \int_{\Gamma} f\mathbf{u}\cdot\mathbf{n}\, d\Gamma$$

where Γ is the directional surface bounding Ω and $\mathbf{n}$ is the outwardly positive unit normal to this surface.

Equation 2.1 relates the rate of change of the material volume integral to the rate of change of the quantity $f(\mathbf{x}, t)$ integrated over a fixed volume Ω, which coincides with the varying volume $\Omega(t)$ at time t, and to the flux of the quantity $f(\mathbf{x}, t)$ through the bounding surfaces. Physically, it relates the total rate of change of the field quantity $f(\mathbf{x}, t)$ integrated over a control volume Ω to its time rate of change within the control volume and to its net rate of flux through the control surface.

2.2 Navier-Stokes equations for incompressible flow

The Navier-Stokes equations are based on the conservation of mass and on Newton's second law. In addition, the more specific assumption of a Newtonian fluid is adopted, which is justified in many cases of hydrodynamic flows.

2.2.1 Conservation of Mass

Let $\rho(\mathbf{x}, t)$ denote the mass density. Then we can write the mass as the integral of the density over the material volume, which must remain constant in time

$$\frac{D}{Dt} \int_{\Omega(t)} \rho(\mathbf{x}, t)\, d\Omega = 0 \tag{2.2}$$

Making use of (2.1) we change the conservation law to the form

$$\int_{\Omega} \frac{\partial \rho}{\partial t} + \nabla \cdot (\rho \mathbf{u})\, d\Omega = 0 \tag{2.3}$$

This equation holds for every volume that could be occupied by the fluid, that is, for arbitrary choice of Ω. We can therefore shrink the integration region to a point and conclude that the continuous integrand must itself vanish at every $\mathbf{x}$. Thus we are led to the *differential form* of the conservation of mass

$$\frac{\partial \rho}{\partial t} + \nabla \cdot (\rho \mathbf{u}) = 0 \tag{2.4}$$

If we use the material derivative we obtain

$$\frac{D\rho}{Dt} + \rho\, (\nabla \cdot \mathbf{u}) = 0 \tag{2.5}$$

Furthermore, if

$$\frac{D\rho}{Dt} = \frac{\partial \rho}{\partial t} + \mathbf{u} \cdot \nabla \rho = 0 \tag{2.6}$$

holds, then the density of a single material particle does not vary during its motion. This leads to the *incompressibility* condition

$$\nabla \cdot \mathbf{u} = 0 \tag{2.7}$$

If (2.6) is satisfied, the continuity equation takes on the simpler form (2.7) where no derivatives with respect to time appears, but which nevertheless holds for unsteady

flows.

Note that equation (2.3) can also be written as

$$\frac{\partial}{\partial t}\int_{\Omega}\rho\, d\Omega = -\int_{\Gamma}\rho\mathbf{u}\cdot\mathbf{n}\, d\Gamma \tag{2.8}$$

which we physically interpret as follows: the rate of change of the mass in the control volume is equal to the difference between the mass entering and leaving through the surface of the control volume per unit time. This very obvious interpretation often serves as a starting point for the explanation of mass conservation. If $\partial\rho/\partial t = 0$, the integral form of the continuity equation reads:

$$\int_{\Gamma}\rho\mathbf{u}\cdot\mathbf{n}\, d\Gamma = 0 \tag{2.9}$$

i.e., just as much mass enters as leaves the control volume per unit time.

2.2.2 Balance of momentum

In an inertial frame the rate of change of the momentum of the body is balanced by the force applied on this body:

$$\frac{D}{Dt}\int_{\Omega(t)}\rho\,\mathbf{u}\, d\Omega = \int_{\Omega(t)}\rho\,\mathbf{f}\, d\Omega + \int_{\Gamma(t)}\boldsymbol{\sigma}\cdot\mathbf{n}\, d\Gamma \tag{2.10}$$

where $\mathbf{f}$ is an external volume force density and $\boldsymbol{\sigma}$ is a stress tensor that reflects the influence of the adjacent fluid on a given fluid particle. The matrix representation of the stress tensor $\boldsymbol{\sigma}$ is

$$\boldsymbol{\sigma} = \begin{bmatrix} \tau_{11} & \tau_{12} & \tau_{13} \\ \tau_{21} & \tau_{22} & \tau_{23} \\ \tau_{31} & \tau_{32} & \tau_{33} \end{bmatrix} \tag{2.11}$$

where the main diagonal elements are normal stresses and the off-diagonal elements are shearing stresses. Furthermore, the balance of angular momentum in an inertial reference frame shows that the stress tensor is symmetric, $\tau_{ij} = \tau_{ji}$.

Since $\mathbf{u}$ and $D\mathbf{u}/Dt$ are continuous, the differentiation can be brought "inside" the integral, so that the momentum balance now becomes

$$\int_{\Omega} \rho \frac{D\mathbf{u}}{Dt}\, d\Omega = \int_{\Omega} \rho \mathbf{f} + \nabla \cdot \boldsymbol{\sigma}\, d\Omega \tag{2.12}$$

where we have made explicit use of the conservation of mass and the Gauss divergence theorem.

Because of the assumed continuity of the integrand and the arbitrary domain of integration, the above is equivalent to the *differential form* of the balance of momentum

$$\rho \frac{D\mathbf{u}}{Dt} = \rho \mathbf{f} + \nabla \cdot \boldsymbol{\sigma} \tag{2.13}$$

which is know as Cauchy's first law of motion. Cauchy's law of motion holds for every continuum, so it holds for every fluid, whatever its particular material properties are. Using the constitutive equation, that is, the relationship between the stress tensor and the motion, Cauchy's equation of motion changes to a specific equation of motion for the material under observation. The most simple constitutive relation for the stress tensor of a viscous fluid is a linear relationship between the stress tensor $\boldsymbol{\sigma}$ and the rate of deformation tensor $\mathbf{D}$

$$\boldsymbol{\sigma} = (-p + \lambda \nabla \cdot \mathbf{u})\, \mathbf{I} + 2\mu \mathbf{D} \tag{2.14}$$

where p is the pressure, λ and μ are macroscopic viscosity parameters, and

$$\mathbf{D} = \frac{1}{2}\left[(\nabla \mathbf{u}) + (\nabla \mathbf{u})^T\right] \tag{2.15}$$

By substituting (2.14) and (2.15) into (2.13), we obtain the *Navier-Stokes* equations

$$\rho \frac{D\mathbf{u}}{Dt} = \rho \mathbf{f} + \nabla \cdot (-p + \lambda \nabla \cdot \mathbf{u})\, \mathbf{I} + \nabla \cdot \mu \left[(\nabla \mathbf{u}) + (\nabla \mathbf{u})^T\right] \tag{2.16}$$

For isothermal fields or by ignoring the temperature dependence of λ and μ, we can

write (2.16) in a different form

$$\rho \frac{D\mathbf{u}}{Dt} = \rho \mathbf{f} - \nabla p + (\lambda + \mu)\, \nabla (\nabla \cdot \mathbf{u}) + \mu \nabla^2 \mathbf{u} \tag{2.17}$$

In incompressible flow, (2.7) applies and (2.17) reduces to

$$\rho \frac{D\mathbf{u}}{Dt} = \rho \mathbf{f} - \nabla p + \mu \nabla^2 \mathbf{u} \tag{2.18}$$

An alternate form to (2.18), which is considered fundamental by many, is

$$\rho \frac{D\mathbf{u}}{Dt} = \rho \mathbf{f} - \nabla p + \mu \nabla \cdot \left[(\nabla \mathbf{u}) + (\nabla \mathbf{u})^T \right] \tag{2.19}$$

The reason that (2.19) is often preferred to the simpler form, (2.18), is related to the the variational (weak) form and natural boundary conditions, which we derive later. Only (2.19) leads to natural boundary conditions that represent true physical forces. Even though (2.18) and (2.19) are equivalent in the continuum, the alternate representations lead to semi-discrete equations that are generally not equivalent.

2.2.3 Dimensionless form

It is useful, both physically and mathematically to recast the governing equations into dimensionless form. We do so by normalizing the coordinates $\mathbf{x}$ by a characteristic length L, the velocity field $\mathbf{u}$ by the characteristic velocity U, and the pressure by ρU^2. In this work we are concerned with advection dominated flows, so we assume that the time scale is set by advection – the appropriate measure of time is L/U. From equations (2.18) and (2.7), the dimensionless incompressible Navier-Stokes equations are

$$\frac{\partial \mathbf{u}}{\partial t} + (\mathbf{u} \cdot \nabla)\, \mathbf{u} + \nabla p - \frac{1}{\mathrm{Re}} \nabla^2 \mathbf{u} = \mathbf{f} \tag{2.20}$$

$$\nabla \cdot \mathbf{u} = 0 \tag{2.21}$$

where $\mathbf{f}$ has been suitably normalized and Re is the Reynolds number

$$\mathrm{Re} = \frac{U\,L\,\rho}{\mu} = \frac{U\,L}{\nu} \tag{2.22}$$

The Reynolds number may be interpreted as a ratio of the strength of inertial forces to viscous forces. Low Reynolds numbers mean strong momentum diffusion or highly viscous flow. High Reynolds numbers correspond to relatively strong driven, underdamped systems. Indeed, the singular limit $\mathrm{Re} \to \infty$ transforms the Navier-Stokes equations into the Euler's equations. Solutions of the Navier-Stokes equations at high Reynolds numbers may appear, locally, similar to inviscid flows. However, the boundary conditions for the Navier-Stokes equations are fundamentally different from those for Euler's equations, and viscous boundary layers are found near stationary walls. Further increases of the Reynolds number will ultimately lead to fully developed turbulence, in which the fluid behavior may no longer be deterministic but stochastic in nature. In the following we formally state the initial-boundary value problem of the incompressible Navier-Stokes equations and in Section 2.2.5 we quote some estimates addressing the issue of the dividing line between deterministic and stochastic behavior of the equations.

2.2.4 Formal problem statement

Let $\bar{\Omega}$ be the closure of an open bounded region Ω in R^n, where $n = 2$ or 3 represents the number of space dimensions, and $\mathbf{x} = (x_1, \ldots, x_n) = (x, y, z)$ be a point in $\bar{\Omega} = \Omega \cup \partial\Omega$, where $\partial\Omega = \Gamma$ is the boundary of Ω. We consider the solution of the Navier-Stokes equations governing incompressible flow, which in dimensionless form can be written as:

Find the velocity $\mathbf{u}(\mathbf{x},t)$ and pressure $p(\mathbf{x},t)$ such that

$$\frac{\partial \mathbf{u}}{\partial t} + (\mathbf{u}\cdot\nabla)\,\mathbf{u} + \nabla p - \frac{1}{\mathrm{Re}}\nabla\cdot\left[(\nabla\mathbf{u}) + (\nabla\mathbf{u})^T\right] = \mathbf{f} \qquad \text{in } \Omega\times(0,\tau] \tag{2.23}$$

$$\nabla\cdot\mathbf{u} = 0 \qquad \text{in } \Omega\times(0,\tau] \tag{2.24}$$

$$\mathbf{u}(\mathbf{x},0) = {}^0\mathbf{u}(\mathbf{x}) \qquad \text{in } \Omega \tag{2.25}$$

$$\mathbf{u} = \mathbf{u}^s \qquad \text{on } \Gamma_u \tag{2.26}$$

$$\mathbf{n}\cdot\boldsymbol{\sigma} = \mathbf{f}^s \qquad \text{on } \Gamma_f \tag{2.27}$$

where $\Gamma = \Gamma_u \cup \Gamma_f$ and $\Gamma_u \cap \Gamma_f = 0$, τ is a real number (time) > 0, Re is the Reynolds number, $\nabla\cdot{}^0\mathbf{u} = 0$, $\boldsymbol{\sigma} = -p\mathbf{I} + 1/\mathrm{Re}\left[(\nabla\mathbf{u}) + (\nabla\mathbf{u})^T\right]$, $\mathbf{f}$ is an externally applied force, $\mathbf{n}$ is the unit normal to the boundary of Ω, $\mathbf{u}^s$ is the prescribed velocity on the boundary Γ_u, $\mathbf{f}^s$ are the prescribed tractions on the boundary Γ_f, and in equation (2.25) the initial conditions are given. We assume the problem is well-posed.

In situations where outflow boundary conditions need to be modeled, the Navier-Stokes equations in the form of equation (2.20) are used. In such cases we drop the $(\nabla\mathbf{u})^T$ term in equation (2.23). The boundary conditions in equation (2.27) now become

$$\mathbf{n}\cdot\tilde{\boldsymbol{\sigma}} = \tilde{\mathbf{f}}^s \qquad \text{on } \Gamma_f \tag{2.28}$$

where $\tilde{\boldsymbol{\sigma}}$ is a pseudo-stress, $\tilde{\boldsymbol{\sigma}} = -p\mathbf{I} + (1/\mathrm{Re})\,\nabla\mathbf{u}$, and $\tilde{\mathbf{f}}^s$ are the prescribed pseudo-tractions on the boundary Γ_f.

2.2.5 Self-consistency

In deriving the Navier-Stokes equations we have adopted a macroscopic viewpoint. In doing so, we ignored all the fine details of the molecular or atomic structure and, for the purpose of study, replaced the discontinuous microscopic medium with a hypothetical continuum. For example the macroscopic, or continuum, velocity is defined as

$$\mathbf{u} = \frac{1}{n}\sum_{i=1}^{n}\mathbf{c}_i$$

where $\mathbf{c}_i$ are the velocities of the molecules and n is the number of molecules in the cluster. This cluster is the smallest part of the material that we consider and we call it a *fluid particle*. To justify this name, the volume which the cluster of molecules occupies must be small compared to the volume occupied by the whole part of the fluid under consideration. Furthermore, the number of molecules in the cluster must be large enough so that averaging makes sense, i.e., so that it becomes independent of the number of molecules. Considering that the number of molecules in on cubic centimeter of gas at standard temperature and pressure is 2.7×10^{19} [10], it is obvious that this condition is satisfied in many cases.

The density $\rho(\mathbf{x}, t)$ at the space point $\mathbf{x}$ is defined as the ratio of the sum of molecular masses in a cluster of molecules centered at $\mathbf{x}$ to the occupied volume $d\Omega$, with the understanding that the volume must be large enough for the density of the fluid particle to be independent of its volume. In other words, the mass of the fluid particle is a smooth function of its volume. If solutions of the deterministic Navier-Stokes equations turn out to vary on a length scale much smaller than the linear measure d of the volume $d\Omega$, then we are outside the validity domain of these equations. Here is the point where the self-consistency problem arises.

If $d\Omega$ is chosen too small, a single measurement of ρ may largely deviate from its mean value due to molecular fluctuations. If we require the relative fluctuation $\Delta\rho/\rho$ to be smaller than 10^{-3}, an estimate for a reasonable lower bound for d, the linear measure of $d\Omega$, should be $d \geq 3 \times 10^{-7}$ m for air, or $d \geq 1 \times 10^{-8}$ m for water [11].

Quoting Rauh [11], in the turbulent regime length scales decrease with increasing Reynolds number. The Kolomogorov length δ_K below which eddies are destroyed by dissipation, is given by $\delta_K = L/\mathrm{Re}^{3/4}$ where L is the external length scale. Another example would be the thickness δ_B of a turbulent boundary layer, which scales as $L/(\mathrm{Re}\log\mathrm{Re})$. If we take $L = 1$ cm, then δ_K and δ_B reach the continuum limit at Re $\mathcal{O}(10^6)$ for air and at Re $\mathcal{O}(10^7)$ for water. Based on this estimate, we can safely state that the deterministic Navier-Stokes equations are self-consistent up to Re $\mathcal{O}(10^6)$. Which in itself is a strong statement, since most engineering applications are defined at or below that order of magnitude.

2.3 Variational form

In the following we define some spaces that are needed for the formulation of the variational problem [9, 12]. $L_2(\Omega)$ is the space of square integrable functions defined over Ω,

$$L_2(\Omega) = \{a : \int_\Omega a^2 \, d\Omega < +\infty\}$$

The Sobolev space is defined for any non-negative integer k as the space of square integrable functions over Ω, whose derivatives up to order k are also square integrable over Ω

$$H^k(\Omega) = \{a \in L_2(\Omega) : \partial^n a \in L_2(\Omega), \forall |n| \leq k\}$$

Clearly $H^0(\Omega) = L_2(\Omega)$. For the vector valued function $\mathbf{a}$, we have the spaces

$$\mathbf{L}_2(\Omega) = \{\mathbf{a} : a_i \in L_2(\Omega)\}$$

$$\mathbf{H}^k(\Omega) = \{\mathbf{a} : a_i \in H^k(\Omega)\}$$

The variational form of the initial, boundary-value problem can be stated as follows:

Find $\mathbf{u} \in U$, $\mathbf{u}(\mathbf{x}, 0) = {}^0\mathbf{u}(\mathbf{x})$, $p \in Q$ such that for all $\mathbf{v} \in V$ and $q \in Q$; $t \in (0, \tau]$

$$\int_\Omega \left[\frac{\partial \mathbf{u}}{\partial t} + (\mathbf{u} \cdot \nabla)\mathbf{u}\right] \cdot \mathbf{v} \, d\Omega - \int_\Omega p \, (\nabla \cdot \mathbf{v}) \, d\Omega + \frac{1}{\mathrm{Re}} \int_\Omega \left[(\nabla \mathbf{u}) + (\nabla \mathbf{u})^T\right] \cdot \nabla \mathbf{v} \, d\Omega = \int_\Omega \mathbf{f} \cdot \mathbf{v} \, d\Omega + \int_{\Gamma_f} \mathbf{f}^s \cdot \mathbf{v} \, d\Gamma_f \tag{2.29}$$

$$\int_\Omega (\nabla \cdot \mathbf{u}) \, q \, d\Omega = 0 \tag{2.30}$$

where we use the linear spaces[1]

$$U = \left\{\mathbf{u} \in \mathbf{H}^1(\Omega), \mathbf{u}|_{\Gamma_u} = \mathbf{u}^s\right\}$$

[1] Actually, to be precise, U is not a linear space but an affine manifold (the same holds for the finite element space U_h defined later).

$$V = \left\{ \mathbf{v} \in \mathbf{H}^1(\Omega), \mathbf{v}|_{\Gamma_u} = \mathbf{0} \right\}$$

$$Q = \left\{ q \in H^0(\Omega) \right\}$$

We note that if the same functions are used in V as in U, the variational formulation corresponds to the standard Galerkin method (the Bubnov-Galerkin method). However we use a more general approach and therefore will in general not have that V and U coincide (when $\mathbf{u}^s = 0$).

2.4 Uniqueness and existence of weak solutions

The existence and uniqueness of weak solutions is addressed in the classic mathematical work by Temam [13] and Ladyzhenskaya [14]. Before going into further details, it may be well to pause and reflect upon the following quotation from Ladyzhenskaya [14] – for weak/generalized solutions: " Before becoming involved with precise formulations, we call the readers' attention to the fact that the statement 'it has been proved that the problem has a unique solution' can have very different meanings depending on the function space in which one looks for the solution. The form in which the requirements of the problem must be satisfied is different for different spaces, and different extensions of the concept of a solution of a problem, i.e., different 'generalized (weak) solutions', present themselves. In fact, for every problem there are infinitely many 'generalized (weak) solutions', but they coincide with the classical solution, if the latter exists." In other words, the weak solutions coincide with the strong (classical) solution if the latter exists.

For example, consider the solution of the linear advection-diffusion equation for a generic transported scalar $\theta(\mathbf{x})$, which in dimensionless form can be written as:

Find $\theta(\mathbf{x})$ such that

$$\mathbf{u} \cdot \nabla\theta - \frac{1}{\mathrm{Pe}} \Delta\theta = f \qquad \text{in } \Omega \tag{2.31}$$

$$\theta = \theta^s \qquad \text{on } \Gamma_\theta \tag{2.32}$$

$$\frac{1}{\mathrm{Pe}} \nabla\theta \cdot \mathbf{n} = f^s \qquad \text{on } \Gamma_f \tag{2.33}$$

where $\Gamma = \Gamma_\theta \cup \Gamma_f$ and $\Gamma_\theta \cap \Gamma_f = 0$, $\mathrm{Pe} = UL/\alpha$ is the Peclet number, $\mathbf{n}$ is the unit normal to the boundary of Ω, θ^s is the prescribed value of θ on the boundary Γ_θ, f^s is the prescribed flux on the boundary Γ_f. We assume the problem is well-posed. Both the velocity field $\mathbf{u}$ and the right-hand side f are prescribed. In the above the coordinates are normalized by a characteristic length L and the prescribed velocity field by the characteristic velocity U. The right-hand side f has been also suitably normalized and α in the definition of the Peclet number denotes the diffisivity of θ.

Let us first suppose that we have a solution, $\theta(\mathbf{x})$, that satisfies equations (2.31) through (2.33). Then clearly

$$\int_\Omega v \left(\mathbf{u} \cdot \nabla\theta - \frac{1}{\mathrm{Pe}} \Delta\theta - f \right) d\Omega = 0 \tag{2.34}$$

is satisfied for all functions $v(\mathbf{x})$. If we narrow down the class of test functions, so that $v \in H^1(\Omega)$ we can apply the Gauss divergence theorem to the second term in equation (2.34) to obtain

$$\int_\Omega v\,(\mathbf{u} \cdot \nabla\theta)\; d\Omega + \frac{1}{\mathrm{Pe}} \int_\Omega \nabla v \cdot \nabla\theta \, d\Omega = \int_\Omega v\, f \, d\Omega + \frac{1}{\mathrm{Pe}} \int_\Gamma v \, \nabla\theta \cdot \mathbf{n} \, d\Gamma \tag{2.35}$$

in which the normal boundary flux is now prominent. Recalling the Neumann bound-

ary condition given by equation (2.33), leads to

$$\int_{\Omega} v\,(\mathbf{u}\cdot\nabla\theta)\;d\Omega + \frac{1}{\mathrm{Pe}}\int_{\Omega}\nabla v\cdot\nabla\theta\,d\Omega = \int_{\Omega} v\,f\,d\Omega + \frac{1}{\mathrm{Pe}}\int_{\Gamma_\theta} v\,\nabla\theta\cdot\mathbf{n}\,d\Gamma_\theta + \int_{\Gamma_f} v\,f^s\,d\Gamma_f \tag{2.36}$$

where we have separated the boundary integral into two parts, one over Γ_θ and the other over Γ_f, in order to incorporate the Neumann boundary condition. We now further restrict the class of test functions to those that vanish on the Dirichlet portion of Γ; i.e., we now require $v = 0$ on Γ_θ. And so the weak or variational form of the advection-diffusion equation is – and this is *important* – obtained by dropping the assumption that $\theta(\mathbf{x})$ satisfies equations (2.31) through (2.33) and instead considering it as an unknown function that need only be once piecewise-differentiable. The variational form of the advection-diffusion boundary value problem in equations (2.31) through (2.33) can be stated as follows:

Find $\theta \in \Theta$ such that for all $v \in V$

$$\int_{\Omega} v\,(\mathbf{u}\cdot\nabla\theta)\;d\Omega + \frac{1}{\mathrm{Pe}}\int_{\Omega}\nabla v\cdot\nabla\theta\,d\Omega = \int_{\Omega} v\,f\,d\Omega + \int_{\Gamma_f} v\,f^s\,d\Gamma_f \tag{2.37}$$

where we use the spaces

$$\Theta = \left\{\theta \in H^1(\Omega), \theta|_{\Gamma_\theta} = \theta^s\right\}$$

$$V = \left\{v \in H^1(\Omega), v|_{\Gamma_\theta} = 0\right\}$$

We now discard equations (2.31) through (2.33) and regard the above statement as the given form of the problem; and also note that $\theta(\mathbf{x})$, the *weak* solution, can (but need not) now reside in a larger function space than do solutions of (2.31), since the weak solution need not even possess second spatial derivatives, at least in the classical sense.

Now we reverse the procedure that 'generated' the weak form – at least when this is permissible; i.e., when $\theta(\mathbf{x})$ is suffeciently smooth. To this end we assume sufficient regularity and manipulate the diffusion term as follows:

$$\begin{aligned}\int_\Omega \nabla v \cdot \nabla\theta \, d\Omega &= \int_\Omega \nabla \cdot (v\nabla\theta) \, d\Omega - \int_\Omega v\nabla \cdot \nabla\theta \, d\Omega \\ &= \int_\Gamma v \, \nabla\theta \cdot \mathbf{n} \, d\Gamma - \int_\Omega v\nabla \cdot \nabla\theta \, d\Omega \\ &= \int_{\Gamma_f} v \, \nabla\theta \cdot \mathbf{n} \, d\Gamma_f - \int_\Omega v \, \nabla^2\theta \, d\Omega\end{aligned}$$

so that equation (2.37) becomes after rearrangement,

$$\int_\Omega v \left(\mathbf{u} \cdot \nabla\theta - \frac{1}{\mathrm{Pe}} \nabla^2\theta - f \right) d\Omega = \int_{\Gamma_f} v \left(f^s - \frac{1}{\mathrm{Pe}} \nabla\theta \cdot \mathbf{n} \right) d\Gamma_f \tag{2.38}$$

for all $\theta \in \Theta$ and for all $v \in V$. Since this equation hold for all $v \in V$, it follows that it holds for that subset (say $\hat{V}$) that vanishes on Γ_f (as well as on Γ_θ); i.e., for the subset, we have

$$\int_\Omega v \left(\mathbf{u} \cdot \nabla\theta - \frac{1}{\mathrm{Pe}} \nabla^2\theta - f \right) d\Omega = 0$$

for all $v \in \hat{V}$.

But since even this subset contains an infinite number of functions (i.e., v is an arbitrary function in $\hat{V}$), it follows that

$$\mathbf{u} \cdot \nabla\theta - \frac{1}{\mathrm{Pe}} \nabla^2\theta - f = 0 \qquad \text{in } \Omega$$

and we see that $\theta(\mathbf{x})$ satisfies the original partial differential equation. And this fact, with equation (2.38), leads directly to

$$\int_{\Gamma_f} v \left(f^s - \frac{1}{\mathrm{Pe}} \nabla\theta \cdot \mathbf{n} \right) d\Gamma_f = 0$$

for all $v \in V$. But again the set of test functions is of infinite dimension, and thus

$$\frac{1}{\mathrm{Pe}} \nabla\theta \cdot \mathbf{n} = f^s \qquad \text{on } \Gamma_f$$

is necessarily true. Hence, we have just proven a special case of the following general result: *if the solution of a weak form of the problem is sufficiently smooth, then that solution is also a classical solution of the same problem.* The key word is IF, a word that is missing when going the other direction – i.e., a classical solution is always also a weak solution.

Weak solutions are also referred to as generalized solutions or solutions in a distributional sense. If the classical solution exists, – which requires (at least) smooth data (e.g. no delta functions in f) and a domain with a sufficiently smooth boundary (e.g. no L-shaped domains are allowed), then the weak solution will also be a classical solution, as shown above. If, however, the problem is not smooth enough, a strictly classical solution will not exist, whereas a weak solution usually will.

We conclude by reiterating: classical solutions are subsets of weak solutions; classical solution will always satisfy equation (2.37), but solutions of (2.37) will not always satisfy (2.31). ■

Going now back to the Navier-Stokes equations, the basic results on uniqueness and existence of weak solutions can be summarized in the following theorem:

Theorem: A unique weak solution exists, at least in the time interval $t \in [0, \tau_1]$ with $\tau \leq \tau_1$, provided the external force $\mathbf{f}$ obeys the condition

$$\int_0^\tau \int_\Omega \left[\mathbf{f}^2 + \left(\frac{\partial \mathbf{f}}{\partial t} \right)^2 \right]^{1/2} < \infty \tag{2.39}$$

However, even if the condition on the external force field $\mathbf{f}$ holds for arbitrary large τ, uniqueness can only be guaranteed by the above theorem for the smaller time interval $t \in [0, \tau_1]$. While this is typical in space dimension three, one has $\tau_1 = \tau$ in the case of two-dimensional flows.

So far we have quoted from Rauh [11] that the Navier-Stokes equations are self-consistent up to about Reynolds number 10^6 and based on the mathematical work of Temam and Ladyzhenskaya we know that weak solutions of well-posed transient problems exist, and in the case of two-dimensional flow these are guaranteed to be unique. Hence, it is reasonable to endeavor to obtain a finite element procedure which will solve high Reynolds number flows.

Chapter 3

Discretization schemes

3.1 Introduction

The main objective of this work is to develop schemes to suppress the numerical instability associated with the convection term in the finite element solution of the incompressible Navier-Stokes equations. As mentioned in Chapter 1, this numerical instability is due to the symmetric treatment of the convection term, which results in spurious oscillations if the discretization scale is too large to resolve subgrid scales. Such oscillations become significant as the Reynolds number increases.

We start the chapter by studying local analytic procedures, which are the cornerstone in our development of finite element discretization schemes for high Reynolds number flow. The first of the four discretization schemes is not a Galerkin approach in its entirety, in that the Navier-Stokes equations are not discretized using their variational form but a local analytic procedure directly. The other three discretization schemes are based on the Petrov-Galerkin formulation for the Navier-Stokes equations, where the test functions respond to the flow conditions surrounding the element so as to give more weight to upstream nodes. These formulations differ from each other in the way the test functions are established. We conclude the chapter by performing the inf-sup test for advection dominated flows.

3.2 Local analytic procedures

By local analytic procedures we understand the embedding of local analytic behavior into the numerical solution of the governing equation(s). To study local behavior we must first construct a finite element model of $\bar{\Omega}$.

A finite element model of the closed domain $\bar{\Omega}$ is a region $\bar{\Omega}^h$ which is the union of a finite number E of bounded subregions $\bar{\Omega}_e$, each $\bar{\Omega}_e$ being the closure of an open region Ω_e:

$$\bar{\Omega}_e = \Omega_e \cup \partial\Omega_e \qquad e = 1, 2, \ldots, E$$

where $\partial\Omega_e$ is the boundary of Ω_e. The bounded subregions $\bar{\Omega}_e$ are called finite elements of $\bar{\Omega}^h$, and we select $\bar{\Omega}^h$ to coincide with, or at least closely approximate, $\bar{\Omega}$. The region $\bar{\Omega}^h$ is called the connected model or discretization of $\bar{\Omega}$, and the open elements Ω_e are pairwise disjoint. We have

$$\bar{\Omega}^h = \bigcup_{e=1}^{E} \bar{\Omega}_e$$

$$\Omega_e \cap \Omega_f = \varnothing \qquad e \neq f$$

In the connected model, we identify a finite number G of points, called *global nodes*, and we label them consecutively $\mathbf{x}^1, \mathbf{x}^2, \ldots, \mathbf{x}^G$. Likewise we identify within each element $\bar{\Omega}_e$ a number of N_e points, called *local nodes*, and we label them consecutively $\mathbf{x}_e^1, \mathbf{x}_e^2, \ldots, \mathbf{x}_e^{N_e}$; $e = 1, 2, \ldots, E$. A correspondence must exist between points in $\bar{\Omega}_e$ and $\bar{\Omega}^h$, in particular, between nodal points $\mathbf{x}_e^n$ in $\bar{\Omega}_e$ and nodes $\mathbf{x}^i$ in $\bar{\Omega}^h$, if the elements are to fit together smoothly to form $\bar{\Omega}^h$.

We take the linear advection-diffusion equation, which is prototypical of the Navier-Stokes equations, as our model equation and obtain a local analytic solution for the case of two-dimensional flow.

3.2.1 Advection-Diffusion as a model equation

Consider the case of two-dimensional flow. Let $\mathcal{P}_h = \{\mathcal{Q}\}$ be a family of quadrilateral finite elements $\bar{\Omega}_e$ that make up the connected model $\bar{\Omega}^h$. For simplicity, lets take the special case where $\mathcal{P}_h$ consists of rectangles. Consider one such rectangle $\bar{\Omega}_e = \mathcal{Q}$ and let $\mathbf{x} = (x_1, x_2) = (x, y)$ be a point in $\bar{\Omega}_e$. Furthermore, let us give the rectangle dimensions $-h \leq x \leq h$ and $-k \leq y \leq k$, as shown in Figure 3-1.

Consider the linear advection-diffusion equation in dimensionless form:

$$\mathbf{u} \cdot \nabla\theta - \frac{1}{\mathrm{Pe}} \nabla^2\theta = f \qquad \text{in } \Omega_e \tag{3.1}$$

where $\theta(\mathbf{x})$ is the transported scalar, Pe is the Peclet number, and both the velocity field $\mathbf{u} = (u_1, u_2)$ and the right-hand side f are prescribed and piecewise constant with respect to the discretization $\mathcal{P}_h$. In the above the coordinates are normalized by a characteristic length L and the prescribed velocity field by the characteristic velocity U. The right-hand side f has been also suitably normalized.

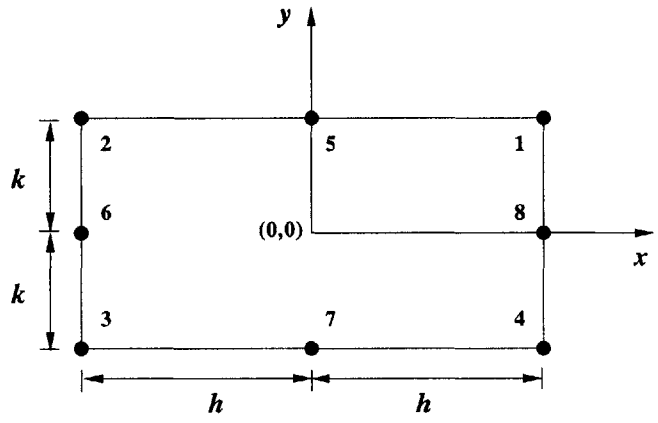

Figure 3-1: Rectangular element with 8 boundary nodes.

We specify a combination of exponential and linear boundary functions on all four

boundaries of the rectangle, for example, at $y = k$ and $x = h$, the boundary functions are of the form

$$\theta(x) = a_N \left(e^{2Ax} - 1\right) + b_N x + c_N \tag{3.2}$$

$$\theta(y) = a_E \left(e^{2By} - 1\right) + b_E y + c_E \tag{3.3}$$

with

$$2A = (\mathrm{Pe})\, u_1 \qquad \text{and} \qquad 2B = (\mathrm{Pe})\, u_2 \tag{3.4}$$

The boundary functions suggest that a total of eight nodes, $N_e = 8$, should be placed on the boundary of the rectangle $\mathcal{Q}$, as shown in Figure 3-1.

With the specification of the boundary functions, equation (3.1) can be solved analytically by the method of separation of variables to obtain coefficients $\{\alpha_n(\mathbf{x})\}_{n=1}^{8}$, $\alpha_f(\mathbf{x})$ such that

$$\theta(\mathbf{x}) = \sum_{n=1}^{8} \alpha_n(\mathbf{x})\ \theta_n + \alpha_f(\mathbf{x})\ f \tag{3.5}$$

When evaluated at $\mathbf{x} = (0,0)$, the coefficients $\{\alpha_n(\mathbf{0})\}_{n=1}^{8} = \{\alpha_n^0\}_{n=1}^{8}$, $\alpha_f(\mathbf{0}) = \alpha_f^0$ are:

$$\begin{aligned}
\alpha_1^0 &= e^{-Ah-Bk} D_0 & \alpha_5^0 &= e^{-Bk} D_1 \\
\alpha_2^0 &= e^{Ah-Bk} D_0 & \alpha_6^0 &= e^{Ah} D_2 \\
\alpha_3^0 &= e^{Ah+Bk} D_0 & \alpha_7^0 &= e^{Bk} D_1 \\
\alpha_4^0 &= e^{-Ah+Bk} D_0 & \alpha_8^0 &= e^{-Ah} D_2
\end{aligned} \tag{3.6}$$

$$\begin{aligned}
\alpha_f^0 = &\frac{1}{2\left(A^2 + B^2\right)} \Big\{ Ah \tanh Ah + Bk \tanh Bk - \\
&4 \cosh Ah \cosh Bk \left[(Ah)^2 E_2 + (Bk)^2 E_2' \right] \Big\}
\end{aligned} \tag{3.7}$$

with

$$D_0 = \frac{1}{2}\left(E_1 + E_1^{'}\right) - Ah\coth AhE_2 - Bk\coth BkE_2^{'} \tag{3.8}$$

$$D_1 = 2Ah\coth Ah\cosh AhE_2 \tag{3.9}$$

$$D_2 = 2Bk\coth Bk\cosh BkE_2^{'} \tag{3.10}$$

where E_1, E_2, $E_1^{'}$, and $E_2^{'}$ are infinite series:

$$E_i = \sum_{m=1}^{\infty} \frac{-(-1)^m\left(\lambda_m^h h\right)}{\left[(Ah)^2 + (\lambda_m^h h)^2\right]^i}\left(\frac{1}{\cosh\left(\mu_m^h k\right)}\right) \tag{3.11}$$

with

$$\lambda_m^h = \frac{(2m-1)\pi}{2h}, \qquad \mu_m^h = \sqrt{A^2 + B^2 + \left(\lambda_m^h\right)^2}$$

and similarly

$$E_i^{'} = \sum_{m=1}^{\infty} \frac{-(-1)^m\left(\lambda_m^k k\right)}{\left[(Bk)^2 + (\lambda_m^k k)^2\right]^i}\left(\frac{1}{\cosh\left(\mu_m^k h\right)}\right) \tag{3.12}$$

with

$$\lambda_m^k = \frac{(2m-1)\pi}{2k}, \qquad \mu_m^k = \sqrt{A^2 + B^2 + \left(\lambda_m^k\right)^2}$$

By explicitly enforcing zeroth and first order consistency on $\{\alpha_n^0\}_{n=1}^8$, we are able to express functions of the infinite series analytically:

$$\frac{1}{2}\left(E_1 + E_1^{'}\right) = \frac{1}{4\cosh Ah\cosh Bk} \tag{3.13}$$

$$E_2^{'} - E_2\left(\frac{h}{k}\right)^2 = \frac{Ak\tanh Bk - Bh\tanh Ah}{4AkBk\cosh Ah\cosh Bk} \tag{3.14}$$

Often, the *order of consistency* is also called the *order of the polynomial which is represented exactly.* Consistency conditions are closely related to reproducing conditions. Reproducing conditions refer to the ability of an approximation to reproduce a function if the nodal values are set by the function; thus the ability to reproduce nth order polynomials is equivalent to nth order consistency.

Note that now we are left to evaluate only one series summation, E_2 or E_2'. Our numerical experiments indicate that taking the first twelve terms in either series is sufficient. Details of the solution procedures are given in Appendix A.

In practical implementations $\mathcal{P}_h$ will seldom consist of rectangles. In some areas or throughout the entire connected model the quadrilaterals may be geometrically distorted. We proceed by mapping $\bar{\Omega}_e$ to a bi-unit square $\hat{\Omega}_e = [-1,1] \times [-1,1]$, where $\boldsymbol{\xi} = (\xi_1, \xi_2) = (\xi, \eta)$ is a point in $\hat{\Omega}_e$. In this new coordinate system equations (3.6) and (3.7) still apply, with the following new definitions:

$$A = \frac{c_1}{\sqrt{g^{11}}} \qquad \text{and} \qquad B = \frac{c_2}{\sqrt{g^{22}}} \tag{3.15}$$

with

$$2c_i = \mathrm{Pe}\frac{\partial \xi_i}{\partial x_j} a_j - \frac{1}{J}\frac{\partial}{\partial \xi_k}\left(J g^{ik}\right) \tag{3.16}$$

where g^{ij} is the contravariant metric tensor and J is the Jacobian associated with the mapping. Also, h and k are to be replaced by $1/\sqrt{g^{11}}$ and $1/\sqrt{g^{22}}$ when used in equations (3.6) and (3.7). Recall that, from equation (3.4), A and B are to be piecewise constant with respect to the discretization $\mathcal{P}_h$ and hence in equation (3.15) representative values of the parameters over the element must be chosen. Details of the transformation are given in Appendix B.

The local analytic coefficients $\{\alpha_n^0\}_{n=1}^8$, α_f^0 are functions of the geometry of the subregion Ω_e, the velocity field $\mathbf{u}$, and the Peclet number. Furthermore, the coefficients are always positive. Hence, using the fact that the coefficients $\{\alpha_n^0\}_{n=1}^8$ have zeroth order consistency we can bound them: $0 \leq \{\alpha_n^0\}_{n=1}^8 \leq 1$.

3.2.2 The finite analytic method

The local analytic solution to the advection-diffusion equation has been previously studied and successfully used to develop discretization schemes to solve the two-dimensional incompressible Navier-Stokes equations. Indeed, the advection-diffusion

equation and the momentum equations are similar in form,

$$\frac{\partial \theta}{\partial t} + \mathbf{u} \cdot \nabla \theta - \frac{1}{\mathrm{Pe}} \nabla^2 \theta = f \tag{3.17}$$

$$\frac{\partial \mathbf{u}}{\partial t} + (\mathbf{u} \cdot \nabla)\, \mathbf{u} - \frac{1}{\mathrm{Re}} \nabla^2 \mathbf{u} = \mathbf{f} - \nabla p \tag{3.18}$$

and equation (3.5) can be used to develop discretization schemes.

In the finite analytic (FA) method of Chen and Chen [15, 16] a node is placed at $\mathbf{x} = (0, 0)$ in element $\mathcal{Q}$ of Figure 3-1. Equation (3.5) is evaluated at the interior node and the resulting coefficients, given by equations (3.6) and (3.7), are used to construct a stencil relating nine nodal variables. Note that equations (3.6) and (3.7) are now used with

$$2A = (\mathrm{Re})\, u_1^0 \qquad \text{and} \qquad 2B = (\mathrm{Re})\, u_2^0 \tag{3.19}$$

where u_1^0 and u_2^0 are now the unknown dimensionless velocity components at $\mathbf{x} = (0, 0)$ in element $\mathcal{Q}$.

Using the backward Euler method to approximate the transient term and lumping it as part of the right-side, results in the FA discretization formula for the two-dimensional momentum equations (3.18):

$$\begin{aligned} {}^{t+\Delta t}\mathbf{u}^0 = & \frac{1}{1 + \mathrm{Re}\ \alpha_f^0/\Delta t} \left\{ \sum_{n=1}^{8} \alpha_n^0\ {}^{t+\Delta t}\mathbf{u}_n + \mathrm{Re}\ \frac{\alpha_f^0}{\Delta t}\ {}^{t}\mathbf{u}^0 \right. \\ & \left. - \alpha_f^0 \left[{}^{t+\Delta t}(\nabla p)^0 - {}^{t+\Delta t}\mathbf{f}^0 \right] \right\} \end{aligned} \tag{3.20}$$

Notice that equation (3.20) is nonlinear, in that the coefficients depend on the velocity field at time $t + \Delta t$. Hence, a fixed point iteration scheme is needed in order to solve (3.20) at each time step. Chen et al. [16] extended the FA method to solve the incompressible Reynolds-Averaged Navier-Stokes equations in three dimensions, which has been used to solve flows with Reynolds numbers of $\mathcal{O}(10^4)$ in the area of turbomachinery [17] and $\mathcal{O}(10^7)$ in the area of submarine technology [18]. However,

the FA method only proves effective when $\mathcal{P}_h$ satisfies some regularity constrains: the mesh must have a high degree of orthogonality.

Even though severe element geometric distortions are not allowed, one might still encounter orthogonal curvilinear elements in the connected model. In such situations the mapping procedures described in Section 3.2.1 apply and equations (3.6) and (3.7) are used with

$$A = \frac{c_1^0}{\sqrt{g^{11}|_0}} \qquad \text{and} \qquad B = \frac{c_2^0}{\sqrt{g^{22}|_0}} \tag{3.21}$$

where

$$2c_i = \mathrm{Re}\frac{\partial \xi_i}{\partial x_j} u_j - \frac{1}{J}\frac{\partial}{\partial \xi_k}\left(J g^{ik}\right) \tag{3.22}$$

Also, h and k are to be replaced by $1/\sqrt{g^{11}|_0}$ and $1/\sqrt{g^{22}|_0}$ when used in equations (3.6) and (3.7).

3.3 Finite element formulations

In the following we describe in detail four finite element discretization schemes for the solutions of two-dimensional high Reynolds number incompressible fluid flows. These schemes are based directly or partially on the local analytic procedures described in the previous section.

3.3.1 Finite Analytic/Finite Element (FAFE) scheme

In this approach we use the finite analytic discretization, developed in the previous section, for the Navier-Stokes equations and enforce the incompressibility constraint in a weighted residual fashion.

3.3.1.1 Discretization procedures

We define the connected model $\bar{\Omega}^h \in R^2$ as the union of non-overlapping quadrilaterals $\mathcal{Q} \in \mathcal{P}_h$. Let $\mathbf{x} = (x_1, x_2) = (x, y)$ be a point in $\bar{\Omega}^h$.

We first identify G_u global nodes for the velocity degrees of freedom. Here we simply take $G_u = G$. Next, we identify a finite number G_{int} of nodes that do not

lie on $\partial\Omega^h$, called *interior nodes*, which form a subset of the G global nodes in the connected model. We associate with each interior node its eight closest neighbors, and for each interior node we write equation (3.20) for the two velocity components: u_1 and u_2.

The incompressibility constraint is enforced in a weighted residual fashion. For this purpose we make use of the 9/4-c element and identify G_p global nodes for the pressure degree of freedom. In the continuity equation we use C^0 biquadratic functions $\{h_m(\mathbf{x})\}_{m=1}^{G_u}$ as trial functions for the velocity degrees of freedom and C^0 bilinear functions $\{\varphi_n(\mathbf{x})\}_{n=1}^{G_p}$ as test functions, all of them with compact support. The pressure gradient in the momentum equations is approximated by finite differences using the G_p nodes.

Note that the construction of the discretized momentum equations takes place at the global node level, while the construction of the discretized continuity equation can be done using standard finite element procedures at the element level. The assembled system of equations are

$$\begin{pmatrix} \mathbf{N} & \mathbf{0} & \mathbf{C}^{u_1} \\ \mathbf{0} & \mathbf{N} & \mathbf{C}^{u_2} \\ \mathbf{D}^{u_1} & \mathbf{D}^{u_2} & \mathbf{0} \end{pmatrix} \begin{pmatrix} \mathbf{u}_1 \\ \mathbf{u}_2 \\ \mathbf{p} \end{pmatrix} = \begin{pmatrix} \mathbf{f}^{u_1} + \mathbf{b}^{u_1} \\ \mathbf{f}^{u_2} + \mathbf{b}^{u_2} \\ \mathbf{b}^D \end{pmatrix} \tag{3.23}$$

where $\mathbf{u}_1$ is a vector of length G_u of nodal velocities in the x_1 direction, $\mathbf{u}_2$ is a vector of length G_u of nodal velocities in the x_2 direction, $\mathbf{p}$ is a vector of length G_p of nodal pressures. The diagonal $\mathbf{N}$ sub-matrices contain the combined effect of advection and diffusion, and, in the case of transient problems, the effect of the temporal terms – all these effects represented by the local analytic coefficients $\{\alpha_n^0\}_{n=1}^8$, α_f^0 at each global node. The $\mathbf{C}$ sub-matrices contain the pressure gradient contributions, represented here by a finite difference approximation. The $\mathbf{D}$ sub-matrices appearing in the continuity equation are the velocity divergence operators:

$$D_{ij}^{u_1} = \int_{\Omega^h} \varphi_i \frac{\partial h_j}{\partial x_1}, \qquad D_{ij}^{u_2} = \int_{\Omega^h} \varphi_i \frac{\partial h_j}{\partial x_2}$$

The vectors $\mathbf{b}^{u_1}$, $\mathbf{b}^{u_2}$, and $\mathbf{b}^D$ account for the non-zero essential boundary conditions on the velocity degrees of freedom. Finally the vectors $\mathbf{f}^{u_1}$, $\mathbf{f}^{u_2}$ contain surface-flux type contributions from the natural boundary conditions, effects from externally applied body forces, and in the case of transient flows, history effects from previous time levels.

The system of equations is nonlinear, in that at every node the coefficients $\{\alpha_n^0\}_{n=1}^8$, α_f^0 are functions of the unknown velocity components. Hence, a fixed point iteration solution scheme is adopted.

3.3.2 Local Analytic/Petrov-Galerkin (LAPG) scheme

3.3.2.1 Test functions

In this approach, we endow the test functions with properties from the local analytic solution of the advection-diffusion equation:

$$\phi_m(\mathbf{x}) = \sum_{n=1}^{8} L_{mn}\alpha_n(\mathbf{x}) \tag{3.24}$$

where $\{L_{mn}(\mathbf{x})\}$ is a boundary interpolant which needs proper motivation and definition, $\{\alpha_n(\mathbf{x})\}$ are the local analytic coefficients, and $\{\phi_m(\mathbf{x})\}$ are the enhanced test functions. Of course, the definitions for the local analytic coefficients, $\{\alpha_n(\mathbf{x})\}$, in Section 3.2.1 are still applicable but with the Peclet number replaced by the Reynolds number and the prescribed velocity field $\mathbf{u}$ replaced by the unknown velocity field, as was done in developing the finite analytic discretization scheme in Section 3.2.2.

Evaluation of the enhanced test functions $\{\phi_m(\mathbf{x})\}$ requires the evaluation of the local analytic coefficients $\{\alpha_n(\mathbf{x})\}$ at other points besides $\mathbf{x} = (0,0)$. The coefficients at any other point require the evaluation of additional series and these evaluations could become computationally inefficient and/or numerically ill conditioned.

To reduce computational costs and/or avoid the evaluation of numerical ill conditioned series we introduce the following approximation scheme: we translate the local coordinate axes to the evaluation point and use the coefficients $\{\alpha_n^0\}_{n=1}^8$ together with

an interpolation scheme using the boundary functions. For example, for $0 < x < h$, $0 < y < k$, with $h_E = h - x, h_W = 2h - x$ and $h_N = k - y, h_S = 2k - y$ the coefficients are

$$
\begin{aligned}
G\,\alpha_1 &= \alpha_1^0 + (s-1)\,\alpha_2^0 + (t-1)\,\alpha_4^0 + (s-1)\,(t-1)\,\alpha_3^0 \\
G\,\alpha_2 &= \bar{s}\,\alpha_2^0 + \bar{s}\,(t-1)\,\alpha_3^0 \\
G\,\alpha_3 &= \bar{s}\,\bar{t}\,\alpha_3^0 \\
G\,\alpha_4 &= \bar{t}\,\alpha_4^0 + \bar{t}\,(s-1)\,\alpha_3^0 \\
G\,\alpha_5 &= \alpha_5^0 + (t-1)\,\alpha_7^0 + (2-s-\bar{s})\,\alpha_2^0 + (t-1)\,(2-s-\bar{s})\,\alpha_3^0 \\
G\,\alpha_6 &= \bar{s}\,\alpha_6^0 + \bar{s}\,(2-t-\bar{t})\,\alpha_3^0 \\
G\,\alpha_7 &= \bar{t}\,\alpha_7^0 + \bar{t}\,(2-s-\bar{s})\,\alpha_3^0 \\
G\,\alpha_8 &= \alpha_8^0 + (s-1)\,\alpha_6^0 + (2-t-\bar{t})\,\alpha_4^0 + (s-1)\,(2-t-\bar{t})\,\alpha_3^0 \\
G\,\alpha_f &= \alpha_f^0 \\
G &= 1 - (2-s-\bar{s})\,\alpha_6^0 - (2-t-\bar{t})\,\alpha_7^0 - (2-s-\bar{s})\,(2-t-\bar{t})\,\alpha_3^0
\end{aligned}
$$

where $\{\alpha_n^0\}_{n=1}^8$, α_f^0 are given in (3.6) and (3.7), and used with $h = h_E$, $k = h_N$. In the above

$$
s = \frac{h_W\left(e^{2Ah_E} + e^{-2Ah_E} - 2\right)}{h_W\left(e^{2Ah_E} - 1\right) + h_E\left(e^{-2Ah_W} - 1\right)}, \qquad \bar{s} = s\frac{h_E}{h_W} \tag{3.25}
$$

$$
t = \frac{h_S\left(e^{2Ah_N} + e^{-2Ah_N} - 2\right)}{h_S\left(e^{2Ah_N} - 1\right) + h_N\left(e^{-2Ah_S} - 1\right)}, \qquad \bar{t} = t\frac{h_N}{h_S} \tag{3.26}
$$

Details of the interpolation procedures are given in Appendix A. By construction, the coefficients $\{\alpha_n(\mathbf{x})\}_{n=1}^8$ retain zeroth and first order consistency. For geometrically distorted elements the procedures and definitions described in Section 3.2.1 apply.

Plots of $\alpha_6(\mathbf{x})$ in a bi-unit square for different values of Ah and Bk are shown in Figure 3-2. Figure 3-2a shows the case of pure diffusion. In Figure 3-2b convection is present, flow is in the positive x direction. Note how the function responds to the flow conditions, the solution at any point inside the bi-unit square will have a

strong dependence from the upstream value θ_6. Figure 3-2c shows the case of flow in the positive y direction, in this scenario θ_6 will have little or no contribution to the solution. Figure 3-2d shows the function's response to flow at an angle. We can see that the function responds appropriately to the skewed velocity vector.

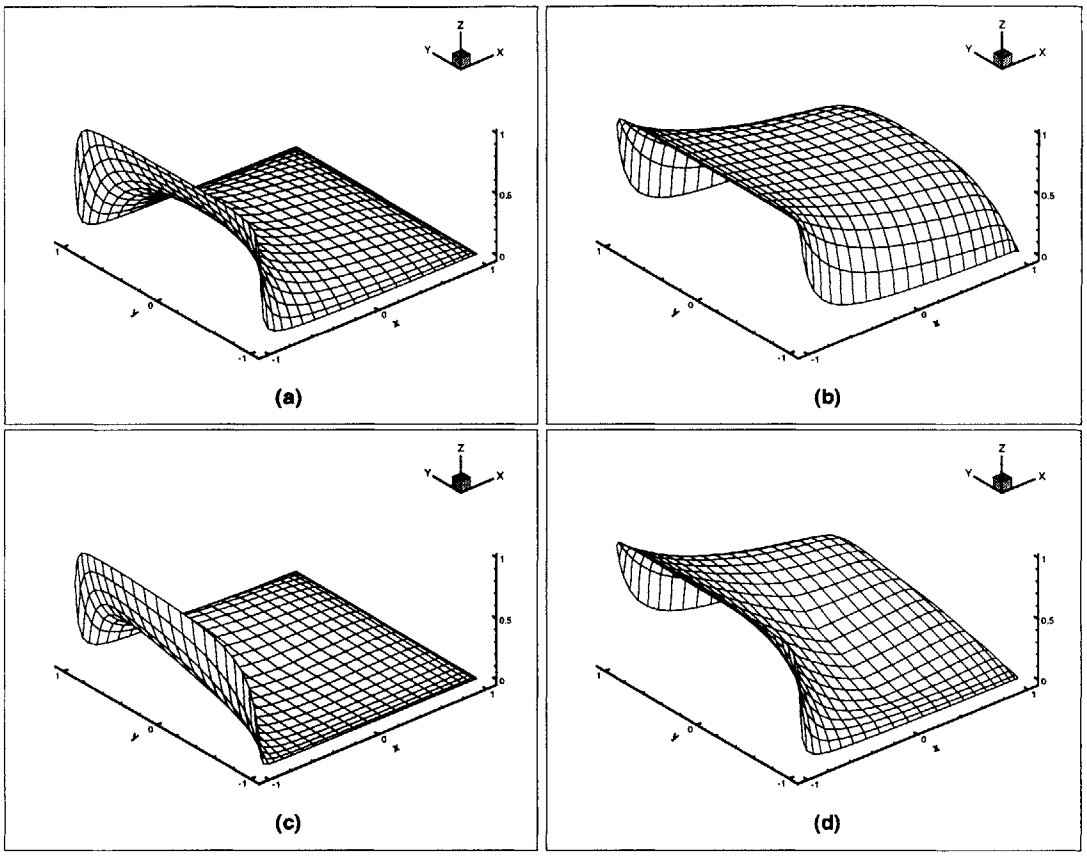

Figure 3-2: $\alpha_6(\mathbf{x})$ for different values of Ah and Bk. The case of $Ah = Bk = 0$ is that of pure diffusion (a). In (b) convection is present, flow is strictly in the positive x direction, $Ah = 5$, $Bk = 0$. In (c) flow is strictly in the positive y direction, $Ah = 0$, $Bk = 5$. In (d) convection is present in the positive x and y directions, flow at a 30° angle from the x axis, $Ah = 2\sqrt{3}$, $Bk = 2$.

The coefficients, $\{\alpha_n(\mathbf{x})\}_{n=1}^{8}$, possess the ability to respond to the local flow conditions including any skewed advective vector. Furthermore, they provide a smooth transition from diffusion dominated to advection dominated conditions. Indeed, the coefficients $\{\alpha_n(\mathbf{x})\}_{n=1}^{8}$ could be used directly as test functions. However, we note from Figure 3-2, that the functions fail to recover the imposed boundary functions,

i.e., they are unable to reproduce the Kronecker delta property. This is due to the approximation made to evaluate the functions at any other points besides $\mathbf{x} = (0, 0)$. It is true that the test functions need not satisfy the Kronecker delta property, however, this property will ensure that the test functions vanish on Γ_u.

To correct for this we make use of equation (3.24) with the following definition for the boundary interpolant $\{L_{mn}(\mathbf{x})\}$:

$$L_{mn}(\mathbf{x}) = h_m(\mathbf{x}_e^{n'}), \qquad \mathbf{x}_e^{n'} = \begin{cases} \mathbf{x}_e^n & \text{if } n = 1, 2, 3, \text{ or } 4, \\ \mathbf{x} \to \partial\Omega_e,\ \mathbf{x}_e^n & \text{if } n = 4, 5, 6, \text{ or } 8. \end{cases} \tag{3.27}$$

where $h_m(x)$ is a Lagrange boundary function, i.e. it is only defined along the boundary of the element, and $[\mathbf{x} \to \partial\Omega_e,\ \mathbf{x}_e^n]$ denotes the projection of $\mathbf{x}$ onto the portion of the boundary $\partial\Omega_e$ that contains local node $\mathbf{x}_e^n$. The locations of the evaluation points $\mathbf{x}_e^{n'}$ in equation (3.27) are shown schematically in Figure 3-3 for an arbitrary point $\mathbf{x} = (x, y)$.

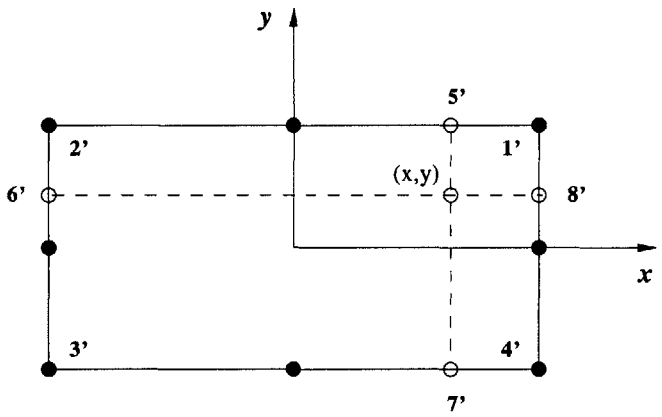

Figure 3-3: Rectangular element showing the evaluation points $\mathbf{x}_e^{n'}$.

In this manner, given a boundary function along the edges of the element, we bring local analytic behavior inside the element. This approach has some similarities

with Brezzi's Residual-Free Bubbles (RFB) procedures [6, 19], specifically the *divide and conquer* principle [20]. Here we use the information at the edges of the elements and enrich (not augment) the finite element space of test functions with local analytic properties.

The enhanced test functions $\{\phi_m(\mathbf{x})\}$ now satisfy the Kronecker delta condition. This can be easily proven in the following manner:

$$\phi_m(\mathbf{x}_e^n) = \sum_n L_{mn}(\mathbf{x}_e^n)\,\alpha_n(\mathbf{x}_e^n) = \sum_n \delta_{mn}\,\alpha_n(\mathbf{x}_e^n) = \delta_{mn}$$

since

$$\sum_n \alpha_n(\mathbf{x}) = 1$$

and

$$L_{mn}(\mathbf{x}_e^n) = h_m(\mathbf{x}_e^n) = \delta_{mn}$$

At this point, the element Lagrange boundary or edge functions $h_m(x)$ can be any functions such that $N_e = 8$, i.e. such that three nodes are used to define the functions on each edge. Regardless of the edge functions we choose, the effect of the local analytic solution is already carried by the coefficients $\{\alpha_n(\mathbf{x})\}$. In this work we use linear-exponential edge functions of the form (3.2), (3.3) and add an x^2, y^2 bubble function to obtain the 9-node element test functions. More on the linear-exponential edge functions will be said in Section 3.3.4. Note, however, that the x^2, y^2 bubble function will contain no effects from the local analytic coefficients $\{\alpha_n(\mathbf{x})\}$, i.e., it will not respond to the flow conditions over the element.

Consider the two 9 node element patch (see Figure 3-4a). In the case of pure diffusion the test function for node A is symmetric (Figure 3-4b). Figure 3-4c shows the test function when convection is present, for the case of flow in the positive x direction. Figure 3-4d shows the function for the case of flow at an angle, both x and y components of velocity are present. The enhanced test functions, $\{\phi_m(\mathbf{x})\}$, place emphasis on the upstream directions – consistent with the physics of the problem.

We remark that the enhanced test functions inherit the ability to respond to any

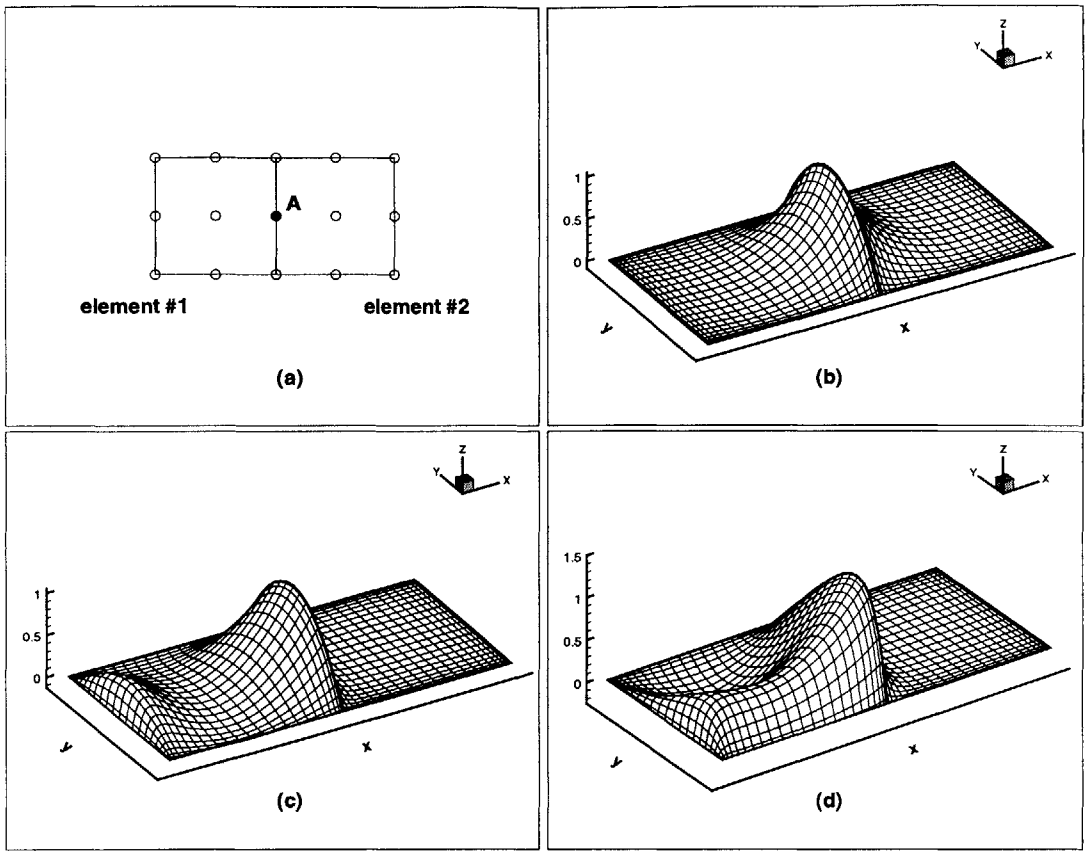

Figure 3-4: Two 9 node element patch (a). In the case of pure diffusion the test function is symmetric (b). In (c) convection is present, flow is strictly in the positive x direction. In (d) convection is present in the positive x and y directions, flow at a 30° angle from the x axis.

skewed velocity vector. Furthermore, the amount of weighting given to upstream nodes is controlled analytically, so that a smooth transition from diffusion dominated to convection dominated conditions is achieved.

3.3.2.2 Differentiation of the test functions

The finite element formulation requires that we differentiate the test functions $\{\phi_m(\mathbf{x})\}$. Accurate differentiation in any finite element procedure is very important. This is sometimes taken for granted in classical implementations of the finite element method where the test functions are polynomials and can be easily differentiated. In this formulation a closed form expression for the test functions is not available because of the approximations associated in deriving them. We must therefore seek alternate ways of computing the derivatives. To do so, we ask ourselves a basic question. Given a set of grid points $\mathbf{x}_j$ and corresponding function values $\phi_m(\mathbf{x}_j)$, how can we use this data to approximate the derivative of ϕ_m ? The method that immediately comes to mind is a finite difference approximation.

Although possible, a finite difference approximation would be prohibitively expensive. We are a looking for an approximation that would require a minimum amount of sampling points $\mathbf{x}_j$ and yield a high degree of accuracy. Approximating the derivatives by spectral methods is the best we can do.

We are interested in computing the derivatives in the bounded domain $\hat{\Omega}_e$, which we take as a bi-unit square: $[-1,1] \times [-1,1]$. This particular choice is obvious, since ultimately we will be mapping each element to such a square to perform the numerical integration. We take the sampling points $\boldsymbol{\xi}_j$ to be the Chebyshev points,

$$\boldsymbol{\xi}_j = \cos(j\pi/N), \quad j = 0, 1, \ldots, N$$

where $N+1$ is the total number of sampling points in one direction, i.e. $(N+1)^2$ will be the total number of sampling points in the bi-unit square. We can evaluate the derivatives by constructing an appropriate Chebyshev differentiation matrix $\mathbf{D}$ and performing the $(N+1)^2 \times (N+1)^2$ matrix multiplication:

$$\frac{\partial \phi_m}{\partial x_k}(\boldsymbol{\xi}_j) = \mathbf{D}\,\phi_m(\boldsymbol{\xi}_j)$$

The test functions and their derivatives are very complicated and change as a

function of the element Reynolds number. Our numerical experiences indicate that a 9×9 Chebyshev grid is sufficient for accurate evaluation of the test functions, regardless of the element Reynolds number. An alternate method that will provide crucial speedup for some calculations is to implement the Fast Fourier Transform (FFT) to compute the derivatives. Since all the data we are sampling will be real, we can do even better and evaluate the derivatives using a Discrete Cosine Transform (DFT) which is faster than the FFT by a factor of two. Details on how to construct a Chebyshev differentiation matrix or implement the FFT to compute the derivatives of a function can be found in [21].

3.3.2.3 Finite element discretization

We define the finite element model $\bar{\Omega}^h \in R^2$ as the union of non-overlapping quadrilaterals $\mathcal{Q} \in \mathcal{P}_h$. Let $\mathbf{x} = (x_1, x_2) = (x, y)$ be a point in $\bar{\Omega}^h$. With the understanding that all operations are to be carried out on the discretized domain, as a notational shortcut we omit the superscript h on Ω and Γ.

Using the variational form of the incompressible Navier-Stokes given in Section 2.3 we develop the finite element discretization. For the finite element solution we chose subspaces U_h, V_h, and Q_h of the infinite dimensional spaces U, V, and Q respectively. The finite element solution procedure is then:

Find $\mathbf{u}^h \in U_h$, $\mathbf{u}^h(\mathbf{x}, 0) = {}^0\mathbf{u}(\mathbf{x})$, $p^h \in Q_h$ such that for all $\mathbf{v}^h \in V_h$, $q^h \in Q_h$; $t \in (0, \tau]$

$$\int_\Omega \left[\frac{\partial \mathbf{u}^h}{\partial t} + \left(\mathbf{u}^h \cdot \nabla\right)\mathbf{u}^h\right] \cdot \mathbf{v}^h \, d\Omega - \int_\Omega p^h \left(\nabla \cdot \mathbf{v}^h\right) d\Omega + \frac{1}{\mathrm{Re}} \int_\Omega \left[\left(\nabla \mathbf{u}^h\right) + \left(\nabla \mathbf{u}^h\right)^T\right] \cdot \nabla \mathbf{v}^h \, d\Omega = \int_\Omega \mathbf{f} \cdot \mathbf{v}^h \, d\Omega + \int_{\Gamma_f} \mathbf{f}^s \cdot \mathbf{v}^h \, d\Gamma_f \tag{3.28}$$

$$\int_\Omega \left(\nabla \cdot \mathbf{u}^h\right) q^h \, d\Omega = 0 \tag{3.29}$$

where

$$U_h = \left\{ \mathbf{u}^h \in \mathbf{H}^1(\Omega), \mathbf{u}^h|_{\Gamma_u} = \mathbf{u}^s, \mathbf{u}^h \in Q_2 \; \forall \, \mathcal{Q} \in \mathcal{P}_h \right\}$$

$$V_h = \left\{ \mathbf{v}^h \in \mathbf{H}^1(\Omega), \mathbf{v}^h|_{\Gamma_u} = 0, \mathbf{v}^h \in Q_2^* \; \forall \, \mathcal{Q} \in \mathcal{P}_h \right\}$$

$$Q_h = \left\{ q^h \in H^0(\Omega), q^h \in P_1 \text{ or } Q_1 \; \forall \, \mathcal{Q} \in \mathcal{P}_h \right\}$$

Here Q_2 are C^0 biquadratic functions $\{h_m(\mathbf{x})\}_{m=1}^{G_u}$, Q_2^* are C^0 enhanced functions $\{\phi_m(\mathbf{x})\}_{m=1}^{G_u}$, Q_1 are C^0 bilinear functions $\{\varphi_n(\mathbf{x})\}_{n=1}^{G_p}$, and P_1 are C^{-1} linear functions $\{\psi_n(\mathbf{x})\}_{n=1}^{G_p}$, all of them with compact support. G_u and G_p are the number of global nodes for velocity and pressure respectively.

Spatial discretization leads to the following semi-discrete system of equations:

$$\begin{pmatrix} \mathbf{M} & \mathbf{0} & \mathbf{0} \\ \mathbf{0} & \mathbf{M} & \mathbf{0} \\ \mathbf{0} & \mathbf{0} & \mathbf{0} \end{pmatrix} \begin{pmatrix} \dot{\mathbf{u}}_1 \\ \dot{\mathbf{u}}_2 \\ \dot{\mathbf{p}} \end{pmatrix} + \begin{pmatrix} \mathbf{N} + \mathbf{K}^{u_1} & \mathbf{G}^{u_1} & \mathbf{C}^{u_1} \\ \mathbf{G}^{u_2} & \mathbf{N} + \mathbf{K}^{u_2} & \mathbf{C}^{u_2} \\ \mathbf{D}^{u_1} & \mathbf{D}^{u_2} & \mathbf{0} \end{pmatrix} \begin{pmatrix} \mathbf{u}_1 \\ \mathbf{u}_2 \\ \mathbf{p} \end{pmatrix} = \begin{pmatrix} \mathbf{f}^{u_1} + \mathbf{b}^{u_1} \\ \mathbf{f}^{u_2} + \mathbf{b}^{u_2} \\ \mathbf{b}^D \end{pmatrix} \tag{3.30}$$

where $\mathbf{u}_1$ is a vector of length G_u of nodal velocities in the x_1 direction, $\mathbf{u}_2$ is a vector of length G_u of nodal velocities in the x_2 direction, $\mathbf{p}$ is a vector of length G_p of nodal pressures, and the following definitions for the sub-matrices and vectors:

$$M_{ij} = \int_\Omega \phi_i \, h_j \, d\Omega$$

$$N_{ij} = \int_\Omega \phi_i \left(u_1^h \frac{\partial h_j}{\partial x_1} + u_2^h \frac{\partial h_j}{\partial x_2} \right) d\Omega$$

$$K_{ij}^{u_1} = \frac{1}{\mathrm{Re}} \int_\Omega 2 \frac{\partial \phi_i}{\partial x_1} \frac{\partial h_j}{\partial x_1} + \frac{\partial \phi_i}{\partial x_2} \frac{\partial h_j}{\partial x_2} \, d\Omega, \quad K_{ij}^{u_2} = \frac{1}{\mathrm{Re}} \int_\Omega \frac{\partial \phi_i}{\partial x_1} \frac{\partial h_j}{\partial x_1} + 2 \frac{\partial \phi_i}{\partial x_2} \frac{\partial h_j}{\partial x_2} \, d\Omega$$

$$G_{ij}^{u_1} = \frac{1}{\mathrm{Re}} \int_\Omega \frac{\partial \phi_i}{\partial x_2} \frac{\partial h_j}{\partial x_1} \, d\Omega, \qquad G_{ij}^{u_2} = \frac{1}{\mathrm{Re}} \int_\Omega \frac{\partial \phi_i}{\partial x_1} \frac{\partial h_j}{\partial x_2} \, d\Omega$$

$$C_{ij}^{u_1} = -\int_\Omega \frac{\partial \phi_i}{\partial x_1} \psi_j \, d\Omega, \qquad C_{ij}^{u_2} = -\int_\Omega \frac{\partial \phi_i}{\partial x_2} \psi_j \, d\Omega$$

$$D_{ij}^{u_1} = -\int_{\Omega} \psi_i \frac{\partial h_j}{\partial x_1}\, d\Omega, \qquad D_{ij}^{u_2} = -\int_{\Omega} \psi_i \frac{\partial h_j}{\partial x_2}\, d\Omega$$

$$\mathrm{f}_i^{u_1} = \int_{\Omega} \phi_i\, \mathrm{f}_1\, d\Omega + \int_{\Gamma_f} \phi_i\, \mathrm{f}_1^s\, d\Gamma_f, \qquad \mathrm{f}_i^{u_2} = \int_{\Omega} \phi_i\, \mathrm{f}_2\, d\Omega + \int_{\Gamma_f} \phi_i\, \mathrm{f}_2^s\, d\Gamma_f$$

with $\mathbf{b}^{u_1}$, $\mathbf{b}^{u_2}$, and $\mathbf{b}^D$ accounting for the non-zero essential boundary conditions on velocity.

Use of a time integration scheme leads to a nonlinear system of algebraic equations at each time step. The system is solved either by the fixed point iteration or Newton Raphson iteration.

3.3.2.4 Numerical integration

An important part of the evaluation of the sub-matrices and vectors defined above is the integration technique used. The integrals are evaluated using numerical integration in the transformed domain $\hat{\Omega}_e$. Since we are already sampling the functions $\{\phi_m(\mathbf{x})\}$ at Chebyshev points to compute their derivatives , it makes sense to use a numerical quadrature that uses the information at those points. In the field of numerical integration, the Clenshaw-Curtis quadrature is classed as the formula of optimal order based on the fixed set of Chebyshev points $\mathbf{x}_j$ [22, 23] – as opposed to the Gauss-Legendre formula of optimal order based on optimally chosen points. Like Chebyshev spectral differentiation, the Clenshaw-Curtis approximation exhibits spectral accuracy as the number of Chebyshev evaluation points (or quadrature points) increases [21].

Gauss-Legendre quadrature has genuine advantages over the Clenshaw-Curtis quadrature for the evaluation of definite integrals. If we use the Gaussian formula, then the integral will be exact for polynomials of degree $2N-1$, not just N as is the case with Clenshaw-Curtis. However, there is not that much difference when evaluating indefinite integrals and functions that are not smooth [21]. This is better illustrated by some examples. Figure 3-5 illustrates the Clenshaw-Curtis quadrature by integrating $|x^3|$, $\exp(-x^{-2})$, $1/(1+x^2)$, and x^{10} in the interval $[-1,1]$. Figure 3-6

shows the results obtained with the Gauss-Legendre quadrature. Note that for the definite integrals, the convergence surpasses that shown in Figure 3-5, but there is not much difference for the indefinite integral and less smooth function.

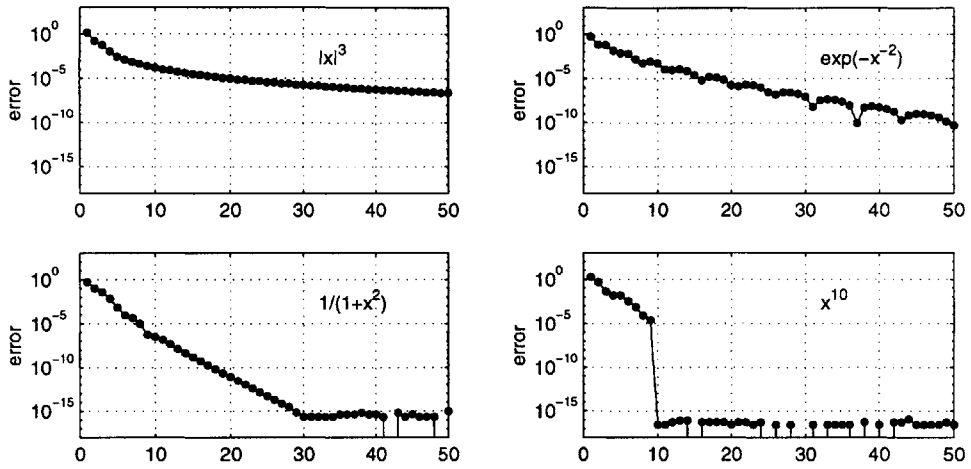

Figure 3-5: Clenshaw-Curtis integration.

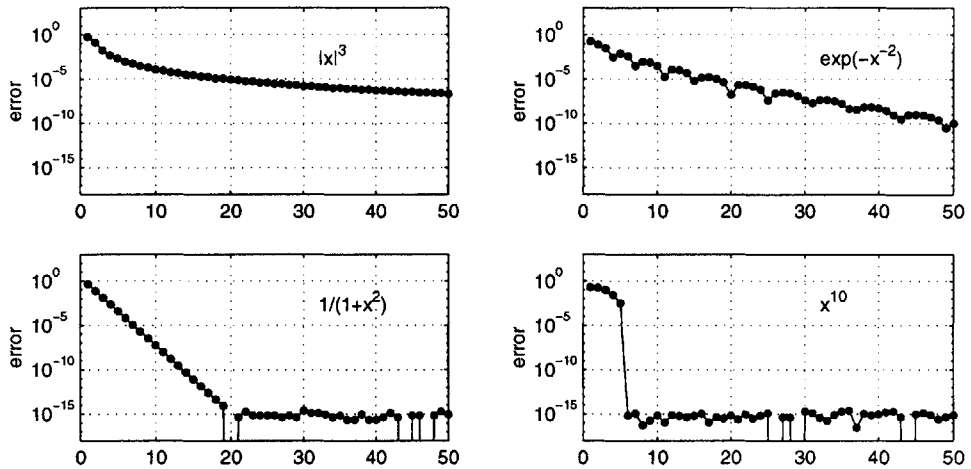

Figure 3-6: Gauss-Legendre integration.

The test functions and their derivatives are very complicated, especially for high Reynolds number flow, and a higher order integration scheme is needed. Furthermore the integrals to be evaluated will be in general indefinite (complicated exponential

functions) and for high Reynolds number flows the integrand may be non-smooth. Hence, either the Clenshaw-Curtis or the Gauss-Legendre quadrature will perform satisfactorily. As mentioned before, we prefer the Clenshaw-Curtis quadrature because we are already sampling values of the test functions and their derivatives at the Chebyshev points.

The order of integration is clearly dependent on the element Reynolds number, however, the number of Chebyshev evaluation points is governed by the need of accurate differentiation of the test functions. Our numerical experiences indicate that a 9×9 Chebyshev grid is needed at all times for an accurate evaluation of the derivatives of the test functions and hence a 9×9 Clenshaw-Curtis quadrature is imposed for the evaluation of the matrices. Expressions for the Clensahw-Curtis quadrature weights can be found in [21].

Clearly the 9×9 integration order requires a considerable computational effort. However, it should be recognized that in computer implementations over ninety percent of the solution effort pertains to the solution of the algebraic equations. Hence, although the computational effort for the element matrix evaluations is significantly higher when compared to the standard 3×3 integration order in traditional finite element formulations, this increase is not significant when measured on the total solution time required.

3.3.3 Simplified LAPG scheme

3.3.3.1 Test functions

To reduce the computational cost associated with evaluating the expressions involving derivatives of the enhanced functions $\{\phi_m(\mathbf{x})\}$, we define the test functions to be equal to the sum of the functions $\{h_m(\mathbf{x})\}$ (which are biquadratic functions) and the enhanced functions $\{\phi_m(\mathbf{x})\}$. This will allow us to take differentiation on $\{h_m(\mathbf{x})\}$ and avoid differentiation on $\{\phi_m(\mathbf{x})\}$.

3.3.3.2 Finite element discretization

Here we take $\mathbf{v} + \mathbf{w}$ to be the test function, and apply integration by parts only to one part of the test function. Further information and remarks on the variational form are presented in Appendix C. The finite element solution procedure is then:

Find $\mathbf{u}^h \in U_h$, $\mathbf{u}^h(\mathbf{x}, 0) = {}^0\mathbf{u}(\mathbf{x})$, $p^h \in Q_h$ such that for all $\mathbf{v}^h + \mathbf{w}^h$ with $\mathbf{v}^h \in V_h$, $\mathbf{w}^h \in W_h$ and for all $q^h \in Q_h$; $t \in (0, \tau]$

$$\begin{aligned}
&\int_\Omega \left[\frac{\partial \mathbf{u}^h}{\partial t} + \left(\mathbf{u}^h \cdot \nabla\right)\mathbf{u}^h\right] \cdot \mathbf{v}^h \, d\Omega - \int_\Omega p^h \left(\nabla \cdot \mathbf{v}^h\right) d\Omega \\
&\qquad + \frac{1}{\mathrm{Re}} \int_\Omega \left[\left(\nabla \mathbf{u}^h\right) + \left(\nabla \mathbf{u}^h\right)^T\right] \cdot \nabla \mathbf{v}^h \, d\Omega \\
&\qquad\qquad + \int_\Omega \left[\frac{\partial \mathbf{u}^h}{\partial t} + \left(\mathbf{u}^h \cdot \nabla\right)\mathbf{u}^h + \nabla p^h - \frac{1}{\mathrm{Re}} \nabla^2 \mathbf{u}^h\right] \cdot \mathbf{w}^h \, d\Omega \\
&\qquad\qquad\qquad = \int_\Omega \mathbf{f} \cdot \mathbf{v}^h \, d\Omega + \int_\Omega \mathbf{f} \cdot \mathbf{w}^h \, d\Omega + \int_{\Gamma_f} \mathbf{f}^s \cdot \mathbf{v}^h \, d\Gamma_f
\end{aligned} \tag{3.31}$$

$$\int_\Omega \left(\nabla \cdot \mathbf{u}^h\right) q^h \, d\Omega = 0 \tag{3.32}$$

where

$$U_h = \left\{\mathbf{u}^h \in \mathbf{H}^1(\Omega), \mathbf{u}^h|_{\Gamma_u} = \mathbf{u}^s, \mathbf{u}^h \in Q_2 \; \forall \, \mathcal{Q} \in \mathcal{P}_h\right\}$$

$$V_h = \left\{\mathbf{v}^h \in \mathbf{H}^1(\Omega), \mathbf{v}^h|_{\Gamma_u} = 0, \mathbf{v}^h \in Q_2 \; \forall \, \mathcal{Q} \in \mathcal{P}_h\right\}$$

$$W_h = \left\{\mathbf{w}^h \in \mathbf{H}^0(\Omega), \mathbf{w}^h \in Q_2^* \; \forall \, \mathcal{Q} \in \mathcal{P}_h\right\}$$

$$Q_h = \left\{q^h \in H^0(\Omega), q^h \in P_1 \text{ or } Q_1 \; \forall \, \mathcal{Q} \in \mathcal{P}_h\right\}$$

We remark that the test functions $\mathbf{v}$ and $\mathbf{w}$ are not applied independently, but together as $\mathbf{v} + \mathbf{w}$. The variational form can also be interpreted as adding to the standard Bubnov-Galerkin formulation the strong form of the incompressible Navier-Stokes equations weighted by the enhanced test functions.

Spatial discretization leads to a similar semi-discrete system of equations as that

in equation (3.30), with the following new definitions for the sub-matrices and vectors:

$$M_{ij} = \int_{\Omega} (h_i + \phi_i)\ h_j \, d\Omega$$

$$N_{ij} = \int_{\Omega} (h_i + \phi_i) \left(u_1^h \frac{\partial h_j}{\partial x_1} + u_2^h \frac{\partial h_j}{\partial x_2} \right) d\Omega$$

$$K_{ij}^{u_1} = \frac{1}{\mathrm{Re}} \int_{\Omega} 2\frac{\partial h_i}{\partial x_1}\frac{\partial h_j}{\partial x_1} + \frac{\partial h_i}{\partial x_2}\frac{\partial h_j}{\partial x_2} \, d\Omega - \frac{1}{\mathrm{Re}} \int_{\Omega} \phi_i \left(\frac{\partial^2 h_j}{\partial x_1^2} + \frac{\partial^2 h_j}{\partial x_2^2} \right) d\Omega$$

$$K_{ij}^{u_2} = \frac{1}{\mathrm{Re}} \int_{\Omega} \frac{\partial h_i}{\partial x_1}\frac{\partial h_j}{\partial x_1} + 2\frac{\partial h_i}{\partial x_2}\frac{\partial h_j}{\partial x_2} \, d\Omega - \frac{1}{\mathrm{Re}} \int_{\Omega} \phi_i \left(\frac{\partial^2 h_j}{\partial x_1^2} + \frac{\partial^2 h_j}{\partial x_2^2} \right) d\Omega$$

$$G_{ij}^{u_1} = \frac{1}{\mathrm{Re}} \int_{\Omega} \frac{\partial h_i}{\partial x_2}\frac{\partial h_j}{\partial x_1} \, d\Omega, \qquad G_{ij}^{u_2} = \frac{1}{\mathrm{Re}} \int_{\Omega} \frac{\partial h_i}{\partial x_1}\frac{\partial h_j}{\partial x_2} \, d\Omega$$

$$C_{ij}^{u_1} = -\int_{\Omega} \frac{\partial h_i}{\partial x_1}\psi_j \, d\Omega + \int_{\Omega} \phi_i \frac{\partial \psi_j}{\partial x_1} \, d\Omega, \qquad C_{ij}^{u_2} = -\int_{\Omega} \frac{\partial \phi_i}{\partial x_2}\psi_j \, d\Omega + \int_{\Omega} \phi_i \frac{\partial \psi_j}{\partial x_2} \, d\Omega$$

$$D_{ij}^{u_1} = -\int_{\Omega} \psi_i \frac{\partial h_j}{\partial x_1} \, d\Omega, \qquad D_{ij}^{u_2} = -\int_{\Omega} \psi_i \frac{\partial h_j}{\partial x_2} \, d\Omega$$

$$\mathrm{f}_i^{u_1} = \int_{\Omega} (h_i + \phi_i)\ \mathrm{f}_1 \, d\Omega + \int_{\Gamma_f} h_i \, \mathrm{f}_1^s \, d\Gamma_f, \qquad \mathrm{f}_i^{u_2} = \int_{\Omega} (h_i + \phi_i)\ \mathrm{f}_2 \, d\Omega + \int_{\Gamma_f} h_i \, \mathrm{f}_2^s \, d\Gamma_f$$

3.3.3.3 Numerical integration

The use of a 9×9 Chebyshev grid and consequently a 9×9 Clenshaw-Curtis quadrature in the LAPG scheme was mainly driven by the need to obtain high accuracy in the evaluation of the derivatives of the enhanced test functions. In this simplified version of the LAPG scheme (S-LAPG scheme) the derivatives of the test functions $\{\phi_m(\mathbf{x})\}$ do not appear in the finite element solution procedure, and hence a significant computational saving is achieved in the numerical evaluation of the finite element matrices.

In general, the required order of integration is dependent on the element Reynolds number. However, a 9×9 Clenshaw-Curtis quadrature is still recommended to eval-

uate the finite element matrices containing the enhanced test functions. Of course, now that there is no need to evaluate derivatives of the enhanced test functions we are free to choose any other quadrature and a 9×9 Gauss-Legendre quadrature could be used as well. There is not much to be gained by using one or the other for expressions involving the enhanced test function, however the usual 3×3 Gauss-Legendre quadrature should be used for the other finite element matrices.

In the interest of computational efficiency the following formula for the Clenshaw-Curtis or Gauss-Legendre integration order can be used:

$$\text{Integration Order} = \begin{cases} 3 \times 3 & \text{if } 10^{-6} \leq \max(|Ah|, |Bk|) \leq 1.0, \\ 5 \times 5 & \text{if } 1.0 < \max(|Ah|, |Bk|) \leq 5.0, \\ 7 \times 7 & \text{if } \max(|Ah|, |Bk|) > 5.0. \end{cases} \tag{3.33}$$

Hence, the maximum integration order is 7×7 and the element matrices may exhibit spurious eigenvalues for high Reynolds number flows.

3.3.4 Exponential/Flow-condition-based interpolation (FCBI) scheme

3.3.4.1 Test functions

In this approach we establish the test functions $\{\phi_m(\mathbf{x})\}$ by taking the tensor product of one-dimensional functions based on a linear-exponential basis, equations (3.2) and (3.3), along the element edge- and mid-lines [24].

Consider a typical 9-node rectangular element $\mathcal{Q} \in \mathcal{P}_h$, shown in Figure 3-7, with dimensions $2h$ and $2k$ as shown.

We assume the following functions along the edge- and mid-lines of the element: for the three functions along lines 2-5-1, 6-9-8, and 3-7-4 in the variable x

$$\phi_i(x) = a_i \left(e^{2A_i x} - 1\right) + b_i\, x + c_i, \qquad i = 1, 2, 3 \tag{3.34}$$

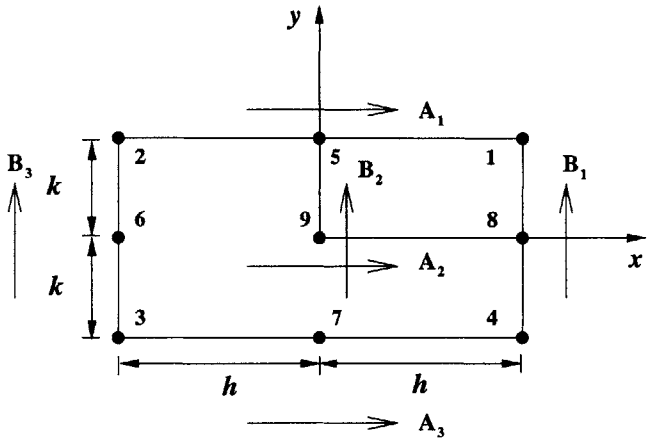

Figure 3-7: Rectangular element with 9 nodes.

for the three functions along lines 4-8-1, 7-9-5, and 3-6-2 in the variable y

$$\phi_i(y) = d_i \left(e^{2B_i y} - 1\right) + e_i\, y + f_i, \qquad i = 1, 2, 3 \tag{3.35}$$

where

$$2A_i = \mathrm{Re}\, u_1 \qquad 2B_i = \mathrm{Re}\, u_2 \tag{3.36}$$

v_1 and v_2 are average velocities along the lines considered and the constants are determined using the conditions at the nodes. Another option would be to let v_1 and v_2 be the velocities at the node at which the test functions are being constructed, in this case we would have nine different functions in x and nine different functions in y for a typical 9-node element. In either case, the procedures described here are equally applicable.

Normalizing these functions to have the Kronecker delta property at the nodes we obtain along an edge or mid-line the generic interpolation functions

$$f_1(x) = \frac{\left(e^{2Ax} - 1\right)}{4\sinh^2 Ah} - \frac{x}{2h} - \frac{x}{2h}\coth Ah \tag{3.37}$$

$$f_2(x) = -\frac{2\left(e^{2Ax}-1\right)}{4\sinh^2 Ah} - \frac{x}{h}\coth Ah + 1 \tag{3.38}$$

$$f_3(x) = \frac{\left(e^{2Ax}-1\right)}{4\sinh^2 Ah} + \frac{x}{2h} - \frac{x}{2h}\coth Ah \tag{3.39}$$

$$g_1(y) = \frac{\left(e^{2By}-1\right)}{4\sinh^2 Bk} - \frac{y}{2k} - \frac{y}{2k}\coth Bk \tag{3.40}$$

$$g_2(y) = -\frac{2\left(e^{2By}-1\right)}{4\sinh^2 Bk} - \frac{y}{k}\coth Bk + 1 \tag{3.41}$$

$$g_3(y) = \frac{\left(e^{2By}-1\right)}{4\sinh^2 Bk} + \frac{y}{2k} - \frac{y}{2k}\coth Bk \tag{3.42}$$

where $f_i(x)$ and $g_i(y)$ are the one-dimensional interpolation functions along the x and y directions respectively.

Figure 3-8 shows the functions for the element Reynolds numbers 10^{-5}, 10, and 100. Note that for very small element Reynolds number these interpolations are the usual parabolic functions and that as the element Reynolds number increases the functions skew towards the upstream side.

A test function is now obtained by simply taking the tensor product of the edge-line and mid-line functions established above; for example, for node 7 in Figure 3-7, we use the normalized edge function for edge 3-7-4 multiplied by the normalized function for mid-line 7-9-5. As an illustrative example, consider the special case when $A_i = A$ and $B_i = B$. The test functions $\{\phi_m(\mathbf{x})\}$ are now established by simply taking the tensor product of the generic one-dimensional functions as follows

$$\begin{aligned}
\phi_1(\mathbf{x}) &= f_3(x)\, g_3(y) & \qquad \phi_5(\mathbf{x}) &= f_2(x)\, g_3(y) \\
\phi_2(\mathbf{x}) &= f_1(x)\, g_3(y) & \qquad \phi_6(\mathbf{x}) &= f_1(x)\, g_2(y) \\
\phi_3(\mathbf{x}) &= f_1(x)\, g_1(y) & \qquad \phi_7(\mathbf{x}) &= f_2(x)\, g_1(y) \\
\phi_4(\mathbf{x}) &= f_3(x)\, g_1(y) & \qquad \phi_8(\mathbf{x}) &= f_3(x)\, g_2(y) \\
 & & \qquad \phi_9(\mathbf{x}) &= f_2(x)\, g_2(y)
\end{aligned} \tag{3.43}$$

For distorted elements the procedures and definitions described in Section 3.2.1 apply.

Representative values of the parameters in equation (3.15) are chosen at the geometric center of the element mid- or edge-line under consideration.

In this approach there is no need to add a bubble function, because the tensor product of the one-dimensional interpolation functions provides us with one. Furthermore, the bubble function obtained in this approach does respond to the flow conditions over the element (see Figure 3-10), as opposed to the x^2, y^2 in the LAPG scheme.

Consider the two 9 node element patch (see Figures 3-9a and 3-10a). In the case of pure diffusion the test functions of nodes A and B are symmetric (Figures 3-9b and 3-10b) and collapse to the usual biquadratic test function. Figures 3-9c and 3-10c show the test functions when convection is present, for the case of flow in the positive x direction. Figures 3-9d and 3-10d show the functions for flow at an angle, both x and y components of velocity are present. Figure 3-9 is to be compared with Figure 3-4, where the test functions were established by means of equation (3.24).

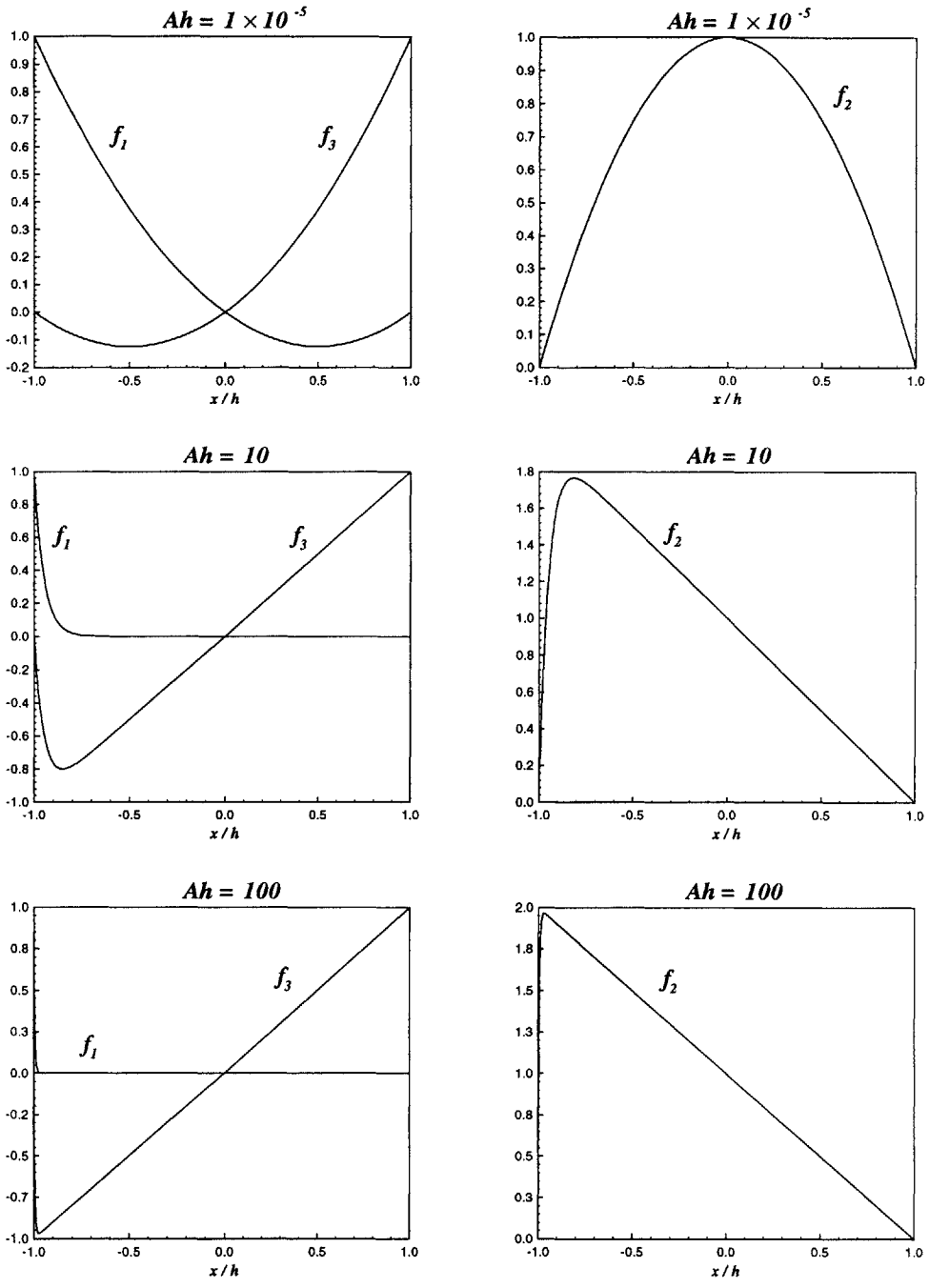

Figure 3-8: One-dimensional test functions.

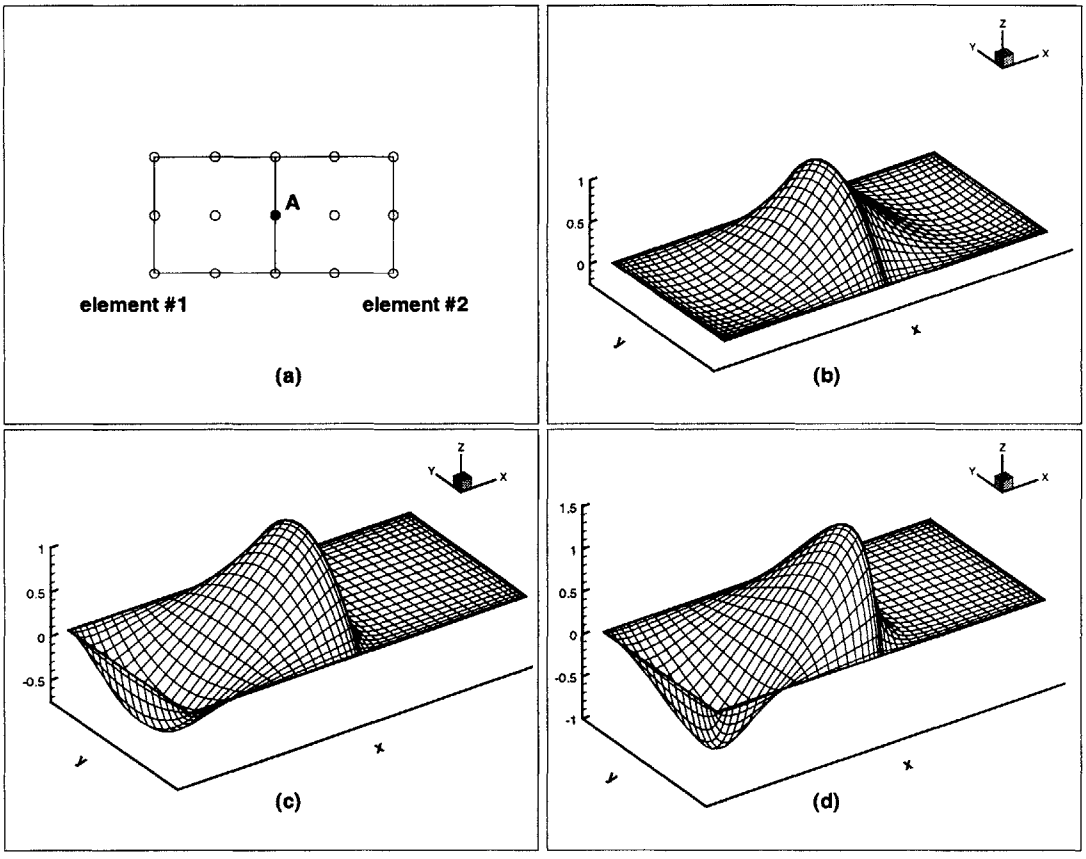

Figure 3-9: Test function for node A in the two element patch in (a). In the case of pure diffusion the test function is symmetric (b). In (c) convection is present, flow is strictly in the positive x direction. In (d) convection is present in the positive x and y directions, flow at a 30° angle from the x axis.

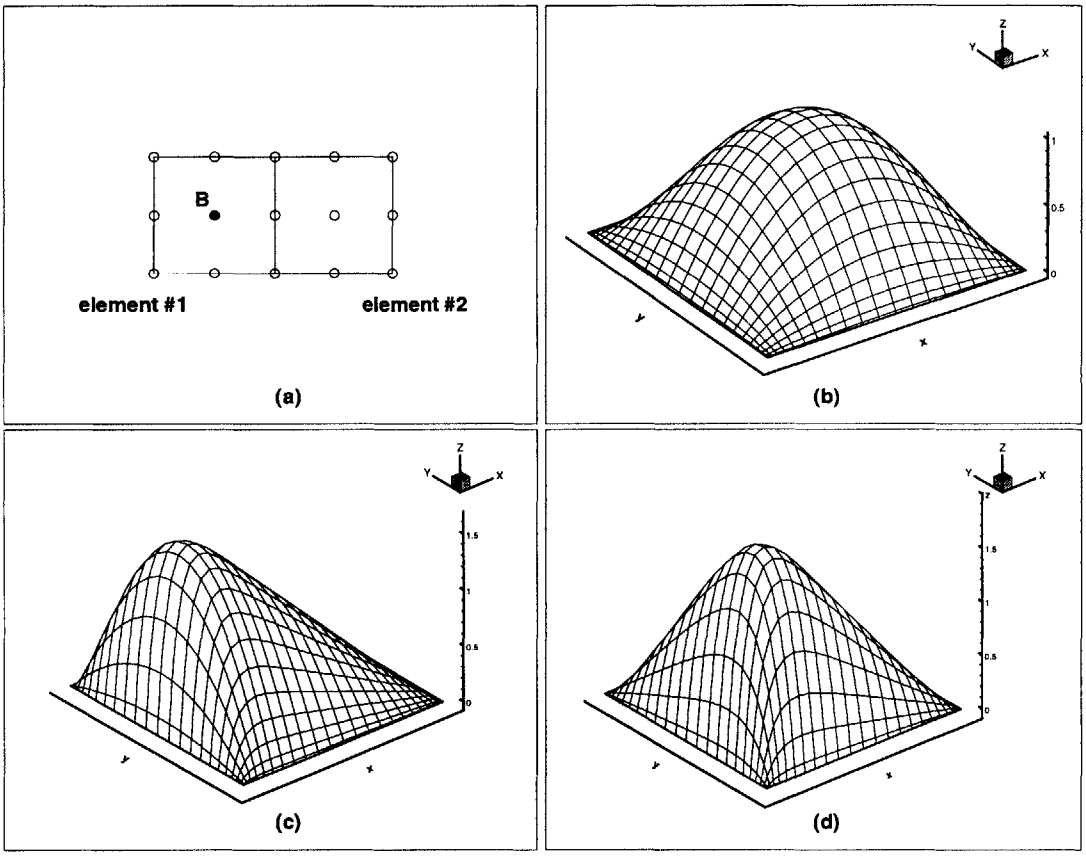

Figure 3-10: Test function for node B in the two element patch in (a). In the case of pure diffusion the test function is symmetric (b). In (c) convection is present, flow is strictly in the positive x direction. In (d) convection is present in the positive x and y directions, flow at a 30° angle from the x axis.

3.3.4.2 Differentiation of the test functions

The differentiation of the test functions is straightforward and can be expressed in terms of one-dimensional products as follows:

$$\begin{aligned}
\frac{\partial \phi_1}{\partial x}(\mathbf{x}) &= \frac{\partial f_3}{\partial x} g_3 & \frac{\partial \phi_1}{\partial y}(\mathbf{x}) &= f_3 \frac{\partial g_3}{\partial y} \\
\frac{\partial \phi_2}{\partial x}(\mathbf{x}) &= \frac{\partial f_1}{\partial x} g_3 & \frac{\partial \phi_2}{\partial y}(\mathbf{x}) &= f_1 \frac{\partial g_3}{\partial y} \\
\frac{\partial \phi_3}{\partial x}(\mathbf{x}) &= \frac{\partial f_1}{\partial x} g_1 & \frac{\partial \phi_3}{\partial y}(\mathbf{x}) &= f_1 \frac{\partial g_1}{\partial y} \\
&\ldots \text{ etc.} & &\ldots \text{ etc.}
\end{aligned} \tag{3.44}$$

Unlike the LAPG scheme where the differentiation of the test functions has to be performed numerically using a Chebyshev grid, differentiation of the test functions is carried out analytically and can be efficiently evaluated as products of functions as shown above.

3.3.4.3 Finite element discretization

The finite element discretization is exactly the same as described in Section 3.3.2.3 but with the new definition for the test functions $\{\phi_m(\mathbf{x})\}$.

3.3.4.4 Numerical integration

For low Reynolds number flow the test functions conveniently collapse to the usual bi-quadratics and a 3×3 Gauss-Legendre integration quadrature is acceptable. For high Reynolds number flow, the test functions are more complicated and a higher order integration scheme is needed. The required order is clearly dependent on the element Reynolds number. However, the "full" 9×9 Clenshaw-Curtis or Gauss-Legendre quadrature is recommended for the numerical evaluation of the finite element matrices.

In the interest of computational efficiency and with the risk of spurious eigenvalues in the numerical representation of the finite element matrices for high Reynolds num-

ber flows and/or highly distorted elements, the following formula for the Clenshaw-Curtis or Gauss-Legendre integration order can be used:

$$\text{Integration Order} = \begin{cases} 3 \times 3 & \text{if } 10^{-5} \leq \max(|Ah|, |Bk|) \leq 2.5, \\ 5 \times 5 & \text{if } 2.5 < \max(|Ah|, |Bk|) \leq 5.0, \\ 7 \times 7 & \text{if } \max(|Ah|, |Bk|) > 5.0. \end{cases} \tag{3.45}$$

3.4 Inf-sup test

In this section we prove the stability of the proposed Petrov-Galerkin schemes (LAPG and FCBI) using the inf-sup test for advection-diffusion problems proposed by Bathe et al. [25]. The performance of a stabilized scheme can be evaluated by looking at the results of an example problem and check if the solution contains oscillations. However, the inf-sup test for advection-diffusion problems provides more insight than just measuring the oscillations in the solution.

The inf-sup test is based on the one-dimensional advection-diffusion problem, which corresponds to a constant prescribed velocity throughout the domain and prescribed temperatures at both ends of the domain. The test compactly describes the stability of the scheme as the Peclet number and element size are varied.

In the case of one-dimensional flow the LAPG and FCBI schemes can be tested by using their element edge functions, which in both cases are linear-exponential functions. Hence, in this section we will simply refer to the one-dimensional scheme as the Exponential/Flow-condition-based interpolation (FCBI) scheme. For example, for a typical 3-node element of length $2h$ the test functions are of the form:

$$\begin{aligned} \phi_1(x) &= \frac{\left(e^{2Ax} - 1\right)}{4\sinh^2 Ah} - \frac{x}{2h} - \frac{x}{2h}\coth Ah \\ \phi_2(x) &= -\frac{2\left(e^{2Ax} - 1\right)}{4\sinh^2 Ah} - \frac{x}{h}\coth Ah + 1 \\ \phi_3(x) &= \frac{\left(e^{2Ax} - 1\right)}{4\sinh^2 Ah} + \frac{x}{2h} - \frac{x}{2h}\coth Ah \end{aligned} \tag{3.46}$$

Note that in the case of one-dimensional flow the two-dimensional FCBI test functions collapse to the one-dimensional test functions in the interior of the element. This results from the fact that the test functions in the interior of the element were obtained by taking the tensor product of the edge- and mid-line functions. On the other hand, in the case of one-dimensional flow the two-dimensional LAPG test functions do not collapse to the one-dimensional functions in the interior of the element. This is because they were constructed specifically to emulate local analytic two-dimensional behavior in the interior of the element. This does not mean that the LAPG test functions cannot respond to one-dimensional flow, it simply means that they do not collapse to the specific form given by equations (3.46) in the interior of the element. However, if the LAPG formulation were developed for one-dimensional flow, equations (3.46) would be obtained. An analysis of the one-dimensional advection-diffusion problem with the FCBI scheme is presented in Appendix D.

The results of the inf-sup test are shown in Figures 3-11, 3-12, and 3-13. In these plots h is the element length and Pe is the Peclet number. Figure 3-11 shows that as the mesh is made coarser (we follow the curves from left to right), the inf-sup value corresponding the Bubnov-Galerkin formulation decreases. This trend indicates that the formulation does not pass the inf-sup test. The formulation is predicted to become unstable as the mesh is made coarser. This instability is displayed by oscillations in the solution. Figure 3-11 also shows that as the mesh is made finer the inf-sup value corresponding to the Bubnov-Galerkin formulation approaches a fixed value of $\log_{10}(\text{inf-sup}) = 0.5$. This indicates that, as already expected, the formulation becomes stable as the mesh is refined. Figure 3-11 also shows that as the mesh is refined, the inf-sup value corresponding to the FCBI formulation is bounded from below. This indicates that the formulation passes the inf-sup test.

Figure 3-12 shows that as the Peclet number increases, the inf-sup value of the Bubnov-Galerkin formulation decreases unboundedly. This means that the formulation does not pass the inf-sup test, which agrees with our earlier observation. Figure 3-12 also shows that as the Peclet number increases, the inf-sup value of the FCBI formulation is bounded from below. This means that the formulation passes the inf-sup

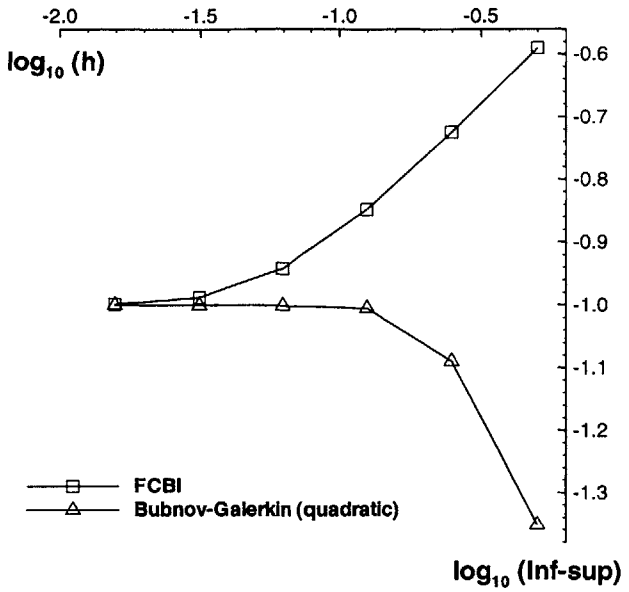

Figure 3-11: Inf-sup value curves as the mesh is coarsened for Pe = 100.

test.

In Figure 3-13 we plot the inf-sup curves corresponding to several stabilized finite element formulations. Figure 3-13 shows that as the mesh is made coarser the inf-sup value for the Exponential/Flow-condition-based interpolation (FCBI), Galerkin/Least-Squares (GLS), and Full Upwind (FU) formulations is bounded from below, meaning that they pass the inf-sup test. We can see from the plot that the FU formulation introduces the largest amount of artificial diffusion, while the FCBI scheme introduces little or no artificial diffusion. We also note that the FCBI scheme is stable but small oscillations occur in the solution because the method has too little artificial diffusion. This can be seen by comparing the curve corresponding to this method with the one corresponding to the GLS formulation, which gives a nodally exact solution.

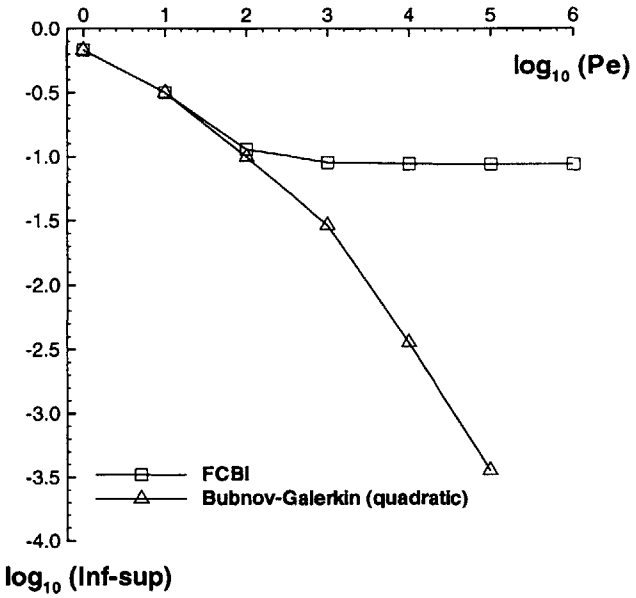

Figure 3-12: Inf-sup value curves as Pe is increased for 16 equal sized elements.

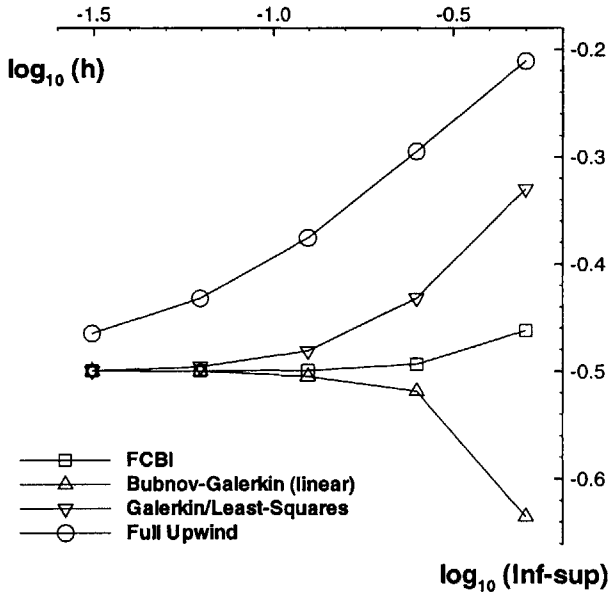

Figure 3-13: Inf-sup value curves as the mesh is coarsened for Pe = 10.

Chapter 4

Numerical examples

4.1 Introduction

In this chapter we solve several test problems with the discretization schemes described in the previous chapter. In the absence of a deep theoretical analysis of the discretization schemes, it is very important to solve well-chosen test problems. The numerical problems are designed to test the numerical stability of the schemes at low and high Reynolds number. We also evaluate their accuracy by comparing the numerical results with benchmark solutions when these are available.

Before going into the presentation and discussion of the numerical results it is instructive to briefly describe the numerical solution procedure of the non-linear system of equations resulting from the application of any of the discretization schemes described in the previous chapter. Upon linearization of the convective term in the Navier-Stokes equations, either by a fixed point iteration scheme or a Newton Raphson scheme, we face the factorization of an indefinite, non-symmetric, sparse, and banded matrix. The absence of pressure in the continuity equation results in zeros along the main diagonal (which makes the matrix indefinite). This forces us to use some kind of pivoting for numerical stability during the factorization process. We also note that the resulting matrix is sparse (which will result in less storage) and banded (meaning that all the nonzero elements are close to the diagonal). Finally the matrix is non-symmetric. Here we use Banded Gauss Elimination with Partial

Pivoting (BGEPP) to factorize the resulting matrix. To minimize the bandwith we apply a Reverse Cuthill-McKee permutation before the BGEPP. Further details on the numerical solution of sparse linear system of equations can be found in [26].

4.2 Distorted Elements

An important requirement for the discretization schemes is that they can be depended upon when the elements are used in geometrically distorted form. To evaluate the capability of the discretization schemes we consider in Figure 4-1 the solution of laminar flow in a duct, $0 \leq x \leq 2$, $0 \leq y \leq 1$, with highly distorted elements. A parabolic velocity profile is specified at the inlet, zero pseudo-tractions are specified at the outlet, and the velocities are set to zero at the horizontal walls.

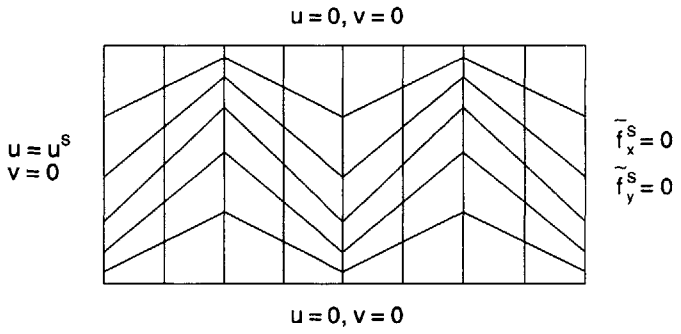

Figure 4-1: Geometry, mesh, and boundary conditions for flow in a duct.

Excellent results are obtained with the LAPG, S-LAPG, and FCBI formulations with either 9/3 or 9/4-c elements. The computed pressure drop is exactly equal to the analytic pressure drop for all Reynolds number considered from 1×10^{-3} to 1×10^{6}. Figure 4-2 shows the smooth pressure contours obtained using the FCBI formulation with 9/4-c elements for a range of Reynolds numbers up to 1×10^{6}. There is definite improvement over the Bubnov-Galerkin formulation where, even for the simple flow conditions considered here, a solution can only be obtained up to Reynolds number 1×10^{4}. The excellent results also validate the procedures to establish the

test functions for geometrically distorted elements outlined in the previous chapter and discussed in more detail in Appendix B.

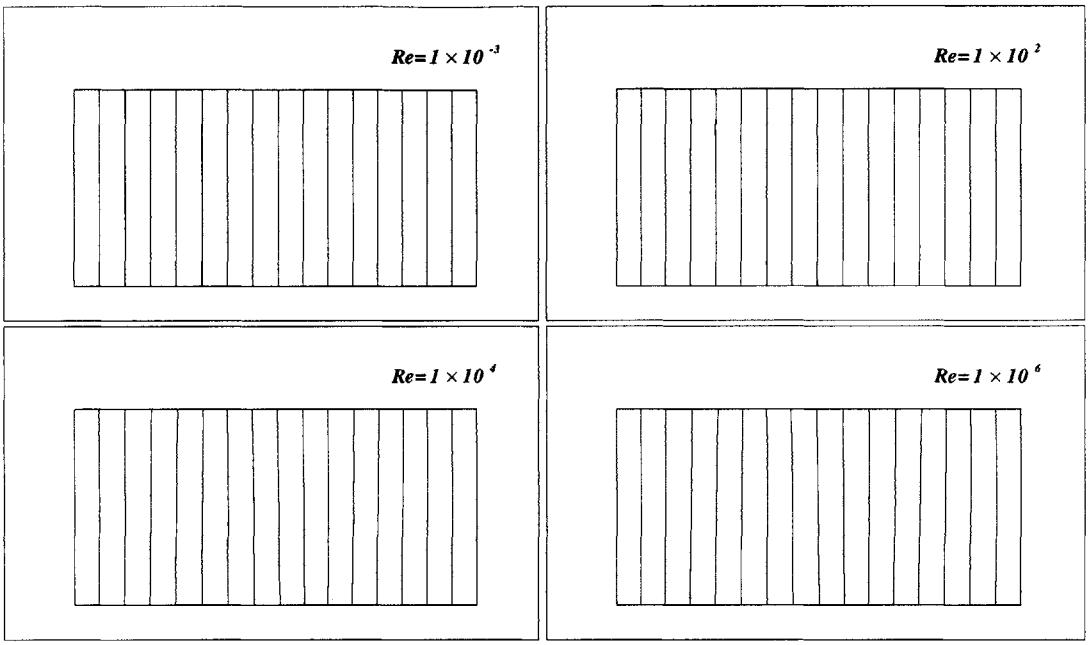

Figure 4-2: Pressure contour plots for Re $= 1 \times 10^{-3}$, 1×10^{2}, 1×10^{4}, and 1×10^{6}. FCBI scheme using 9/4-c elements.

On the other hand, the FAFE scheme does not perform well when the elements are used in such highly non-orthogonal distorted form. This was to be expected since in the FAFE scheme the momentum equations are discretized using the finite analytic approach, which requires that the mesh have the highest degree of orthogonality possible. A solution is obtained for Reynolds number up to 1×10^{6}, however the pressure is not well predicted for Re $> 1 \times 10^{2}$.

4.3 Lid-driven cavity flow

The lid-driven cavity flow problem has been used extensively as a test problem because of its complex flow physics and simple geometry. The incompressible fluid is bounded in a square enclosure and the flow is driven by the uniform translation of the top boundary. The flow configurations generated in the cavity show rich vortex phenomena at many scales depending on the Reynolds number. These recirculating regions make this an interesting and challenging problem. A unit square with a non-uniform 30×30 element mesh, shown in Figure 4-3, is used for the computations. Since velocity is prescribed on the entire boundary of the cavity, the pressure is undetermined unless it is prescribed at one point. We prescribe zero pressure at the lower right corner of the cavity.

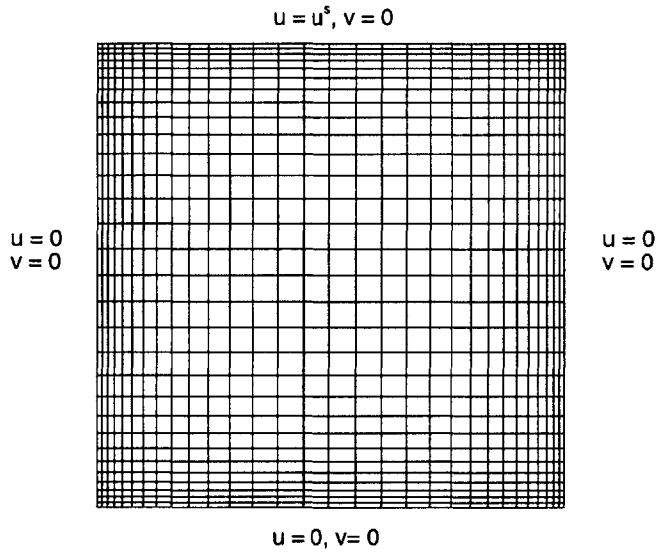

Figure 4-3: Mesh and boundary conditions for the lid-driven cavity problem.

Most published numerical solutions of two-dimensional cavity flows use a vorticity-stream function formulation. Among the previous research, Ghia et al. [27] obtained numerical solutions up to Reynolds number 1×10^4 with a 257×257 grid. Their work represents the most comprehensive study of the 2-D cavity flow to date.

Here, we perform a steady state analysis for Reynolds number up to 1×10^4 and continue with an unsteady analysis up to a Reynolds number of 1×10^6. The four schemes perform extremely well for the steady state analyses up to Reynolds number 1×10^4. Figure 4-4 shows plots of the streamlines for Reynolds number up to 1×10^4 computed with the LAPG scheme using 9/3 elements. It is apparent that the flow structure is in good agreement with Ghia et al. These plots give a clear picture of the overall flow pattern and the effect of Reynolds number on the structure of the recirculating eddies in the cavity. In addition to the central vortex, a pair of counter rotating eddies of much smaller strength develop in the lower corners at Re = 400. At Re = 5000, a third secondary vortex is observed in the upper left corner. For Re $= 1 \times 10^4$ a tertiary vortex appears in the lower right hand corner. As Re increases, from Re = 100, the primary vortex center moves towards the right and becomes increasingly circular. This center moves down towards the geometric center of the cavity as Re increases and becomes fixed in its x location for Re $\geq$ 5000.

In Figures 4-5 and 4-7 we compare the horizontal and vertical velocity profiles through the vertical and horizontal mid-sections of the cavity obtained by the simplified LAPG (S-LAPG) scheme using 9/3 elements with the benchmark solution of Ghia et al. [27]. It is clear that the numerical results are in good agreement with Ghia et al. Figures 4-6 and 4-8 show the pressure profiles through the vertical and horizontal mid-sections of the cavity respectively. In these figures and in the figures throughout the chapter, we plot dimensionless velocities and pressure (see Chapter 2); i.e., the velocities are normalized by a characteristic velocity U which we set to unity and the pressure by ρU^2.

As the Reynolds number is increased above 1×10^4, the flow becomes unsteady. The only scheme that did not become numerically unstable up to Reynolds number 1×10^6 was the FAFE scheme. Figure 4-9 shows plots of the instantaneous velocity and pressure fields predicted by the FAFE scheme for Reynolds number 1×10^6. At this Reynolds number the core of the primary vortex changes its shape and rotates with time. Figure 4-10 shows instantaneous horizontal and vertical velocity profiles through the vertical and horizontal mid-sections of the cavity. Figure 4-11 shows the

instantaneous pressure profiles through the vertical and horizontal mid-sections of the cavity.

Table 4.1 summarizes the relative performance of the four schemes in solving the lid-driven cavity problem using the mesh shown in Figure 4-3. The column in the table labeled BG denotes the Bubnov-Galerkin formulation. The table is representative of analyses performed with both the 9/3 and 9/4-c elements. For steady state analyses "$\surd$" denotes convergence to within a tolerance of 1×10^{-6} and "—" denotes failure to converge due to numerical instabilities. Convergence is based on the normalized norm of the residuals in velocities: $\|\Delta \mathbf{u}^h\| / \|\mathbf{u}^h\|$.

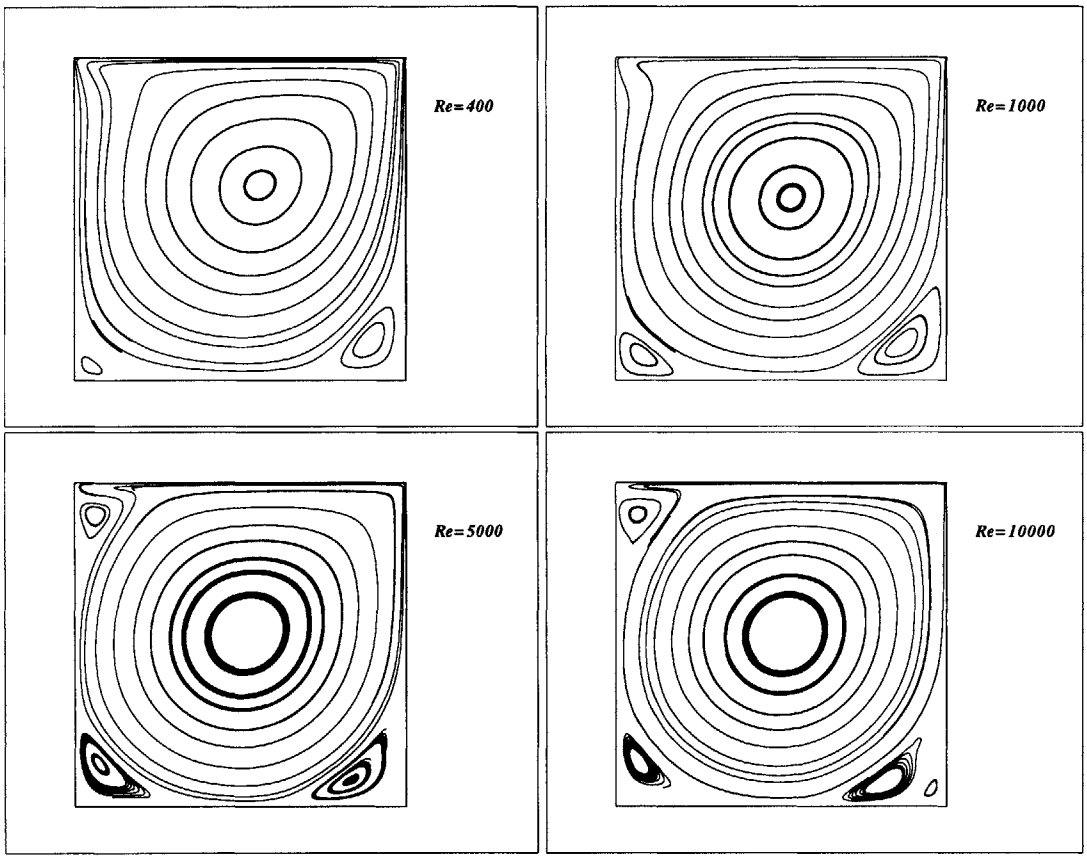

Figure 4-4: Contour plots showing streamlines for Re = 400, 1000, 5000, and 1×10^4. LAPG scheme using 9/3 elements.

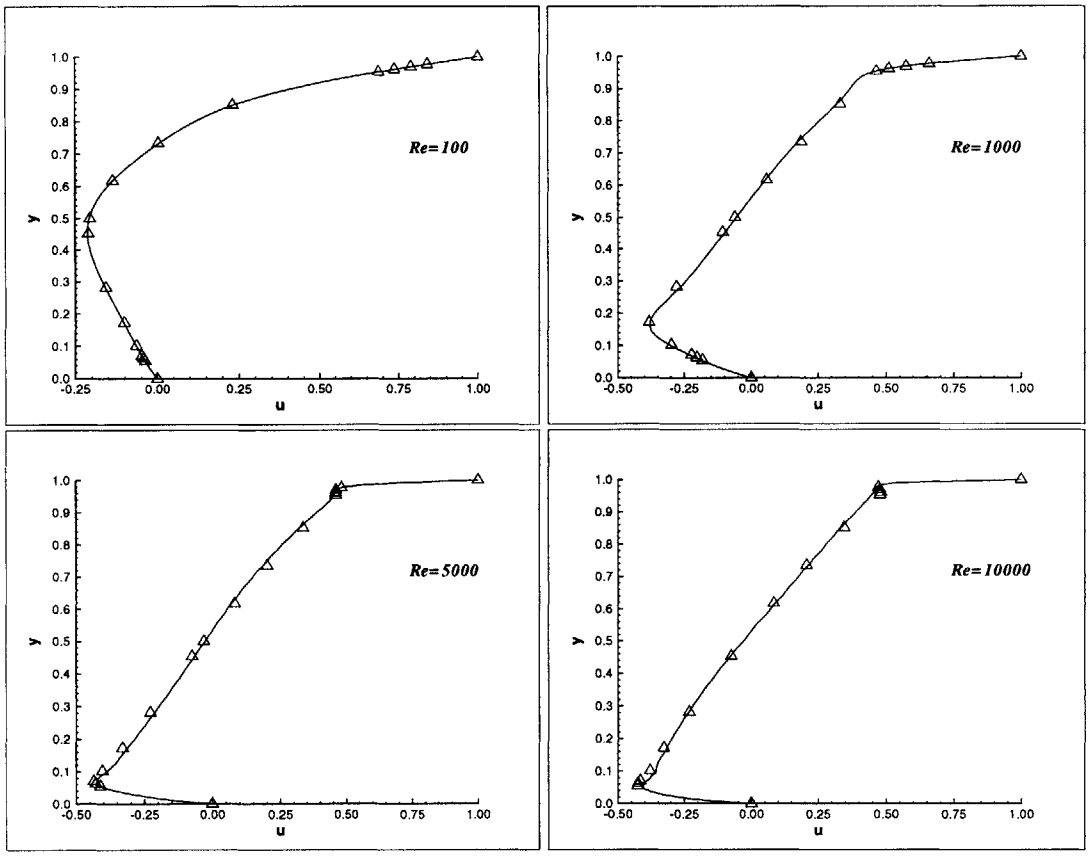

Figure 4-5: Normalized horizontal velocity profiles along the vertical mid-section of the cavity: — computed, △ Ghia et al. [27]. S-LAPG scheme using 9/3 elements.

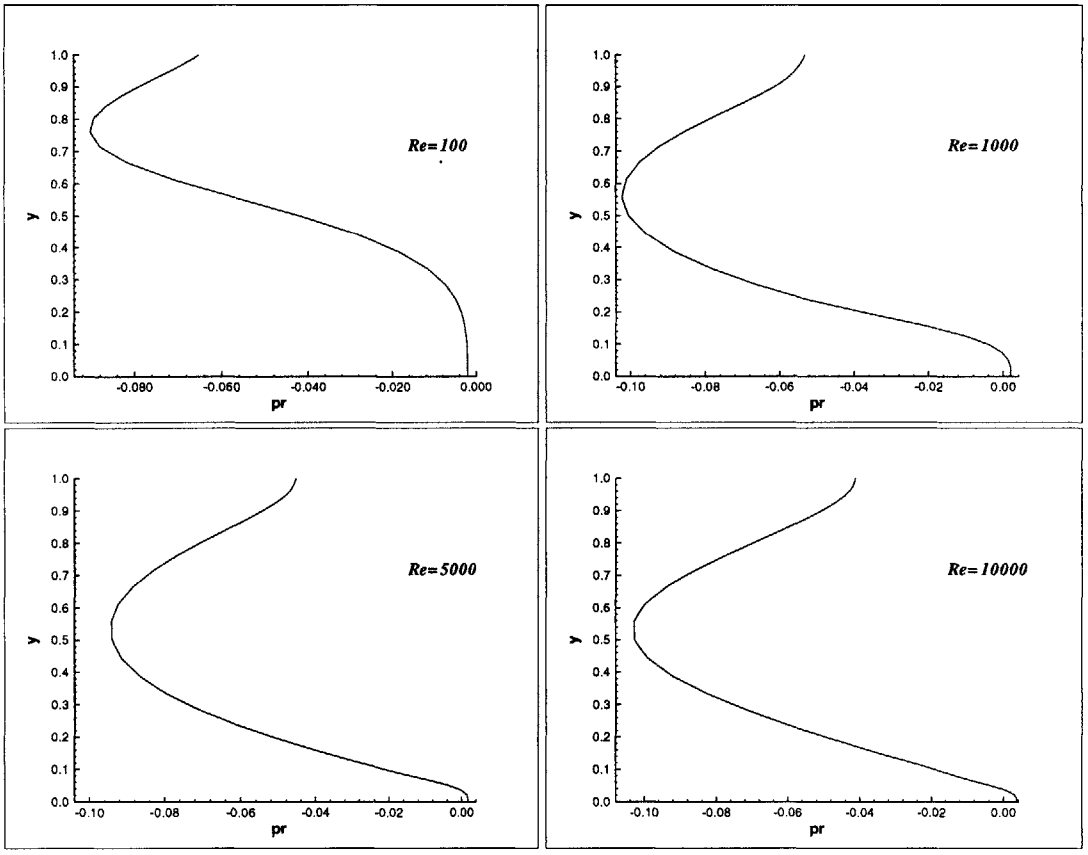

Figure 4-6: Normalized pressure profiles along the vertical mid-section of the cavity. S-LAPG scheme using 9/3 elements.

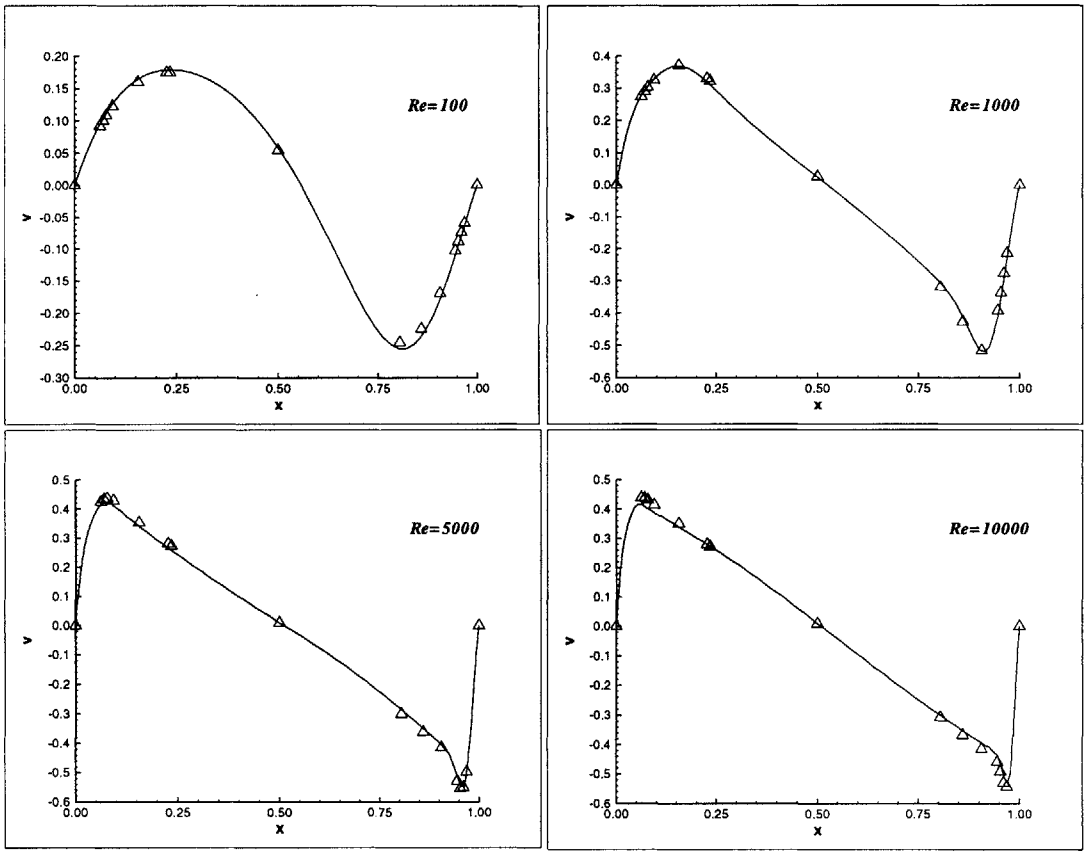

Figure 4-7: Normalized vertical velocity profiles along the horizontal mid-section of the cavity: — computed, △ Ghia et al. [27]. S-LAPG scheme using 9/3 elements.

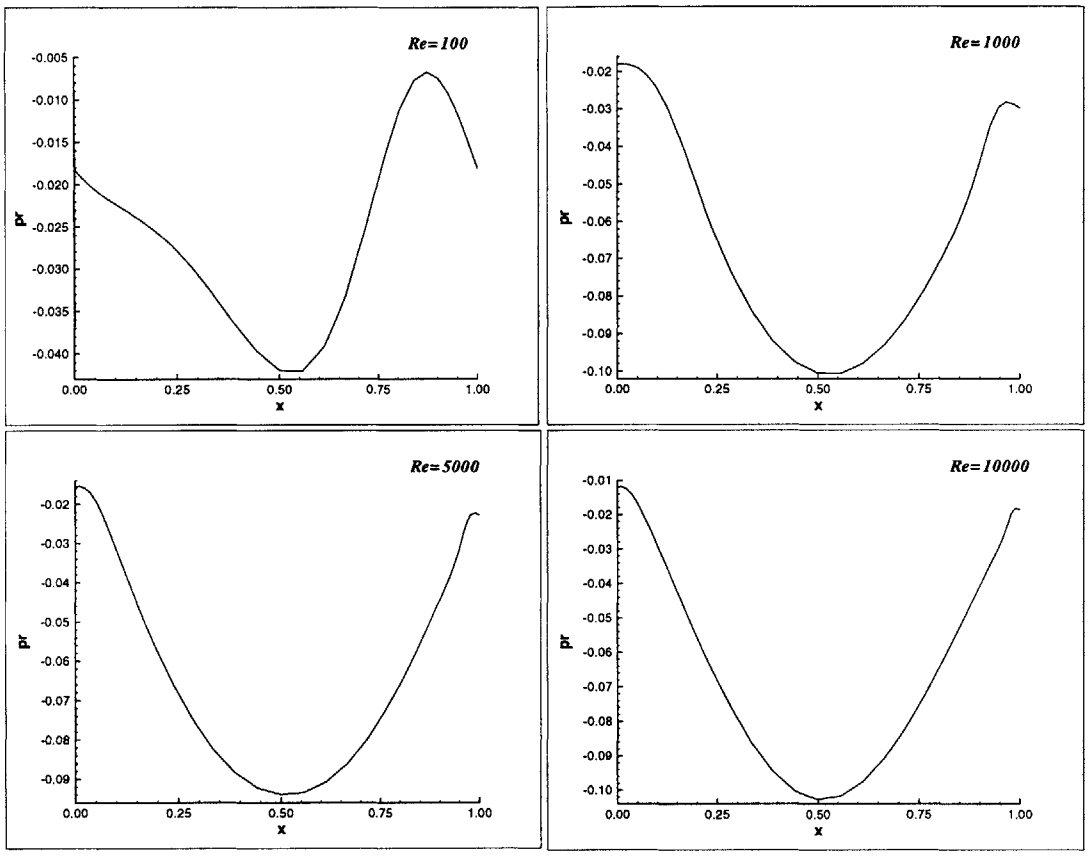

Figure 4-8: Normalized pressure profiles along the horizontal mid-section of the cavity. S-LAPG scheme using 9/3 elements.

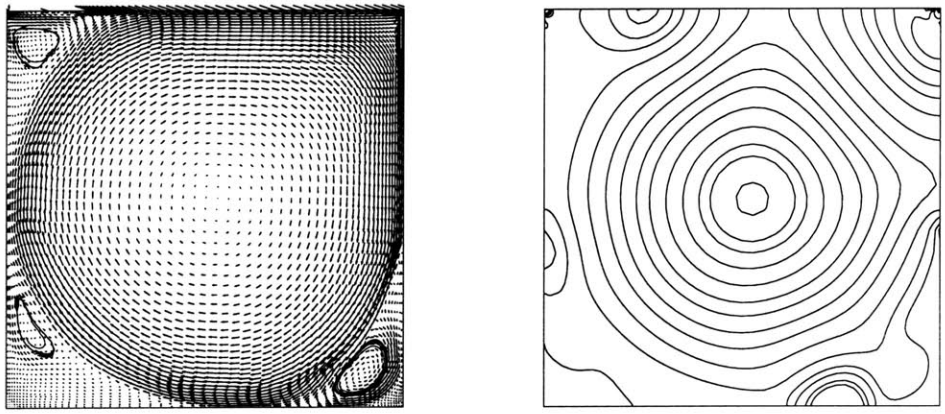

Figure 4-9: Vector velocity field (a) and pressure contours (b) for Reynolds number 1×10^6. FAFE scheme using 9/4-c elements.

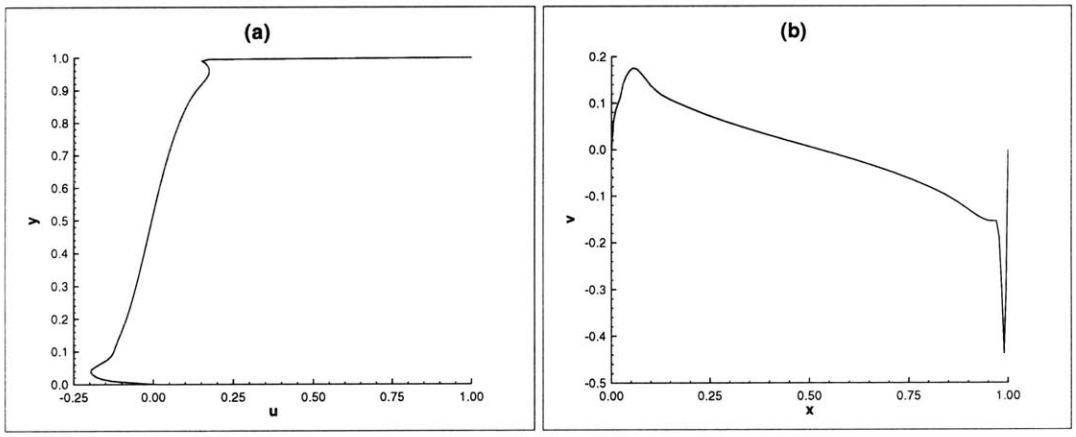

Figure 4-10: Normalized horizontal (a) and vertical (b) velocity profiles along the vertical and horizontal mid-sections of the cavity for Reynolds number 1×10^6. FAFE scheme using 9/4-c elements.

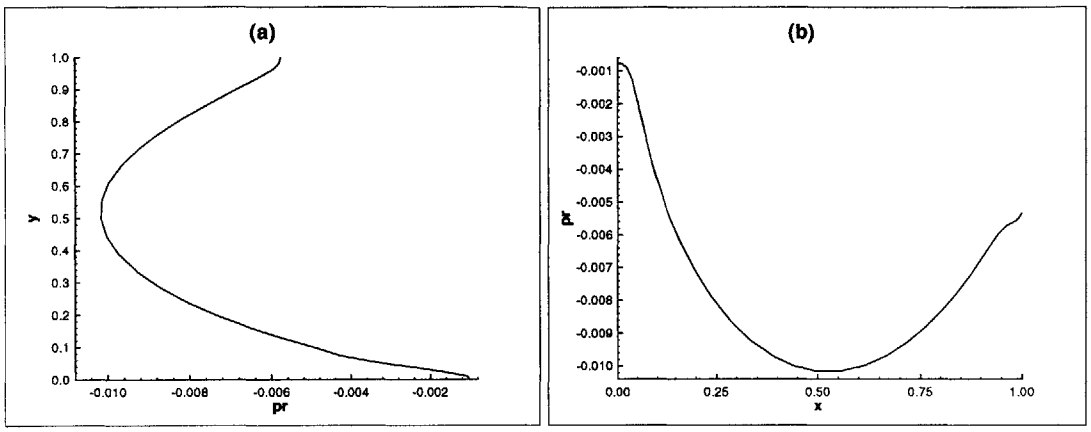

Figure 4-11: Normalized pressure profiles along the vertical (a) and horizontal (b) mid-sections of the cavity for Reynolds number 1×10^6. FAFE scheme using 9/4-c elements..

Table 4.1: Comparison of the formulations for the lid-driven cavity.

Reynolds Number	FAFE	LAPG	S-LAPG	FCBI	BG
1×10^2	√	√	√	√	√
1×10^3	√	√	√	√	√
1×10^4	√	√	√	√	√
1×10^5	√*	√*	—	—	—
1×10^6	√*	—	—	—	—

*Unsteady behavior.

4.4 180° channel flow

The incompressible fluid flow in a bend of outer diameter of 21 and an inner diameter of 19 is considered. A parabolic velocity profile is specified at the inlet, zero pseudo-tractions at the outlet, and zero velocities at the walls. A 15×150 element mesh is used for the computations, the mesh is non-uniform along the width and uniform along the length of the bend. Figure 4-12 shows the geometry and a partial view of the mesh.

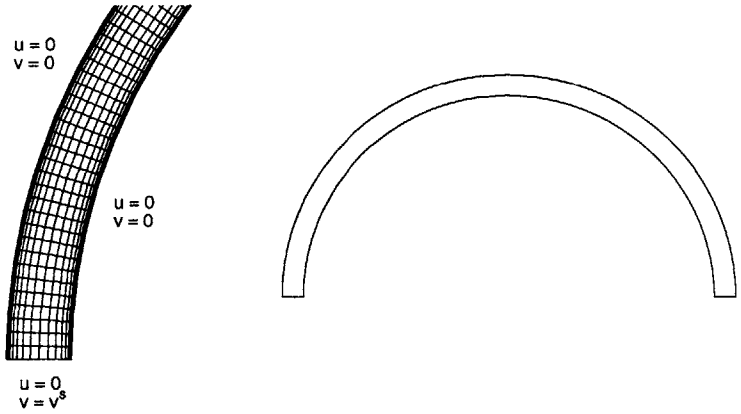

Figure 4-12: Geometry and partial view of the mesh for flow in a bend.

Of particular importance in the solution of this test problem is the pressure distribution along the length of the bend. We perform a steady state analysis for Reynolds number up to 1×10^6. The pressure distribution along the outer and inner walls obtained by the LAPG scheme using 9/4-c elements is compared with the Bubnov-Galerkin formulation in Figure 4-13. No solution was obtained with the Bubnov-Galerkin formulation for $\mathrm{Re} > 1 \times 10^3$.

Table 4.2 summarizes the performance of the four schemes in solving the 180° channel flow. The only scheme able to converge to a solution at Reynolds number 1×10^6 was the FAFE scheme. Both the LAPG and S-LAPG scheme could only go as high as $\mathrm{Re} = 1 \times 10^5$. The FCBI scheme showed its superiority over the classic Bubnov-Galerkin formulation by going above $\mathrm{Re} = 1 \times 10^3$.

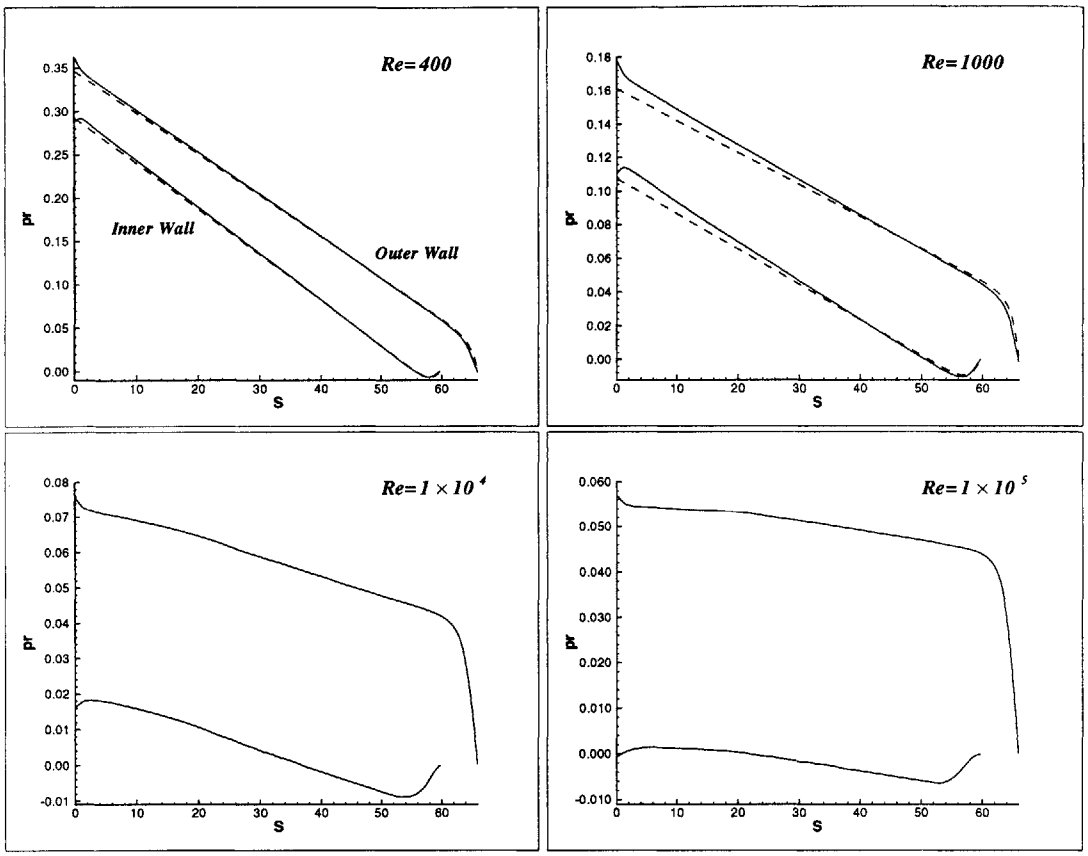

Figure 4-13: Normalized pressure profiles for 180° bend flow: — computed, - - - Bubnov-Galerkin. LAPG scheme using 9/4-c elements.

Table 4.2: Comparison of the formulations for the 180° channel flow.

Reynolds Number	FAFE	LAPG	S-LAPG	FCBI	BG
1×10^2	√	√	√	√	√
1×10^3	√	√	√	√	√
1×10^4	√	√	√	√	—
1×10^5	√	√	√	—	—
1×10^6	√	—	—	—	—

4.5 S-duct channel flow

This test problem is taken from Hendriana and Bathe [5]. The geometry, mesh, and boundary conditions are shown in Figure 4-14. The solution of this test problem displays complex physics in a simple geometry. The incompressible fluid enters the S-duct with a parabolic velocity profile, it is forced through a rough 90 degree turn, and then squeezed into another rough 90 degree turn. The flow configurations generated at the corners of the duct show vortex phenomena at many scales depending on the Reynolds number. The recirculating regions, rough 90 degree turns, and squeezing of the fluid make this an interesting and challenging problem.

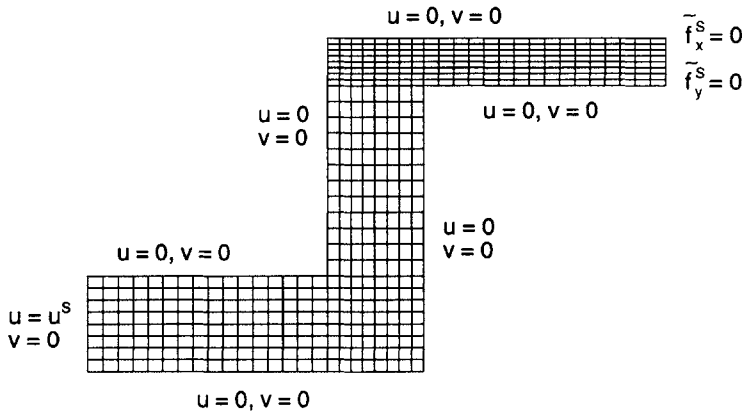

Figure 4-14: Geometry, mesh, and boundary conditions for flow in the S-duct.

Hendriana and Bathe [5] tested several upwind finite element schemes, including the SUPG [3] and GLS [4] schemes, for the high Reynolds number solution of this test problem. Only a simplified version of the SUPG scheme was able to go above Re = 1000. Here, all four schemes were able to go past Re = 1000. We emphasize, that the mesh shown in Figure 4-14 is the same one used in the computations of Hendriana and Bathe.

Figures 4-15 and 4-16 show plots of the velocity vector field and pressure contours for Reynolds number up to 1×10^6 computed with the FAFE scheme. These plots give a clear picture of the overall flow pattern and the effect of Reynolds number on

the structure of the recirculating eddies at the two lower and two upper corners of the duct. As the Reynolds number increases the strength of the recirculating eddies increases and the primary flow pattern changes significantly, especially at the second 90 degree turn where recirculation occurs near the exit of the duct. Even though the mesh in Figure 4-14 is not fine enough to resolve every detail of the flow, at $\mathrm{Re} = 1 \times 10^6$, a tertiary vortex is observed in the lower corner of the duct.

In an effort to obtain a more detailed flow solution we consider in Figure 4-17 a refined and graded version of the mesh shown in Figure 4-14. Again, we solve for the flow in the S-duct using the FAFE scheme. Vertical velocity and pressure profiles through section A-A of the S-duct are shown in Figures 4-18 and 4-19 for a range of Reynolds number up to 1×10^6. Horizontal velocity and pressure profiles through section B-B of the S-duct are shown in Figure 4-20 and 4-21 for a range of Reynolds number up to 1×10^6. The figures clearly show several flow separations at the two cross-sections as the Reynolds number is increased.

Figure 4-22 shows the vector velocity field at the exit of the S-duct for a range of Reynolds number. We notice from this figure that there is inflow at the exit of the S-duct when high Reynolds number flow is considered. The fact that the FAFE scheme did not become numerically unstable when inflow occurred is encouraging, i.e. the scheme is not overly sensitive to where we specify the outflow boundary condition or equivalently to where we choose to truncate the computational domain, see for example the remarks on outflow boundary conditions of Sani and Gresho [28].

The FAFE scheme was the only one able to go as high as $\mathrm{Re} = 1 \times 10^6$ without any changes to the mesh shown in Figure 4-14. The LAPG scheme went as high as $\mathrm{Re} = 1 \times 10^5$, however, the mesh had to be refined by a factor of two for computations with $\mathrm{Re} > 1 \times 10^3$. The S-LAPG was stable up to $\mathrm{Re} = 1 \times 10^4$ but mesh grading was necessary for $\mathrm{Re} > 1 \times 10^3$. The FCBI scheme could only go up to $\mathrm{Re} = 1 \times 10^3$, mesh refinement, grading, and/or enlarging the exit of the S-duct did not help. Table 4.3 summarizes the experiences with the discretization schemes applied to the mesh in Figure 4-14.

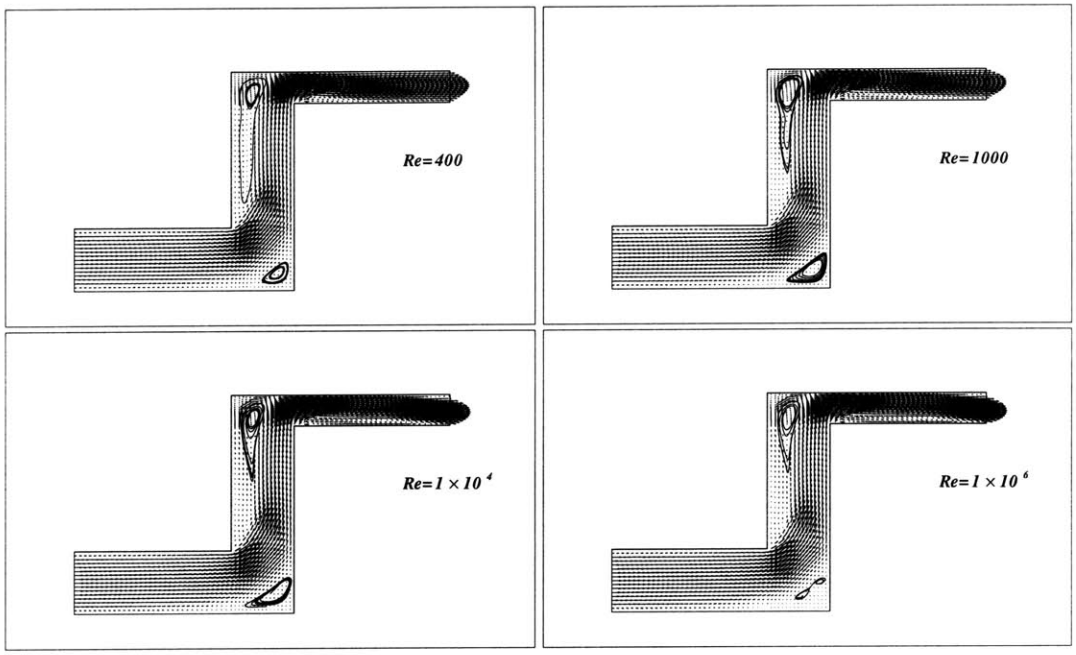

Figure 4-15: Vector velocity field for Reynolds number 400, 1000, 1×10^4, and 1×10^6. FAFE scheme using 9/4-c elements.

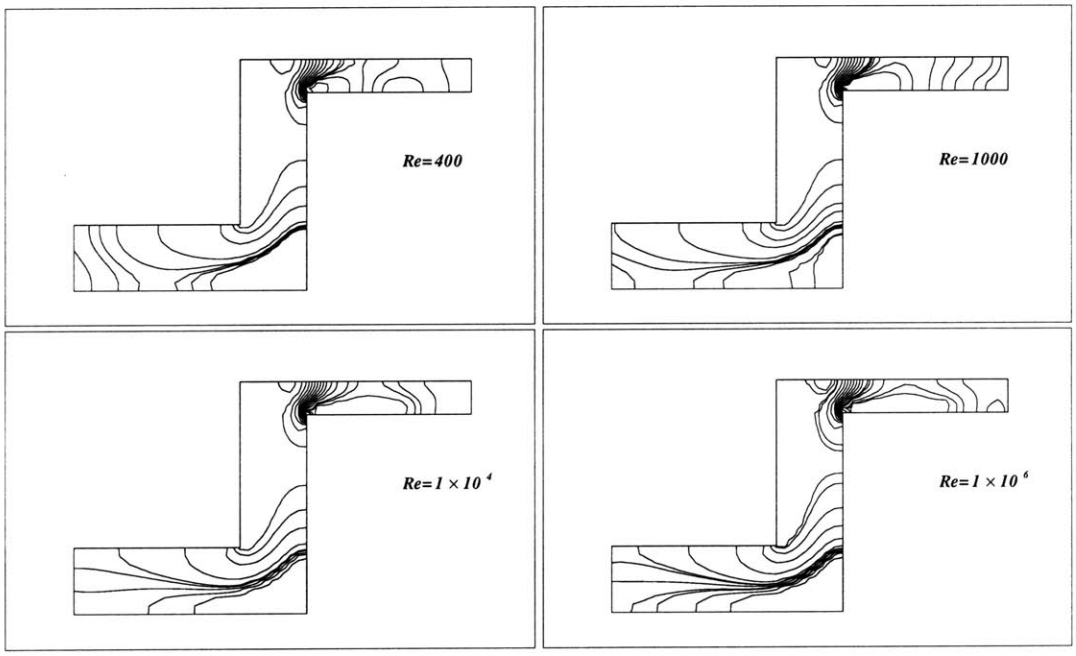

Figure 4-16: Pressure contours for Reynolds number 400, 1000, 1×10^4, and 1×10^6. FAFE scheme using 9/4-c elements.

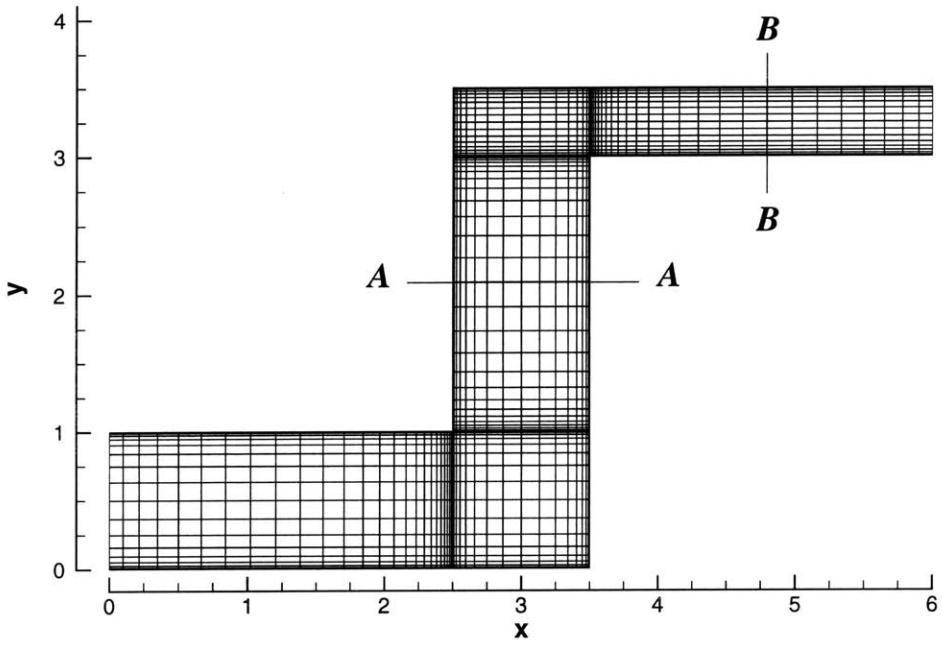

Figure 4-17: Refined and graded mesh for flow in the S-duct.

Table 4.3: Comparison of the formulations for the S-duct channel flow.

Reynolds Number	FAFE	LAPG	S-LAPG	FCBI	BG
1×10^2	√	√	√	√	√
1×10^3	√	√	√	√	—
1×10^4	√	√ *	√ †	—	—
1×10^5	√	√ *	—	—	—
1×10^6	√	—	—	—	—

*Refining the mesh by a factor of two.
†Refining the mesh by a factor of two and grading.

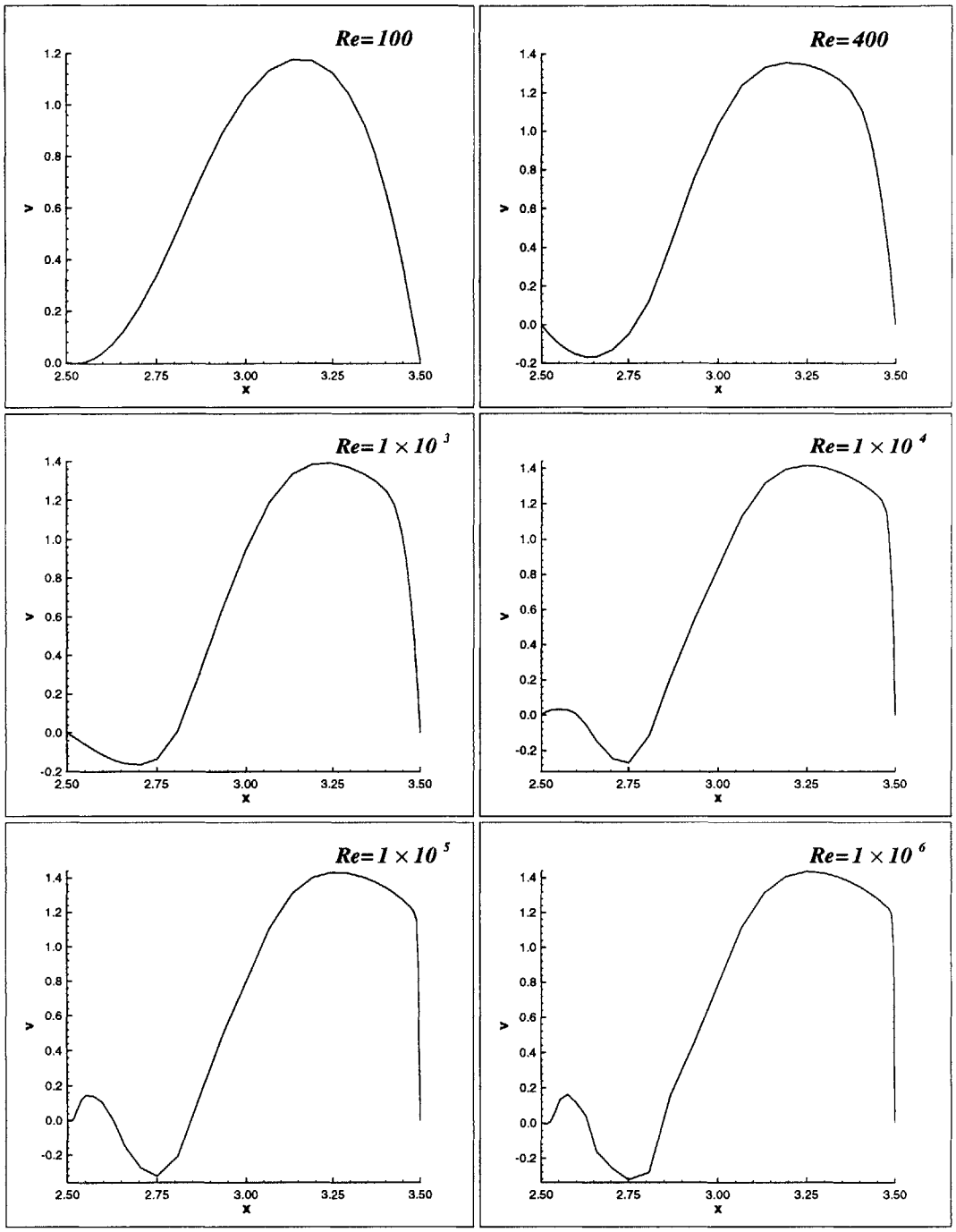

Figure 4-18: Normalized vertical velocity profiles along section A-A of the S-duct. FAFE scheme using 9/4-c elements.

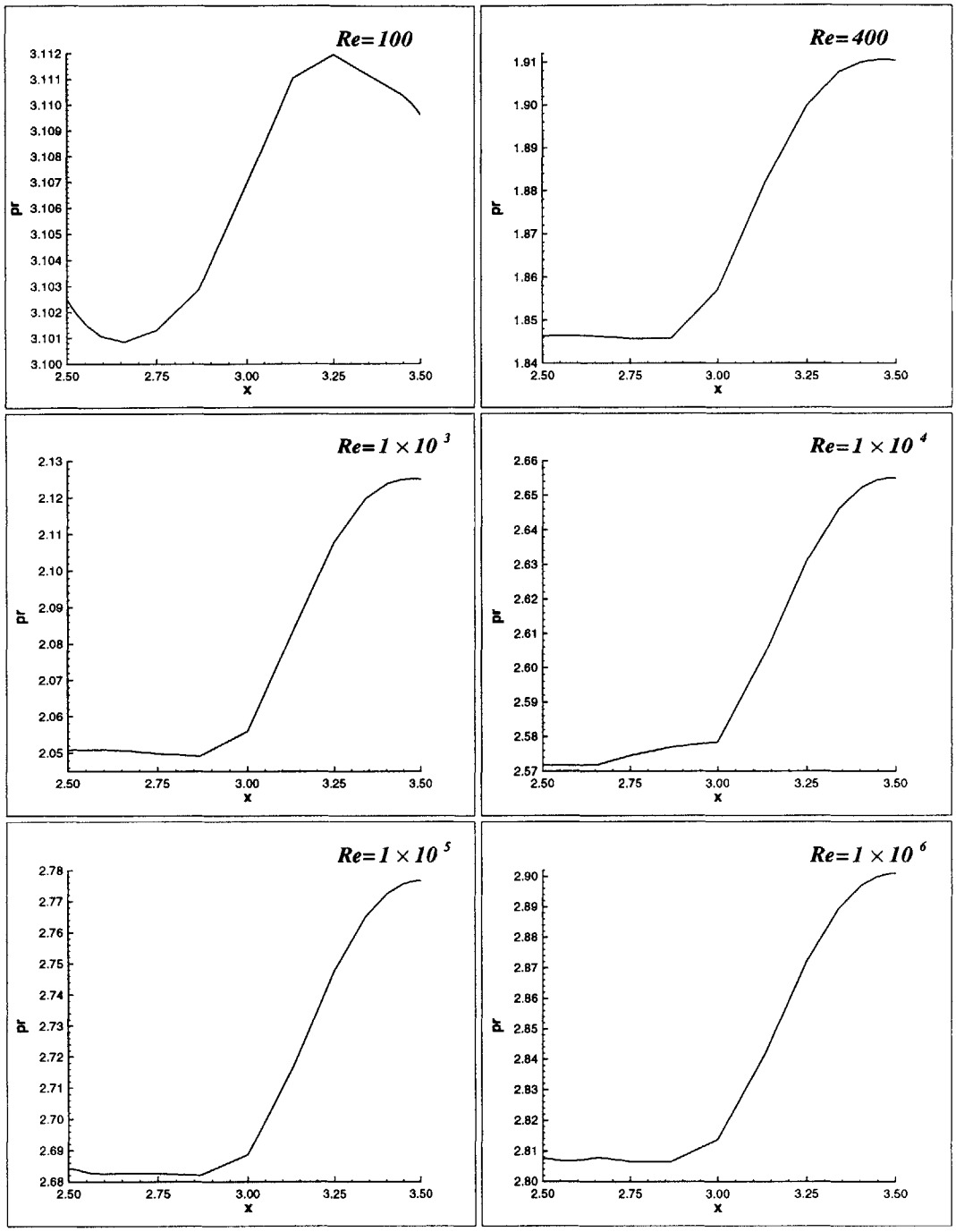

Figure 4-19: Normalized pressure profiles along section A-A of the S-duct. FAFE scheme using 9/4-c elements.

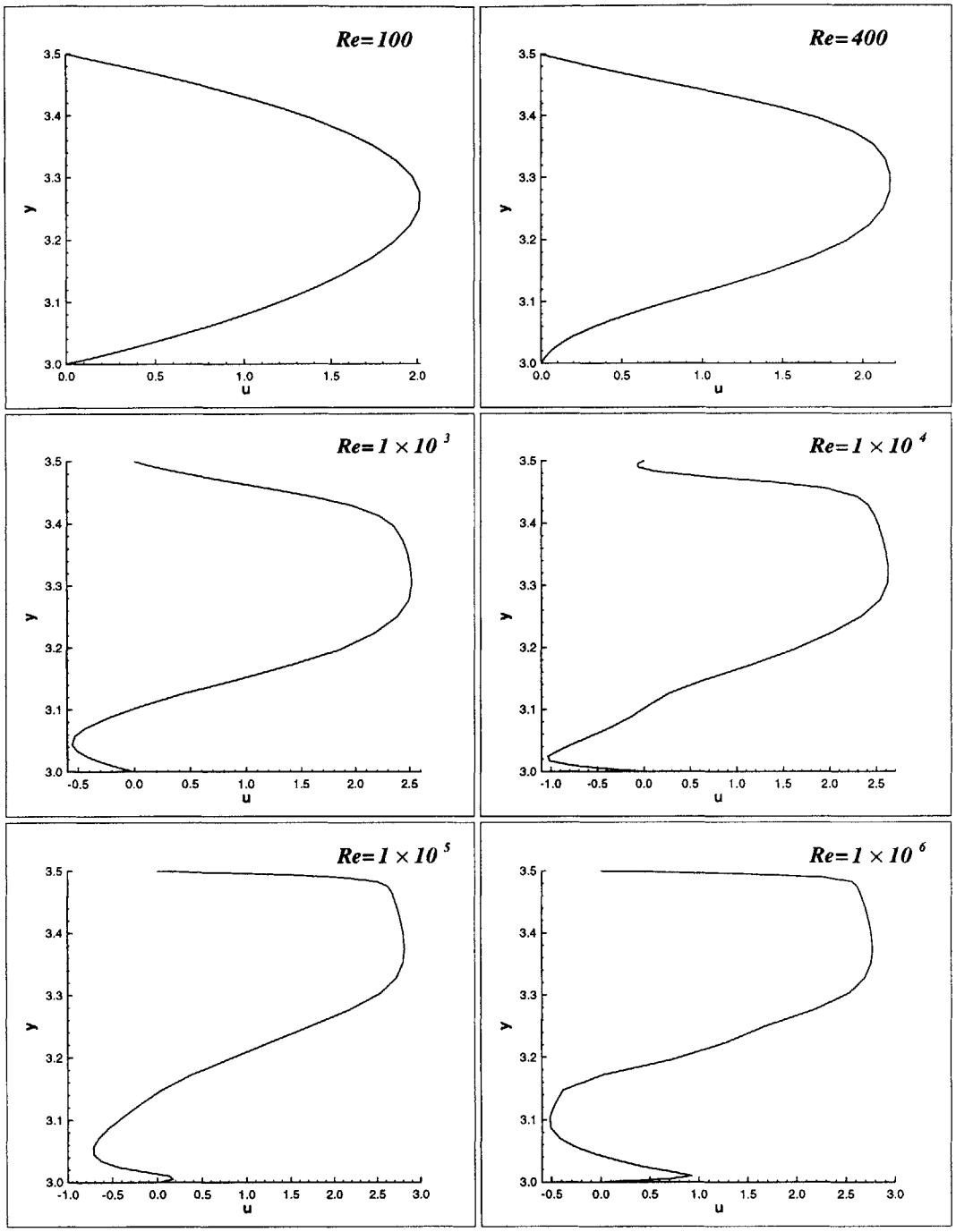

Figure 4-20: Normalized horizontal velocity profiles along section B-B of the S-duct. FAFE scheme using 9/4-c elements.

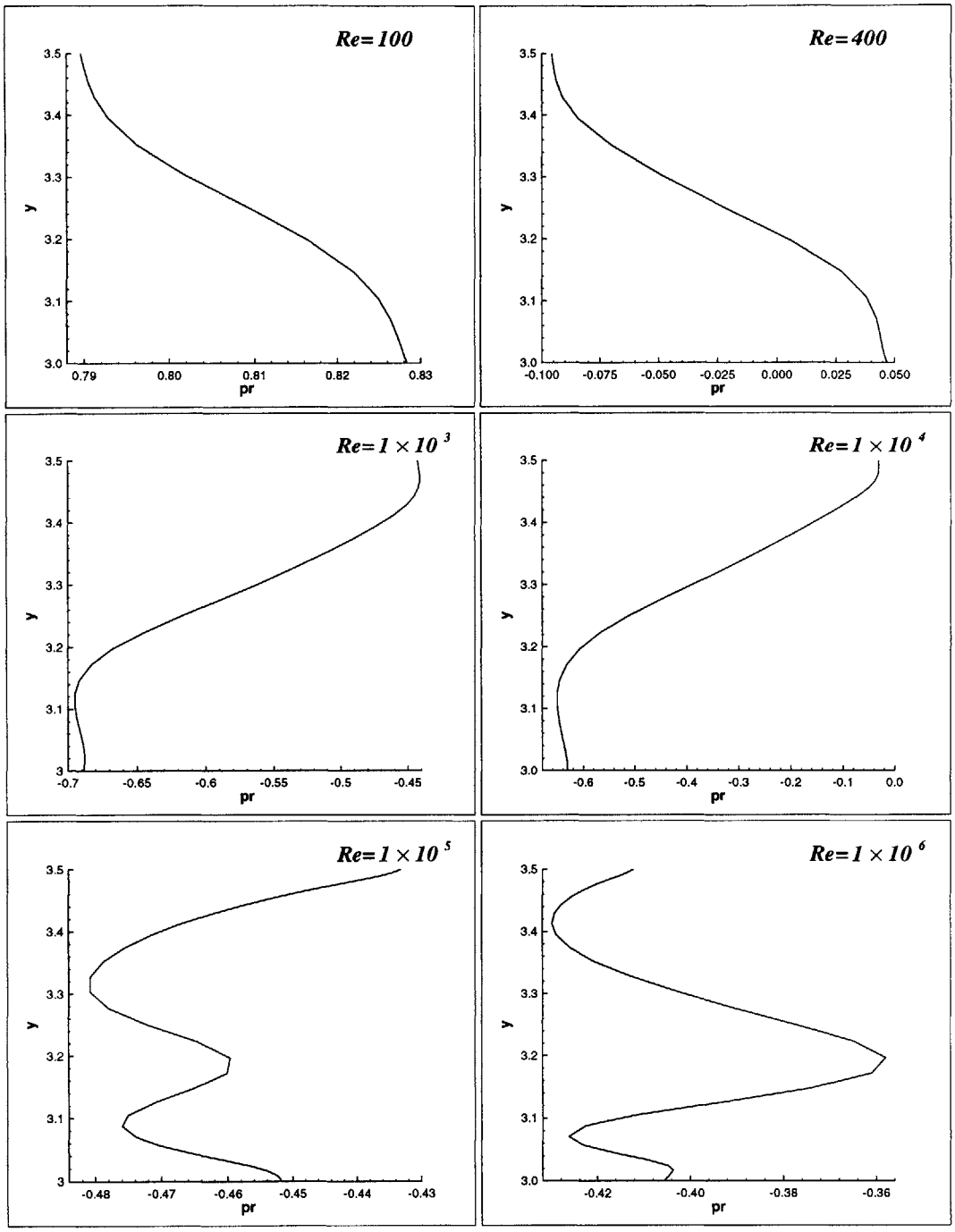

Figure 4-21: Normalized pressure profiles along section B-B of the S-duct. FAFE scheme using 9/4-c elements.

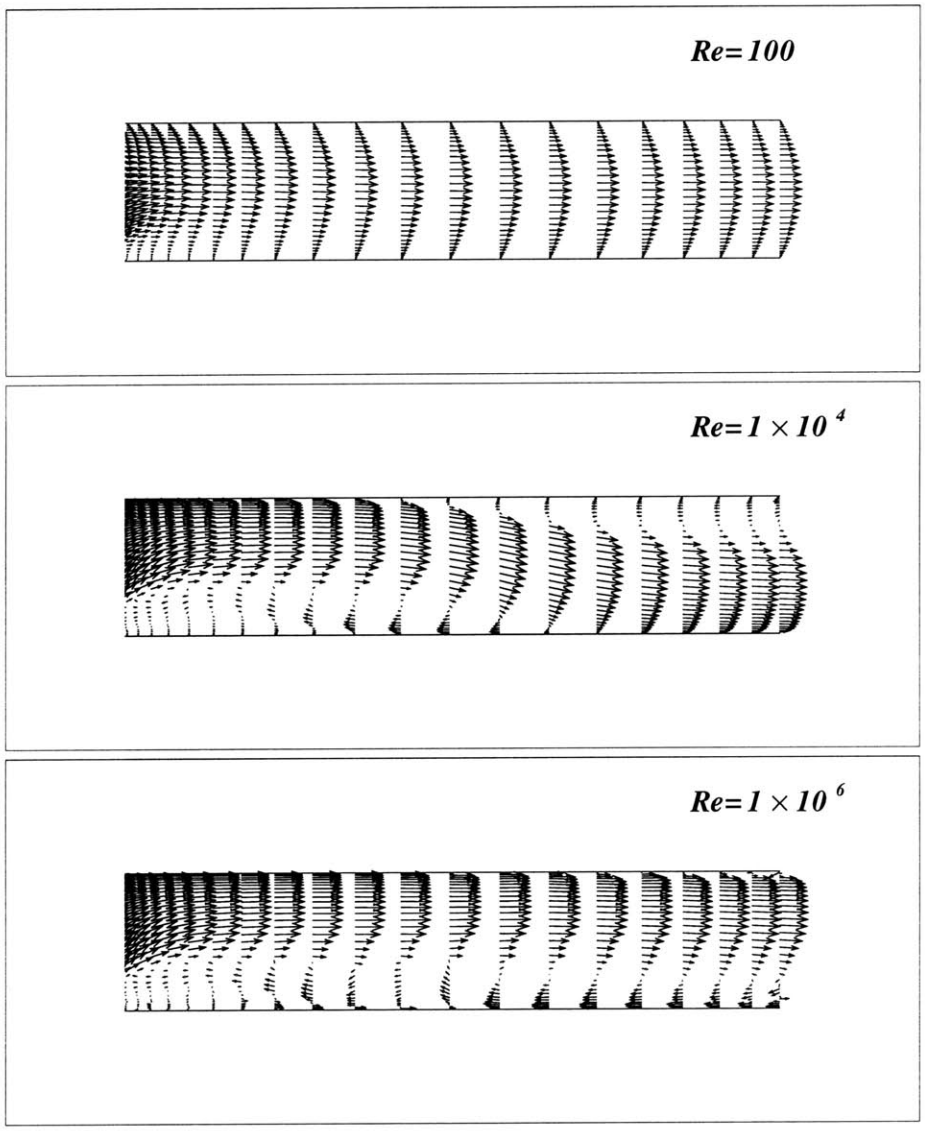

Figure 4-22: Velocity vector field at the exit of the S-duct for a range of Reynolds number. FAFE scheme using 9/4-c elements.

4.6 Transient flow past a circular cylinder

To test the non-stationary formulation we consider transient flow past a circular cylinder. The computational domain is a rectangle, $-5 \leq x \leq 20$, $-5 \leq y \leq 5$, with a cylinder of unit diameter placed at $(x, y) = (0, 0)$. The mesh consists of 1200 elements and is shown in Figure 4-23. The boundary conditions for the problem include an imposed value of unity for the x velocity component at the inflow and at the top and bottom boundaries, at these boundaries the y velocity component was specified to be zero. Zero pseudo-tractions are specified at the outflow boundary and zero velocities around the cylinder. We consider flow at a freestream Reynolds number of 100 and compare our results with the benchmark solution of Engelman and Jamnia [29]. The transient time integration is performed using an implicit predictor-corrector scheme. The corrector step uses the second order accurate and non-dissipative trapezoidal rule while the predictor step is a second order Adams Bashford scheme. The scheme allows for a variable time increment at each time step, the increment being determined by controlling the local time truncation error (LTTE) at each time step. Complete details of the time integration scheme can be found in [30].

For this computation the LTTE between time steps was allowed to be no greater than 5×10^{-4}. At each time step the non-linear system of algebraic equations was solved using a Newton-Raphson solver. Because a predictor-corrector scheme is being used and the LTTE is small, the predictor is sufficiently accurate that at most three iterations of the non-linear solver were required to obtain convergence at each time step. A convergence tolerance on the normalized norm of the residuals in velocities $\left(\|\Delta \mathbf{u}^h\| / \|\mathbf{u}^h\| \right)$ of 1×10^{-5} was used to terminate the non-linear iteration scheme.

The shedding period computed using the S-LAPG scheme with 9/4-c elements was $T = 5.82$, which compares well with the benchmark value of $T = 5.80$. All other formulations gave results within 2% of this value. The Strouhal number follows directly as $\mathrm{St} = 0.172$, which is defined as $\mathrm{St} = D/UT$ where D is the diameter of the cylinder and U is the characteristic velocity. Figure 4-24 shows the instantaneous velocity and pressure contours after the periodic regime is reached.

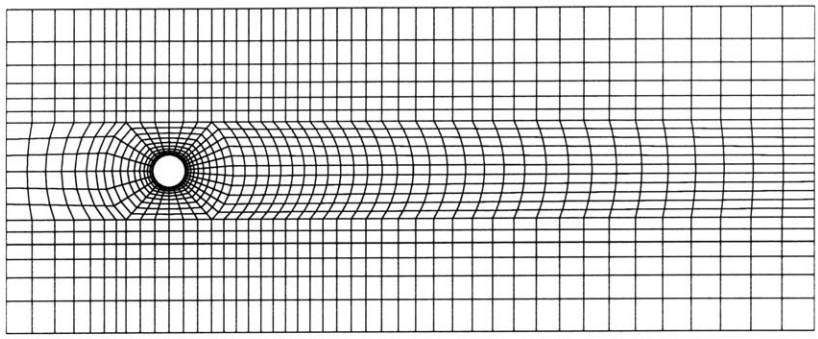

Figure 4-23: Geometry and mesh for flow past a circular cylinder.

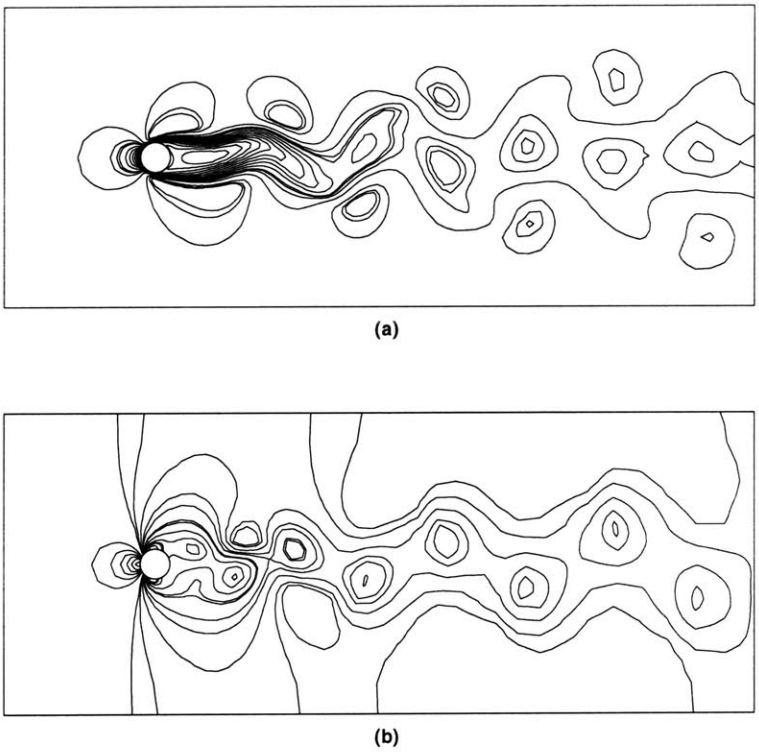

Figure 4-24: Contour plot of the x velocity component (a) and pressure field (b). S-LAPG scheme using 9/4-c elements.

Chapter 5

Conclusions

In this work we have presented four finite element formulations for the solution of two-dimensional high Reynolds number incompressible fluid flows. The formulations use high-order elements – the 9/3 or 9/4-c elements – which are optimal in enforcing the incompressibility constraint. The essential idea in developing the formulations was to incorporate local analytic behavior in the numerical solution of the Navier-Stokes equations. This was achieved in different manners for the four formulations.

In the Finite Analytic/Finite Element (FAFE) formulation we directly use the local analytic solution of the advection-diffusion equation to discretize the momentum equations and enforce the incompressibility constraint in a weighted residual manner. Evaluation of the scheme in the solution of several test problems showed that the scheme is superior to any of the other schemes developed here, provided that the mesh has a high degree of orthogonality. This condition is a direct consequence of the way in which the discretization procedure was derived, i.e. the separation of variables procedure is only valid in an orthogonal coordinate system. The scheme is fully effective when the mesh is orthogonal and deteriorates as orthogonality is lost. Note that the mesh could be curvilinear but at the same time orthogonal. When the orthogonality condition was met the scheme consistently solved problems with Reynolds number as high as 1×10^6 using fairly coarse meshes.

In the Local Analytic/Petrov-Galerkin (LAPG) formulation we endowed the test function with properties from the local analytic solution. This allowed the test func-

tion to respond to the velocity field so as to give more weight to upstream nodes, the amount of weight and the upstream direction being completely determined by the local analytic solution. However, some difficulties were encountered in differentiating the test functions and subsequently integrating expressions involving the test functions. To alleviate this problem a simplified version of the LAPG (S-LAPG) was developed. In this formulation the test functions were taken to be the sum of two functions: the enhanced test functions and biquadratic test functions. In developing the variational form of the momentum equations, the differentiation was absorbed by the biquadratic functions but the effect of the enhanced test functions was retained without the need of differentiating. Both formulations performed fairly well in the solution of the test problems at high Reynolds number, furthermore, the formulations had no problems in dealing with distorted meshes.

The Exponential/Flow-condition-based interpolation (FCBI) scheme arose from efforts to simplify the process by which the test functions are endowed with local analytic properties. In this scheme the test functions are simply taken to be the tensor product of one-dimensional linear-exponential functions along the edge- and mid-lines of the element. The evaluation and differentiation of the test functions is straightforward and can be done efficiently as products of the one-dimensional test functions. The procedure is simple and a natural extension of a discretization scheme known to be optimal for low Reynolds number fluid flows. The FCBI scheme did not perform as well as the other schemes, however it showed a clear advantage over the classic Bubnov-Galerkin formulation and is the strongest candidate for future mathematical analysis.

We remark that the evaluation of the schemes was only based on the solution of the test problems presented in Chapter 4. This work can be classed as the numerical experimentation phase and before an effective scheme can be claimed a rigorous mathematical study of the schemes is required. The schemes presented in this work have a sound mathematical basis and performed well in the numerical experimentation phase. No mathematical or numerical studies of convergence and accuracy were performed and is clearly a necessary next step before any of the schemes can be used

confidently.

Recommendations for future research are:

- The development of efficient techniques with a strong mathematical basis to endow the test functions with local analytic properties.

- The development of specialized quadrature rules for the efficient and accurate evaluation of expressions involving the derivatives of the enhanced test functions.

- Further research on the implementation of the schemes for the case of geometrically distorted elements. The procedures suggested in Chapter 3 and Appendix B, for some flow conditions, lack physical meaning.

Appendix A

The advection-diffusion equation

A.1 Solution by separation of variables

In this appendix we give details of the procedures by which an analytic solution to the two-dimensional advection-diffusion equation can be obtained by the method of separation of variables. Consider the two-dimensional advection-diffusion equation for a generic transported scalar $\phi(x, y)$, in the rectangular domain shown in Figure A-1,

$$\frac{\partial^2 \phi}{\partial x^2} + \frac{\partial^2 \phi}{\partial y^2} = 2A\frac{\partial \phi}{\partial x} + 2B\frac{\partial \phi}{\partial y} + S \tag{A.1}$$

where A, B, and S are known constants. In Figure A-1 we identify the nodes using compass notation, i.e. north, south, east, west, northwest, etc., this will be an aid in the presentation of the solution procedures. Note that in this appendix $\phi(x, y)$ is used to denote a generic transported scalar, not to be confused with $\{\phi_n(\mathbf{x})\}$ which are reserved to denote the enhanced test functions in the main body of the thesis.

We construct appropriate boundary data by studying the natural solution for equation (A.1):

$$\phi(x, y) = C_0\, e^{2(Ax+By)} + C_1\,(Ay - Bx) + C_2 - \frac{S}{2\,(A^2 + B^2)}\,(Ax + By) \tag{A.2}$$

The first three terms in the solution satisfy the homogeneous part of (A.1), the last

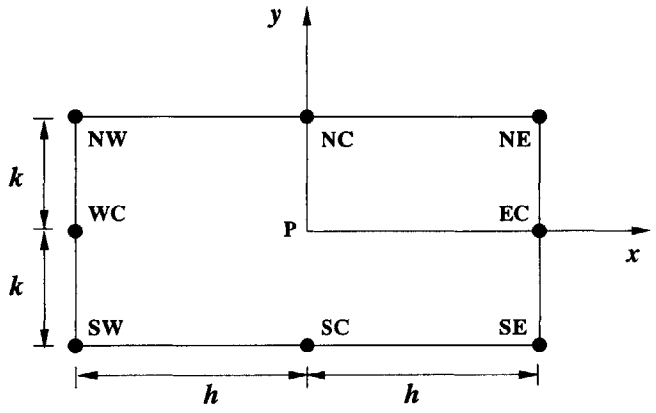

Figure A-1: Rectangular element with 8 boundary nodes.

term is the particular solution of (A.1). Next we define $\tilde{\phi}$ as

$$\tilde{\phi} = \phi + \frac{S_P}{2\left(A^2 + B^2\right)}\left(Ax + By\right) \tag{A.3}$$

Substituting for ϕ from equation (A.3) into equation (A.1), we see that $\tilde{\phi}$ satisfies the homogeneous equation

$$\left(\frac{\partial^2 \tilde{\phi}}{\partial x^2} + \frac{\partial^2 \tilde{\phi}}{\partial y^2}\right) = 2A\frac{\partial \tilde{\phi}}{\partial x} + 2B\frac{\partial \tilde{\phi}}{\partial y} \tag{A.4}$$

The natural solution (A.2) suggests that an exponential and linear function in terms of three nodal values on each boundary may be employed to obtain the approximated boundary condition for the element considered. For example the north boundary condition where y is fixed can be approximated by

$$\tilde{\phi}_N(x) = a_N\left(e^{2Ax} - 1\right) + b_N x + c_N \tag{A.5}$$

where

$$a_N = \frac{\tilde{\phi}_{NE} + \tilde{\phi}_{NW} - 2\tilde{\phi}_{NC}}{4\sinh^2 Ah}$$

$$b_N = \frac{\tilde{\phi}_{NE} - \tilde{\phi}_{NW} - \coth Ah\left(\tilde{\phi}_{NE} + \tilde{\phi}_{NW} - 2\tilde{\phi}_{NC}\right)}{2h} \tag{A.6}$$

$$c_N = \tilde{\phi}_{NC}$$

The boundary conditions for south, east, and west sides can be similarly approximated by exponential and linear boundary functions as follows:

$$\tilde{\phi}_S(x) = a_S\left(e^{2Ax} - 1\right) + b_S x + c_S$$

$$\tilde{\phi}_E(y) = a_E\left(e^{2By} - 1\right) + b_E y + c_E$$

$$\tilde{\phi}_W(y) = a_W\left(e^{2By} - 1\right) + b_W y + c_W$$

where the coefficients a_S, b_S, etc. can be expressed in terms of the nodal values along each boundary in a way similar to that for a_N, b_N, and c_N in equation (A.6). Next we introduce a change of variable

$$\tilde{\phi} = w\, e^{Ax+By} \tag{A.7}$$

and equation (A.4) takes the following form:

$$w_{xx} + w_{yy} = \left(A^2 + B^2\right) w \tag{A.8}$$

subject to the "transformed" boundary conditions

$$w_N(x) = e^{-Bk}\left[a_N e^{Ax} + b_N x e^{-Ax} + (c_N - a_N)\, e^{-Ax}\right] \tag{A.9}$$

$$w_S(x) = e^{Bk}\left[a_S e^{Ax} + b_S x e^{-Ax} + (c_S - a_S)\, e^{-Ax}\right] \tag{A.10}$$

$$w_E(y) = e^{-Ah}\left[a_E e^{By} + b_E y e^{-By} + (c_E - a_E)\, e^{-By}\right] \tag{A.11}$$

$$w_W(y) = e^{Ah}\left[a_W e^{By} + b_W y e^{-By} + (c_W - a_W)\, e^{-By}\right] \tag{A.12}$$

Equation (A.8) can be solved by the method of separation of variables, by further dividing it into four simpler problems with each of them containing one non-homogeneous and three homogeneous boundary conditions. The solution would then be a superposition of the solutions of the four simpler problems:

$$w(x,y) = w^N(x,y) + w^S(x,y) + w^E(x,y) + w^W(x,y) \tag{A.13}$$

Consider the first of these four problems, which can be stated as:

$$w^N_{xx} + w^N_{yy} = \left(A^2 + B^2\right) w^N \tag{A.14}$$

subject to the following boundary conditions

$$w^N(x,k) = w_N(x)$$

$$w^N(x,-k) = w^N(h,y) = w^N(-h,y) = 0$$

We proceed by the method of separation of variables and let

$$w^N(x,y) = g(x)\varphi(y) \tag{A.15}$$

then equation (A.14) becomes

$$\varphi\frac{d^2g}{dx^2} + g\frac{d^2\varphi}{dy^2} = \left(A^2 + B^2\right) g\varphi \tag{A.16}$$

$$\frac{1}{g}\frac{d^2g}{dx^2} = \left(A^2 + B^2\right) - \frac{1}{\varphi}\frac{d^2\varphi}{dy^2} = -\lambda \tag{A.17}$$

Since we want $g(x)$ to be zero at $+h$ and $-h$, $g(x)$ is the solution of the homogeneous boundary value problem. So we have

$$\frac{d^2g}{dx^2} = -\lambda g, \qquad g(-h) = g(+h) = 0 \tag{A.18}$$

and

$$\frac{d^2\varphi}{dy^2} = \varphi\left(A^2 + B^2 + \lambda\right), \qquad \varphi(-k) = 0 \tag{A.19}$$

The x dependent problem is the homogeneous boundary value problem and will be used to determine the eigenvalues λ. Equation (A.18) has a general solution of the form:

$$g(x) = c_1 \cos\sqrt{\lambda}(x+h) + c_2 sin\sqrt{\lambda}(x+h) \tag{A.20}$$

Applying the homogeneous boundary conditions to determine the constants, we have that:

$$g(x=-h) = c_1\cos(0) = 0, \quad \Rightarrow \quad c_1 = 0 \tag{A.21}$$

$$g(x=+h) = c_2 \sin\sqrt{\lambda}2h = 0, \quad \Rightarrow \quad \sqrt{\lambda} = \frac{n\pi}{2h}, \quad n = 1,2,3,\ldots \tag{A.22}$$

hence

$$g_n(x) = sin\frac{n\pi(x+h)}{2h}, \quad n = 1,2,3,\ldots \tag{A.23}$$

Next we solve equation (A.19),

$$\frac{d^2\varphi}{dy^2} = \varphi\left[A^2 + B^2 + \left(\frac{n\pi}{2h}\right)^2\right] \tag{A.24}$$

whose general solution is of the form

$$\begin{aligned}\varphi(y) = a_1 \cosh\sqrt{A^2 + B^2 + \left(\frac{n\pi}{2h}\right)^2}(y+k) \\ + a_2 \sinh\sqrt{A^2 + B^2 + \left(\frac{n\pi}{2h}\right)^2}(y+k)\end{aligned} \tag{A.25}$$

Applying the homogeneous boundary condition to determine one of the constants, we have that:

$$\varphi(y=-k) = a_1 = 0 \tag{A.26}$$

hence

$$\varphi_n(y) = a_2 \sinh \sqrt{A^2 + B^2 + \left(\frac{n\pi}{2h}\right)^2}(y+k), \quad n = 1, 2, 3, \ldots \tag{A.27}$$

Thus the solution to (A.14) has the following form:

$$w^N(x,y) = \sum_{n=1}^{\infty} A_n sin\frac{n\pi}{2h}(x+h) \sinh \sqrt{A^2 + B^2 + \left(\frac{n\pi}{2h}\right)^2}(y+k) \tag{A.28}$$

where the coefficients A_n are yet to be determined.

Evaluating (A.28) at $y = +k$ will determine the coefficients A_n:

$$w^N(x,k) = w_N(x) = \sum_{n=1}^{\infty} A_n sin\frac{n\pi}{2h}(x+h) \sinh \sqrt{A^2 + B^2 + \left(\frac{n\pi}{2h}\right)^2}(2k) \tag{A.29}$$

then

$$A_n \sinh \sqrt{A^2 + B^2 + \left(\frac{n\pi}{2h}\right)^2}(2k) = \frac{2}{2h}\int_{-h}^{h} w_N(x) sin\frac{n\pi}{2h}(x+h)dx \tag{A.30}$$

or

$$A_n = \frac{1}{h \sinh 2\mu_n k}\int_{-h}^{h} w_N(x) sin\frac{n\pi}{2h}(x+h)dx \tag{A.31}$$

where

$$\mu_n = \sqrt{A^2 + B^2 + \left(\frac{n\pi}{2h}\right)^2} \tag{A.32}$$

Evaluating A_n is not a difficult task, since the integrals can be evaluated analytically. Inserting for w_N from equation (A.9) into equation (A.31) yields the following expression for A_n:

$$A_n = \frac{e^{-Bk}}{\sinh 2\mu_n k}\left[a_N e_{0n} + b_N h e_{1n} + (c_N - a_N)\, e_{2n}\right] \tag{A.33}$$

where

$$e_{0n} = \frac{1}{h}\int_{-h}^{h} e^{Ax} \sin\frac{n\pi}{2h}(x+h)dx \tag{A.34}$$

$$e_{1n} = \frac{1}{h^2}\int_{-h}^{h} xe^{-Ax}\sin\frac{n\pi}{2h}(x+h)dx \tag{A.35}$$

$$e_{2n} = \frac{1}{h}\int_{-h}^{h} e^{-Ax}\sin\frac{n\pi}{2h}(x+h)dx \tag{A.36}$$

or

$$e_{0n} = \frac{\lambda_n h}{(Ah)^2 + (\lambda_n h)^2}\left[e^{-Ah} - (-1)^n e^{Ah}\right] \tag{A.37}$$

$$\begin{aligned} e_{1n} = {} & \frac{2(Ah)(\lambda_n h)}{\left[(Ah)^2 + (\lambda_n h)^2\right]^2}\left[e^{Ah} - (-1)^n e^{-Ah}\right] \\ & - \frac{\lambda_n h}{(Ah)^2 + (\lambda_n h)^2}\left[e^{Ah} + (-1)^n e^{-Ah}\right] \end{aligned} \tag{A.38}$$

$$e_{2n} = \frac{\lambda_n h}{(Ah)^2 + (\lambda_n h)^2}\left[e^{Ah} - (-1)^n e^{-Ah}\right] \tag{A.39}$$

where

$$\lambda_n = \frac{n\pi}{2h} \tag{A.40}$$

and the coefficients a_N, b_N, and c_N are given in equation (A.6).

This concludes the first of the four problems. Similar analysis is needed for each of the four problems. The pseudo-solution, $w(x,y)$ from equation (A.13), has the following form:

$$\begin{aligned} w(x,y) = {} & \sum_{n=1}^{\infty} C_n^1 \sinh\left[\mu_n^h(y+k)\right]\sin\left[\lambda_n^h(x+h)\right] \\ & + \sum_{n=1}^{\infty} C_n^2 \sinh\left[\mu_n^h(y-k)\right]\sin\left[\lambda_n^h(x+h)\right] \\ & + \sum_{n=1}^{\infty} C_n^3 \sinh\left[\mu_n^k(x+h)\right]\sin\left[\lambda_n^k(y+k)\right] \\ & + \sum_{n=1}^{\infty} C_n^4 \sinh\left[\mu_n^k(x-h)\right]\sin\left[\lambda_n^k(y+k)\right] \end{aligned} \tag{A.41}$$

with

$$C_n^1 = \frac{e^{-Bk}}{\sinh(2\mu_n^h k)}\left[a_N e_{0n} + b_N h\, e_{1n} + (c_N - a_N)\, e_{2n}\right] \tag{A.42}$$

$$C_n^2 = \frac{e^{Bk}}{\sinh(-2\mu_n^h k)}\left[a_S e_{0n} + b_S h\, e_{1n} + (c_S - a_S)\, e_{2n}\right] \tag{A.43}$$

$$C_n^3 = \frac{e^{-Ah}}{\sinh(2\mu_n^k h)}\left[a_E e_{3n} + b_E k\, e_{4n} + (c_E - a_E)\, e_{5n}\right] \tag{A.44}$$

$$C_n^4 = \frac{e^{Ah}}{\sinh(-2\mu_n^k h)}\left[a_W e_{3n} + b_W k\, e_{4n} + (c_W - a_W)\, e_{5n}\right] \tag{A.45}$$

and the $\tilde{\phi}(x,y)$ can be immediately obtained from equation (A.7).

Next we develop expressions for $\tilde{\phi}(0,0) = \tilde{\phi}^0$, i.e. the local analytic solution to equation (A.4) evaluated at point P, $(x,y) = (0,0)$, in Figure A-1. At point P, the sine functions in equation (A.41) can be easily decomposed as follows:

$$\sin\left(\frac{n\pi}{2}\right) = \begin{cases} 0 & \text{if } n = 2m, \\ -(-1)^m & \text{if } n = 2m-1. \end{cases} \tag{A.46}$$

Since we are interested only in the non-zero contributions, equation (A.41) can can be simplified considerably. Each of its four contributions can now be written as:

$$w^N = e^{-Bk}\left[\left(\frac{E_1}{2} - E_2 Ah\coth Ah\right)\left(e^{-Ah}\phi_{NE} + e^{Ah}\phi_{NW}\right) + \left(2Ah\coth Ah\cosh AhE_2\right)\phi_{NC}\right] \tag{A.47}$$

$$w^S = e^{Bk}\left[\left(\frac{E_1}{2} - E_2 Ah\coth Ah\right)\left(e^{-Ah}\phi_{SE} + e^{Ah}\phi_{SW}\right) + \left(2Ah\coth Ah\cosh AhE_2\right)\phi_{SC}\right] \tag{A.48}$$

$$w^E = e^{-Ah}\left[\left(\frac{E_1'}{2} - E_2' Bk\coth Bk\right)\left(e^{-Bk}\phi_{NE} + e^{Bk}\phi_{SE}\right) + \left(2Bk\coth Bk\cosh BkE_2'\right)\phi_{EC}\right] \tag{A.49}$$

$$w^W = e^{Ah}\left[\left(\frac{E_1^{'}}{2} - E_2^{'}Bk\coth Bk\right)\left(e^{-Bk}\phi_{NW} + e^{Bk}\phi_{SW}\right)\right.$$
$$\left. + \left(2Bk\coth Bk\cosh BkE_2^{'}\right)\phi_{WC}\right] \tag{A.50}$$

where the following definitions apply:

$$E_i = \sum_{m=1}^{\infty} \frac{-(-1)^m\left(\lambda_m^h h\right)}{\left[(Ah)^2 + (\lambda_m^h h)^2\right]^i}\left(\frac{1}{\cosh\left(\mu_m^h k\right)}\right) \tag{A.51}$$

with

$$\lambda_m^h = \frac{(2m-1)\pi}{2h}, \qquad \mu_m^h = \sqrt{A^2 + B^2 + \left(\lambda_m^h\right)^2}$$

and similarly

$$E_i^{'} = \sum_{m=1}^{\infty} \frac{-(-1)^m\left(\lambda_m^k k\right)}{\left[(Bk)^2 + (\lambda_m^k k)^2\right]^i}\left(\frac{1}{\cosh\left(\mu_m^k h\right)}\right) \tag{A.52}$$

with

$$\lambda_m^k = \frac{(2m-1)\pi}{2k}, \qquad \mu_m^k = \sqrt{A^2 + B^2 + \left(\lambda_m^k\right)^2}$$

Grouping like terms and realizing that $\tilde{\phi}(0,0) = \tilde{\phi}^0 = w(0,0)$, we can write:

$$\tilde{\phi}^0 = \alpha_{SW}^0\,\tilde{\phi}_{SW} + \alpha_{SE}^0\,\tilde{\phi}_{SE} + \alpha_{NE}^0\,\tilde{\phi}_{NE} + \alpha_{NW}^0\,\tilde{\phi}_{NW}$$
$$+ \alpha_{SC}^0\,\tilde{\phi}_{SC} + \alpha_{EC}^0\,\tilde{\phi}_{EC} + \alpha_{NC}^0\,\tilde{\phi}_{NC} + \alpha_{WC}^0\,\tilde{\phi}_{WC} \tag{A.53}$$

where the coefficients are

$$\begin{aligned} \alpha_{SW}^0 &= e^{Ah+Bk}D_0 & \alpha_{SC}^0 &= e^{Bk}D_1 \\ \alpha_{SE}^0 &= e^{-Ah+Bk}D_0 & \alpha_{EC}^0 &= e^{-Ah}D_2 \\ \alpha_{NE}^0 &= e^{-Ah-Bk}D_0 & \alpha_{NC}^0 &= e^{-Bk}D_1 \\ \alpha_{NW}^0 &= e^{Ah-Bk}D_0 & \alpha_{WC}^0 &= e^{Ah}D_2 \end{aligned} \tag{A.54}$$

with

$$D_0 = \frac{1}{2}\left(E_1 + E_1^{'}\right) - Ah\coth AhE_2 - Bk\coth BkE_2^{'} \tag{A.55}$$

$$D_1 = 2Ah \coth Ah \cosh AhE_2 \tag{A.56}$$

$$D_2 = 2Bk \coth Bk \cosh BkE_2' \tag{A.57}$$

Since $\tilde{\phi} = 1$ and $\tilde{\phi} = -Bx + Ay$ are solutions of equation (A.4), and both of them can be represented by the exponential and linear boundary functions (A.5), we use the solutions to obtain functions of the infinite series analytically:

$$\frac{1}{2}\left(E_1 + E_1'\right) = \frac{1}{4\cosh Ah \cosh Bk} \tag{A.58}$$

$$E_2' - E_2\left(\frac{h}{k}\right)^2 = \frac{Ak \tanh Bk - Bh \tanh Ah}{4AkBk \cosh Ah \cosh Bk} \tag{A.59}$$

Note that now we are left to evaluate only one series summation, E_2 or E_2'.

For the general case $S \neq 0$, i.e. $\tilde{\phi} \neq \phi$, the local analytic solution can be obtained by substituting $\tilde{\phi}$ of equation (A.3) into equation (A.53), to obtain

$$\begin{aligned}\phi^0 = {} & \alpha_{SW}^0 \phi_{SW} + \alpha_{SE}^0 \phi_{SE} + \alpha_{NE}^0 \phi_{NE} + \alpha_{NW}^0 \phi_{NW} \\ & + \alpha_{SC}^0 \phi_{SC} + \alpha_{EC}^0 \phi_{EC} + \alpha_{NC}^0 \phi_{NC} + \alpha_{WC}^0 \phi_{WC} - \alpha_f^0 S\end{aligned} \tag{A.60}$$

where

$$\begin{aligned}\alpha_f^0 = {} & \frac{1}{2\left(A^2 + B^2\right)}\Big\{Ah \tanh Ah + Bk \tanh Bk - \\ & 4\cosh Ah \cosh Bk \left[(Ah)^2 E_2 + (Bk)^2 E_2'\right]\Big\}\end{aligned} \tag{A.61}$$

A.2 Interpolation procedures

Evaluation of the local analytic solution at any other point requires the evaluation of additional series and these evaluations could become computationally inefficient and/or numerically ill conditioned. To compute the local analytic solution at any other point we introduce the following approximation: we translate the origin to the point of interest, construct a smaller rectangular element, interpolate necessary values using the natural solution (A.2), and use equation (A.60) to evaluate the solution at

that point. Consider the case $0 < x < h$, $0 < y < k$, with $h_E = h - x, h_W = 2h - x$ and $h_N = k - y, h_S = 2k - y$, shown in Figure A-2 as an example.

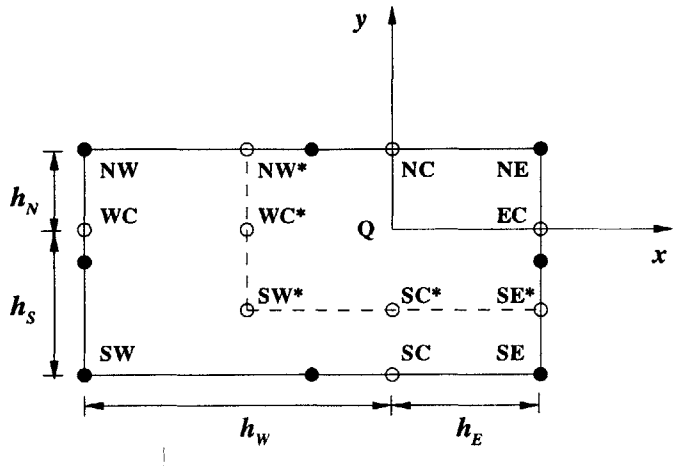

Figure A-2: Rectangular element showing translation of axis.

A smaller rectangular element of width $2h_E \times 2h_N$ and with interior point Q located at the center is drawn as shown. Equation (A.60) can then be written in terms of nodal stared values on the smaller rectangular element as follows

$$\begin{aligned}\phi_Q = {} & \alpha^0_{SW}\,\phi^*_{SW} + \alpha^0_{SE}\,\phi^*_{SE} + \alpha^0_{NE}\,\phi_{NE} + \alpha^0_{NW}\,\phi^*_{NW} \\ & + \alpha^0_{SC}\,\phi^*_{SC} + \alpha^0_{EC}\,\phi_{EC} + \alpha^0_{NC}\,\phi_{NC} + \alpha^0_{WC}\,\phi^*_{WC} - \alpha^0_f\,S\end{aligned} \tag{A.62}$$

where the coefficients are defined in equations (A.54) and (A.61), and used with $h = h_E$ and $k = h_N$. If suitable interpolation functions are employed to approximate the unknown stared values in terms of known values at the boundary, equation (A.62) can be used to obtain the solution at point Q.

Although there are several interpolation functions that could be used to approximate the stared values, the same exponential and linear functions suggested by the natural solution (A.2) are employed as interpolation functions to obtain the unknown values on the smaller rectangular element. For example the north boundary condition

is now approximated by

$$\tilde{\phi}_N(x) = a_N^* \left(e^{2Ax} - 1\right) + b_N^* x + c_N^* \tag{A.63}$$

where

$$\begin{aligned}
a_N^* &= \frac{h_W \phi_{NE} + h_E \phi_{NW} - (h_E + h_W)\,\phi_{NC}}{h_W \left(e^{2Ah_E} - 1\right) + h_E \left(e^{2Ah_W} - 1\right)} \\
b_N^* &= \frac{\left(e^{-2Ah_W} - 1\right)(\phi_{NE} - \phi_{NC}) + \left(e^{2Ah_E} - 1\right)(\phi_{NW} - \phi_{NC})}{h_W \left(e^{2Ah_E} - 1\right) + h_E \left(e^{2Ah_W} - 1\right)} \\
c_N^* &= \phi_{NC}
\end{aligned} \tag{A.64}$$

The interpolated stared value ϕ_{NW}^* can be obtained by simply evaluating the boundary function (A.63) at $x = -h_E$, to obtain

$$\phi_{NW}^* = (s-1)\,\phi_{NE} + \bar{s}\,\phi_{NW} + (2 - s - \bar{s})\,\phi_{NC} \tag{A.65}$$

where

$$s = \frac{h_W \left(e^{2Ah_E} + e^{-2Ah_E} - 2\right)}{h_W \left(e^{2Ah_E} - 1\right) + h_E \left(e^{-2Ah_W} - 1\right)}, \qquad \bar{s} = s\frac{h_E}{h_W} \tag{A.66}$$

Similar exponential and linear boundary functions can also be employed to obtain the other stared values. By substituting the interpolated values into equation (A.62) we obtain the local analytic solution at point Q.

$$\begin{aligned}
\phi_Q = {} & \alpha_{SW}\,\phi_{SW} + \alpha_{SE}\,\phi_{SE} + \alpha_{NE}\,\phi_{NE} + \alpha_{NW}\,\phi_{NW} \\
& + \alpha_{SC}\,\phi_{SC} + \alpha_{EC}\,\phi_{EC} + \alpha_{NC}\,\phi_{NC} + \alpha_{WC}\,\phi_{WC} - \alpha_f\,S
\end{aligned} \tag{A.67}$$

where

$$
\begin{aligned}
G\,\alpha_{SW} &= \bar{s}\,\bar{t}\,\alpha^0_{SW} \\
G\,\alpha_{SE} &= \bar{t}\,\alpha^0_{SE} + \bar{t}\,(s-1)\,\alpha^0_{SW} \\
G\,\alpha_{NE} &= \alpha^0_{NE} + (s-1)\,\alpha^0_{NW} + (t-1)\,\alpha^0_{SE} + (s-1)\,(t-1)\,\alpha^0_{SW} \\
G\,\alpha_{NW} &= \bar{s}\,\alpha^0_{NW} + \bar{s}\,(t-1)\,\alpha^0_{SW} \\
G\,\alpha_{SC} &= \bar{t}\,\alpha^0_{SC} + \bar{t}\,(2-s-\bar{s})\,\alpha^0_{SW} \\
G\,\alpha_{EC} &= \alpha^0_{EC} + (s-1)\,\alpha^0_{WC} + (2-t-\bar{t})\,\alpha^0_{SE} + (s-1)\,(2-t-\bar{t})\,\alpha^0_{SW} \\
G\,\alpha_{NC} &= \alpha^0_{NC} + (t-1)\,\alpha^0_{SC} + (2-s-\bar{s})\,\alpha^0_{NW} + (t-1)\,(2-s-\bar{s})\,\alpha^0_{SW} \\
G\,\alpha_{WC} &= \bar{s}\,\alpha^0_{WC} + \bar{s}\,(2-t-\bar{t})\,\alpha^0_{SW} \\
G\,\alpha_f &= \alpha^0_f \\
G &= 1 - (2-s-\bar{s})\,\alpha^0_{WC} - (2-t-\bar{t})\,\alpha^0_{SC} \\
&\quad - (2-s-\bar{s})\,(2-t-\bar{t})\,\alpha^0_{SW}
\end{aligned}
$$

and

$$
t = \frac{h_S\left(e^{2Ah_N} + e^{-2Ah_N} - 2\right)}{h_S\left(e^{2Ah_N} - 1\right) + h_N\left(e^{-2Ah_S} - 1\right)}, \qquad \bar{t} = t\frac{h_N}{h_S} \tag{A.68}
$$

Expressions for the cases $h_E > h_W$ and/or $h_N > h_S$ can be easily constructed by renaming nodal points. In this fashion we can compute the local analytic solution at any point on the element.

Appendix B

Curvilinear coordinates

In practical implementations of the finite element method, the test and trial functions are constructed, differentiated, and integrated in a mapped space. In this appendix we develop tools to construct the local analytic solution in this curvilinear space. Note that in the following we will use $u(i)$ to denote the cartesian velocity components, superscripts and subscripts will be reserved for contravariant and covariant components respectively unless otherwise stated. Superscripts will be used for coordinate components unless otherwise stated.

Our focus is not to present a detailed analysis of vector and tensor operations in the curvilinear space, but rather to review and to use available results. To this end we repeatedly refer to the work of Chung [31] and Richmond et al. [32] throughout this appendix.

In general, orthogonal coordinates are not the most convenient or efficient for numerical solutions. One can introduce an analytic or numerical transformation which simplifies the computational domain. We seek a transformation from the orthogonal coordinate system (x^i), in which the geometrically distorted element is located, to a simple square domain with equal grid spacing, which we take as the bi-unit square $[-1,1] \times [-1,1]$, in the computational space (ξ^i).

We show that the local analytic coefficients can still be used in this space, but

with the following new definitions for the independent parameters:

$$A = \frac{a_P^1}{\sqrt{g_P^{11}}}, \qquad B = \frac{a_P^2}{\sqrt{g_P^{22}}} \tag{B.1}$$

with

$$2a^m = \mathrm{Pe}\frac{\partial \xi^m}{\partial x^n}u(n) - \frac{1}{J}\frac{\partial}{\partial \xi^p}\left(Jg^{mp}\right) \tag{B.2}$$

and

$$h = \frac{1}{\sqrt{g_P^{11}}}, \qquad k = \frac{1}{\sqrt{g_P^{22}}} \tag{B.3}$$

B.1 Basic Definitions and Properties

We consider a proper transformation of the form

$$\xi^i = \xi^i\left(x^1, x^2, x^3\right)$$

By a proper transformation, we understand that the transformation is reversible, so that we can solve for x^i, giving

$$x^i = x^i\left(\xi^1, \xi^2, \xi^3\right)$$

Since the transformation is reversible the determinant of the transformation is not zero. It is important to develop tools to work in this new curvilinear coordinate system. We define the covariant base vector as

$$\mathbf{g}_i = \frac{\partial \mathbf{r}}{\partial \xi^i} = \frac{\partial x^m}{\partial \xi^i}\mathbf{i}_m \tag{B.4}$$

and its reciprocal, the contravariant base vector as

$$\mathbf{g}^i = \frac{\partial \xi^i}{\partial x^m}\mathbf{i}_m \tag{B.5}$$

The determinant of the transformation or Jacobian J is given by

$$J = \mathbf{g}_1 \cdot (\mathbf{g}_2 \times \mathbf{g}_3) \tag{B.6}$$

We define the permutation tensor e_{ijk} as:

$$e_{ijk} = \mathbf{g}_i \cdot (\mathbf{g}_j \times \mathbf{g}_k) = \begin{cases} J & \text{if even permutation} \\ -J & \text{if odd permutation} \\ 0 & \text{if any two indices are equal} \end{cases} \tag{B.7}$$

For convenience we introduce the alternating tensor ϵ_{ijk}, defined as:

$$\epsilon_{ijk} = \frac{e_{ijk}}{J} = \frac{1}{J}\,\mathbf{g}_i \cdot (\mathbf{g}_j \times \mathbf{g}_k) = \begin{cases} 1 & \text{if even permutation} \\ -1 & \text{if odd permutation} \\ 0 & \text{if any two indices are equal} \end{cases} \tag{B.8}$$

The contravariant base vectors $\mathbf{g}^i$ are orthogonal to the planes constructed by the covariant base vectors $\mathbf{g}_i$, this requires:

$$\mathbf{g}_i \cdot \mathbf{g}^j = \delta_i^j = \begin{cases} 1 & \text{if } i = j \\ 0 & \text{if } i \neq j \end{cases} \tag{B.9}$$

The set of contravariant base vectors can also be defined in the following manner:

$$\mathbf{g}^i = \frac{1}{J}\,\mathbf{g}_j \times \mathbf{g}_k \tag{B.10}$$

which are clearly orthogonal to the planes constructed by the covariant basis. For convenience, let

$$\mathbf{b}^i = J\,\mathbf{g}^i = \mathbf{g}_j \times \mathbf{g}_k \tag{B.11}$$

So that the lth component of the ith contravariant vector $\mathbf{b}^i$ can be written as [32]:

$$b_l^i = J\,\frac{\partial \xi^i}{\partial x^l} = \epsilon_{lmn}\,\frac{\partial x^m}{\partial \xi^j}\frac{\partial x^n}{\partial \xi^k} = \frac{\partial x^m}{\partial \xi^j}\frac{\partial x^n}{\partial \xi^k} - \frac{\partial x^n}{\partial \xi^j}\frac{\partial x^l}{\partial \xi^k} \tag{B.12}$$

with i, j, k and l, m, n in cyclic order.

We also define g_{ij} and g^{ij} as the covariant and contravariant metric tensors respectively:

$$g_{ij} = \mathbf{g}_i \cdot \mathbf{g}_j = \frac{\partial x^m}{\partial \xi^i} \frac{\partial x^m}{\partial \xi^j} \tag{B.13}$$

$$g^{ij} = \mathbf{g}^i \cdot \mathbf{g}^j = \frac{\partial \xi^i}{\partial x^m} \frac{\partial \xi^j}{\partial x^m} \tag{B.14}$$

The determinants of the metric tensors are both positive and equal to

$$\det\left(g_{ij}\right) = g = J^2 \tag{B.15}$$

$$\det\left(g^{ij}\right) = \frac{1}{g} = \frac{1}{J^2} \tag{B.16}$$

We also note the additional properties obtained by using equations (B.4), (B.5), (B.13), and (B.14); which we do not prove here but refer to the proofs of Chung [31] and Richmond et al. [32].

$$\mathbf{g}_i = g_{ij}\mathbf{g}^j \tag{B.17}$$

$$\mathbf{g}^i = g^{ij}\mathbf{g}_j \tag{B.18}$$

$$g_{ik}\, g^{kj} = \delta_i^j \tag{B.19}$$

The contravariant metric tensor g^{ij} is the inverse of g_{ij} or the adjoint of g_{ij} divided by the determinant of g_{ij} (Cramer's rule) [31, 32]:

$$g^{ij} = \frac{1}{g} \frac{\partial g}{\partial g_{ij}} = \frac{1}{J^2} \left(g_{mp} g_{nq} - g_{mq} g_{np}\right) \tag{B.20}$$

with i, m, n and j, p, q in cyclic order.

B.2 Covariant Differentiation

Now consider the derivatives of the covariant base vectors:

$$\mathbf{g}_{i,j} = \frac{\partial \mathbf{g}_i}{\partial \xi^j} = \frac{\partial}{\partial \xi^j}\left(\frac{\partial x^m}{\partial \xi^i}\mathbf{i}_m\right) = \frac{\partial^2 x^m}{\partial \xi^j \partial \xi^i}\frac{\partial \xi^n}{\partial x^m}\mathbf{g}_n = \Gamma^n_{ij}\mathbf{g}_n \tag{B.21}$$

where Γ^n_{ij} is called the Christoffel symbol of the second kind [31, 32], defined as:

$$\Gamma^n_{ij} = \frac{\partial^2 x^m}{\partial \xi^j \partial \xi^i}\frac{\partial \xi^n}{\partial x^m} = x^m_{,ij}\frac{\partial \xi^n}{\partial x^m} \tag{B.22}$$

Making use of equation (B.19), we note that

$$\frac{\partial}{\partial \xi^i}\left(\mathbf{g}^j \cdot \mathbf{g}_k\right) = \mathbf{g}_k \cdot \mathbf{g}^j_{,i} + \mathbf{g}^j \cdot \mathbf{g}_{k,i} = 0 \tag{B.23}$$

or

$$\mathbf{g}_k \cdot \mathbf{g}^j_{,i} = -\mathbf{g}^j \cdot \mathbf{g}_{k,i} = -\mathbf{g}^j \cdot \mathbf{g}_n \Gamma^n_{ki} = -\Gamma^j_{ki} \tag{B.24}$$

Thus, the derivative of contravariant base vectors is of the form

$$\frac{\partial \mathbf{g}^j}{\partial \xi^i} = \mathbf{g}^j_{,i} = -\Gamma^j_{ik}\mathbf{g}^k \tag{B.25}$$

The Christoffel symbol of the second kind is related to the Jacobian as:

$$\begin{aligned}
\frac{\partial J}{\partial \xi^i} &= \frac{\partial \mathbf{g}_1}{\partial \xi^i} \cdot (\mathbf{g}_2 \times \mathbf{g}_3) + \mathbf{g}_1 \left(\frac{\partial \mathbf{g}_2}{\partial \xi^i} \times \mathbf{g}_3 + \mathbf{g}_2 \times \frac{\partial \mathbf{g}_3}{\partial \xi^i}\right) \\
&= \Gamma^j_{1i}\,\mathbf{g}_j \cdot (\mathbf{g}_2 \times \mathbf{g}_3) + \Gamma^j_{2i}\,\mathbf{g}_1 \cdot (\mathbf{g}_j \times \mathbf{g}_3) + \Gamma^j_{3i}\,\mathbf{g}_1 \cdot (\mathbf{g}_2 \times \mathbf{g}_j) \\
&= \Gamma^j_{1i}\,e_{j23} + \Gamma^j_{2i}\,e_{ij3} + \Gamma^j_{3i}\,e_{i2j} \\
&= \Gamma^j_{1i}\,J + \Gamma^j_{2i}\,J + \Gamma^j_{3i}\,J \\
&= J\,\Gamma^j_{ji}
\end{aligned} \tag{B.26}$$

B.3 Operations in Curvilinear Form

With the foregoing tensor analysis tools, we are ready to recast the usual operations for any dependent variable ϕ in curvilinear tensor form. Using the chain rule we can write:

$$\frac{\partial \phi}{\partial x^i} = \frac{\partial \xi^l}{\partial x^i}\frac{\partial \phi}{\partial \xi^l} \tag{B.27}$$

making use of equation (B.12) yields:

$$\frac{\partial \phi}{\partial x^i} = \frac{1}{J} b_i^l \frac{\partial \phi}{\partial \xi^l} = \frac{1}{J}\left(\frac{\partial x^j}{\partial \xi^m}\frac{\partial x^k}{\partial \xi^n} - \frac{\partial x^k}{\partial \xi^m}\frac{\partial x^i}{\partial \xi^n}\right)\frac{\partial \phi}{\partial \xi^l} \tag{B.28}$$

with i, j, k and l, m, n in cyclic order. Next we consider the second derivative:

$$\begin{aligned}
\frac{\partial^2 \phi}{\partial x^m \partial x^m} &= \frac{\partial \xi^j}{\partial x^m}\frac{\partial}{\partial \xi^j}\left(\frac{\partial \xi^i}{\partial x^m}\frac{\partial \phi}{\partial \xi^i}\right) \\
&= \mathbf{g}^j \frac{\partial}{\partial \xi^j} \cdot \mathbf{g}^i \frac{\partial \phi}{\partial \xi^i} \\
&= \mathbf{g}^j \cdot \mathbf{g}^i_{,j}\phi_{,i} + \mathbf{g}^j \cdot \mathbf{g}^i \phi_{,ij} \\
&= \mathbf{g}^j \cdot \left(g^{ik}\mathbf{g}_k\right)_{,j}\phi_{,i} + g^{ij}\phi_{,ij} \\
&= \left(\mathbf{g}^j \cdot g^{ik}_{,j}\mathbf{g}_k + \mathbf{g}^j \cdot g^{ik}\mathbf{g}_{k,j}\right)\phi_{,i} + g^{ij}\phi_{,ij} \\
&= g^{ij}_{,j}\phi_{,i} + \mathbf{g}^j \cdot g^{ik}\Gamma^l_{jk}\mathbf{g}_l\phi_{,i} + g^{ij}\phi_{,ij} \\
&= g^{ik}\Gamma^j_{jk}\phi_{,i} + g^{ij}\phi_{,ij} \\
&= g^{ij}\Gamma^k_{ki}\phi_{,j} + g^{ij}\phi_{,ij} \\
&= g^{ij}\phi_{,ij} + g^{ij}\frac{1}{J}\frac{\partial J}{\partial \xi^i}\phi_{,j} \\
&= g^{ij}\frac{\partial^2 \phi}{\partial \xi^i \partial \xi^j} + \frac{1}{J}\frac{\partial}{\partial \xi^i}\left(J g^{ij}\right)\frac{\partial \phi}{\partial \xi^j}
\end{aligned} \tag{B.29}$$

Where we made repeated use of the identity $g^{ij}_{,i} = g^{ij}_{,j} = 0$ [31].

B.4 Partial Transformation

Making use of equations (B.27) and (B.29), the advection-diffusion equation becomes

$$\frac{1}{\mathrm{Pe}}\left[g^{mn}\frac{\partial^2\phi}{\partial\xi^m\partial\xi^n}+\frac{1}{J}\frac{\partial}{\partial\xi^p}\left(Jg^{mp}\right)\frac{\partial\phi}{\partial\xi^m}\right]=U(n)\frac{\partial\xi^m}{\partial x^n}\frac{\partial\phi}{\partial\xi^m}+F \tag{B.30}$$

a rearrangement of the above yields

$$g^{mn}\frac{\partial^2\phi}{\partial\xi^m\partial\xi^n}-\left[\mathrm{Pe}\,\frac{\partial\xi^m}{\partial x^n}u(n)-\frac{1}{J}\frac{\partial}{\partial\xi^p}\left(Jg^{mp}\right)\right]\frac{\partial\phi}{\partial\xi^m}=F \tag{B.31}$$

where F has been suitably modified. Now, let

$$2a^m=\mathrm{Pe}\,\frac{\partial\xi^m}{\partial x^n}u(n)-\frac{1}{J}\frac{\partial}{\partial\xi^p}\left(Jg^{mp}\right) \tag{B.32}$$

Then, we can write

$$g^{mn}\frac{\partial^2\phi}{\partial\xi^m\partial\xi^n}-2a^m\frac{\partial\phi}{\partial\xi^m}=F \tag{B.33}$$

or equivalently

$$\begin{aligned} g^{mm}\frac{\partial^2\phi}{\partial\xi^m\partial\xi^m} \quad - \quad 2a^m\frac{\partial\phi}{\partial\xi^m} &= F - \\ & 2\left(g^{12}\frac{\partial^2\phi}{\partial\xi^1\partial\xi^2}+g^{13}\frac{\partial^2\phi}{\partial\xi^1\partial\xi^3}+g^{23}\frac{\partial^2\phi}{\partial\xi^2\partial\xi^3}\right) \end{aligned} \tag{B.34}$$

Now, we define

$$S=F-2\left(g^{12}\frac{\partial^2\phi}{\partial\xi^1\partial\xi^2}+g^{13}\frac{\partial^2\phi}{\partial\xi^1\partial\xi^3}+g^{23}\frac{\partial^2\phi}{\partial\xi^2\partial\xi^3}\right) \tag{B.35}$$

And so the advection-diffusion equation can be written as

$$g^{mm}\frac{\partial^2\phi}{\partial\xi^m\partial\xi^m}=2a^m\frac{\partial\phi}{\partial\xi^m}+S \tag{B.36}$$

Making use of equation (B.12) we rewrite $2a^m$ as

$$2a^m = \frac{\mathrm{Pe}}{J} b_n^m u(n) - \frac{1}{J}\frac{\partial}{\partial \xi^p}\left(J g^{mp}\right) \tag{B.37}$$

Note that we have only performed a partial transformation, i.e., the velocity components are still referenced in the cartesian coordinate system.

The geometric coefficients b_n^m, J, and g^{mn} given by equations (B.12), (B.15), and (B.20) are functions of the coordinates only. When either analytic or numerical transformations are employed their values can be readily evaluated.

B.5 Local Analytic Solution

In the following $\xi^1 = \xi$ and $\xi^2 = \eta$. We locally linearize equation (B.36) in each rectangular numerical element by taking representative values of the velocity field, source function, and geometric coefficients – say the value at the center of the element.

$$g_P^{11}\frac{\partial^2 \phi}{\partial \xi^2} + g_P^{22}\frac{\partial^2 \phi}{\partial \eta^2} = 2a_P^1\frac{\partial \phi}{\partial \xi} + 2a_P^2\frac{\partial \phi}{\partial \eta} + S_P \tag{B.38}$$

Introducing the coordinate stretching functions:

$$\xi^* = \frac{\xi}{\sqrt{g_P^{11}}}, \qquad \eta^* = \frac{\eta}{\sqrt{g_P^{22}}} \tag{B.39}$$

equation (B.38) is simplified to the standard form seen in equation (A.1), i.e.,

$$\frac{\partial^2 \phi}{\partial \xi^{*2}} + \frac{\partial^2 \phi}{\partial \eta^{*2}} = 2A\frac{\partial \phi}{\partial \xi^*} + 2B\frac{\partial \phi}{\partial \eta^*} + S_P \tag{B.40}$$

where

$$A = \frac{a_P^1}{\sqrt{g_P^{11}}}, \qquad B = \frac{a_P^2}{\sqrt{g_P^{22}}} \tag{B.41}$$

for a numerical element with dimensions

$$\Delta\xi^* = h = \frac{1}{\sqrt{g_P^{11}}}, \qquad \Delta\eta^* = k = \frac{1}{\sqrt{g_P^{22}}} \tag{B.42}$$

Appendix C

Variational formulation for the S-LAPG scheme

In this appendix we derive the variational form of the Navier-Stokes equations used in the simplified version of the Local Analytic/Petrov-Galerkin (S-LAPG) discretization scheme. As usual we multiply the Navier-Stokes equation with a test function, however we express the test function as the sum of two test functions $\mathbf{a} = \mathbf{v} + \mathbf{w}$.

$$\int_{\Omega} \left\{ \frac{\partial \mathbf{u}}{\partial t} + (\mathbf{u} \cdot \nabla)\,\mathbf{u} + \nabla p - \frac{1}{\mathrm{Re}} \nabla \cdot \left[(\nabla \mathbf{u}) + (\nabla \mathbf{u})^T \right] - \mathbf{f} \right\} \cdot \mathbf{a}\, d\Omega = 0 \qquad \text{(C.1)}$$

or equivalently

$$\int_{\Omega} \left\{ \frac{\partial \mathbf{u}}{\partial t} + (\mathbf{u} \cdot \nabla)\,\mathbf{u} + \nabla p - \frac{1}{\mathrm{Re}} \nabla \cdot \left[(\nabla \mathbf{u}) + (\nabla \mathbf{u})^T \right] - \mathbf{f} \right\} \cdot (\mathbf{v} + \mathbf{w})\, d\Omega = 0 \quad \text{(C.2)}$$

In equation (C.2) the test functions $\mathbf{v}$ and $\mathbf{w}$ are not applied independently, but together as $\mathbf{v} + \mathbf{w}$. We now require that $\mathbf{v} \in \mathbf{H}^1(\Omega)$ and $\mathbf{v}|_{\Gamma_u} = 0$ so that we may apply integration by parts together with the Gauss divergence theorem to obtain:

$$\int_\Omega \left[\frac{\partial \mathbf{u}}{\partial t} + (\mathbf{u}\cdot\nabla)\,\mathbf{u}\right]\cdot \mathbf{v}\, d\Omega - \int_\Omega p\ (\nabla\cdot\mathbf{v})\ d\Omega$$
$$+ \frac{1}{\mathrm{Re}}\int_\Omega \left[(\nabla\mathbf{u}) + (\nabla\mathbf{u})^T\right]\cdot\nabla\mathbf{v}\, d\Omega$$
$$+ \int_\Omega \left[\frac{\partial \mathbf{u}}{\partial t} + (\mathbf{u}\cdot\nabla)\,\mathbf{u} + \nabla p - \frac{1}{\mathrm{Re}}\nabla^2\mathbf{u}\right]\cdot\mathbf{w}\, d\Omega$$
$$= \int_\Omega \mathbf{f}\cdot\mathbf{v}\, d\Omega + \int_\Omega \mathbf{f}\cdot\mathbf{w}\, d\Omega + \int_{\Gamma_f} \mathbf{f}^s\cdot\mathbf{v}\, d\Gamma_f \qquad \text{(C.3)}$$

Note that in arriving at equation (C.3) we made use of the incompressibility constraint, $\nabla\cdot\mathbf{u} = 0$, in

$$\nabla\cdot\left[(\nabla\mathbf{u}) + (\nabla\mathbf{u})^T\right] = \nabla^2\mathbf{u} + \nabla\,(\nabla\cdot\mathbf{u}) = \nabla^2\mathbf{u} \qquad \text{(C.4)}$$

We do this for convenience, since no boundary terms involving the test function $\mathbf{w}$ arose in the variational form. See Chapter 2 for an explanation of why the term $\nabla\cdot\left[(\nabla\mathbf{u}) + (\nabla\mathbf{u})^T\right]$ is retained in its entirety when boundary terms arise.

In equation (C.3) we require that $\mathbf{w}\in\mathbf{H}^0$ and since $\mathbf{w}$ does not come into the boundary terms we may have that $\mathbf{w}|_\Gamma = 0$, although not required. Hence, we avoid differentiation of the test function $\mathbf{w}$ but retain its effect in the variational form. Note that if we set $\mathbf{w} = 0$ we recover the variational formulation derived in Chapter 2. Also note that this variational form contains second order derivatives, which in the finite element discretization do not disappear since we are using biquadratic functions to approximate $\mathbf{u}$.

The Navier-Stokes equations in differential form, which can be obtained from equation (C.2), can be easily recovered by using equation (C.4) in (C.3) and then applying integration by parts together with the Gauss divergence theorem to equation (C.3).

Appendix D

One-dimensional discrete equations using the FCBI scheme

In this appendix we give discrete equations for the one-dimensional advection-diffusion equation using linear-exponential test functions, of the form given in equation (3.46), and quadratic trial functions.

Consider the one-dimensional stationary advection-diffusion equation for the transported scalar $\theta(x)$ in dimensionless form:

$$-\frac{1}{\mathrm{Pe}}\frac{d^2\theta}{dx^2}+\frac{d\theta}{dx}=0 \qquad \text{in } \Omega, \qquad \theta|_{\Gamma_\theta}=\theta^s \tag{D.1}$$

where $\Omega \in R^1$, $\mathrm{Pe}=uL/\alpha$ is the Peclet number, L is the length of the domain, u is the prescribed fluid velocity, α is the diffusivity of the transported scalar θ, and θ^s is the prescribed value of θ on the boundary Γ_θ. Here we consider the case where no fluxes are prescribed on the boundary, i.e. $\Gamma_f=\varnothing$. The variational form of the equation using the Petrov-Galerkin formulation is:

Find $\theta \in \Theta$ such that for all $v \in V$

$$\frac{1}{\mathrm{Pe}}\int_\Omega \frac{d\theta}{dx}\frac{dv}{dx}+\frac{d\theta}{dx}v\,d\Omega=0 \tag{D.2}$$

where

$$\Theta = \left\{\theta \in H^1(\Omega), \theta|_{\Gamma_\theta} = \theta^s\right\}$$

$$V = \left\{v \in H^1(\Omega), v|_{\Gamma_\theta} = 0\right\}$$

and different functions are used in Θ and V.

For the finite element solution we choose subspaces Θ_h and V_h of the infinite-dimensional spaces Θ and V respectively. Specifically, for Θ_h we choose quadratic functions and for V_h the linear-exponential functions described in Chapter 3. Upon spatial discretization, integration, and proper assembly we obtain the discrete equation for the ith node. In this case there will be two types of discrete equations, one relating three nodal variables and the other relating five nodal variables. This is a direct consequence of the use of 3-node elements.

First we consider the discrete equation relating three nodal variables. Here we present the discrete equations for the case of distance h between nodes and flow in the positive x direction, i.e. $u > 0$.

$$\left(\frac{1}{\mathrm{Pe}^e} a_1 + b_1\right)\theta_{i-1} + \left(\frac{1}{\mathrm{Pe}^e} a_2 + b_2\right)\theta_i + \left(\frac{1}{\mathrm{Pe}^e} a_3 + b_3\right)\theta_{i+1} = 0 \qquad \text{(D.3)}$$

where $\mathrm{Pe}^e = uh/\alpha$ is the element Peclet number and the coefficients a_j, b_j $(j = 1, 2, 3)$ are functions of the element Peclet number. The coefficients a_j represent the diffusion effect and the coefficients b_j the advection effect, compare equations (D.2) and (D.3). The expressions for these coefficients are not very compact and a better feel for their behavior can be obtained by plotting them. Figures D-1 and D-2 show the coefficients as a function of the element Peclet number.

For the case of advection dominated flows, $\mathrm{Pe}^e \to \infty$, the discrete equation becomes

$$\theta_i = \frac{5}{4}\theta_{i-1} - \frac{1}{4}\theta_{i+1} \qquad \text{(D.4)}$$

which reveals a positive weight of 1.25 for the upstream node and a negative weight of 0.25 for the downstream node. For the case of pure diffusion, $\mathrm{Pe}^e \to 0$, the

test functions collapse to the quadratic functions and we recover the classic Bubnov-Galerkin quadratic approximation

$$\theta_i = \frac{1}{2}\left(\theta_{i-1} + \theta_{i+1}\right) \tag{D.5}$$

For completeness, we give the expressions for the coefficients a_j and b_j in terms of $Ah = \mathrm{Pe}^e/2$. Expressions for the coefficients a_j are:

$$\begin{aligned} a_1 = e^{2Ah}\big\{e^{-4Ah}\left(-Ah-1\right) + e^{-2Ah}\left[4Ah\cosh(Ah)\sinh(Ah)\right] \\ - 3Ah + 1\big\} \,/\, 4Ah\left[\cosh^2(Ah) - 1\right] \end{aligned} \tag{D.6}$$

$$a_2 = e^{2Ah}\big\{e^{-4Ah}\left(2Ah+1\right) + 2Ah + 1\big\} \,/\, 2Ah\left[\cosh^2(Ah) - 1\right] \tag{D.7}$$

$$\begin{aligned} a_3 = -e^{2Ah}\big\{e^{-4Ah}\left(3Ah+1\right) + e^{-2Ah}\left[4Ah\cosh(Ah)\sinh(Ah)\right] \\ + Ah - 1\big\} \,/\, 4Ah\left[\cosh^2(Ah) - 1\right] \end{aligned} \tag{D.8}$$

and for the coefficients b_j:

$$\begin{aligned} b_1 = -e^{2Ah}\big\{e^{-4Ah}\left(-3Ah-3\right) + e^{-2Ah}\big[16(Ah)^2\cosh(Ah)\sinh(Ah) \\ + 24(Ah)^2\cosh^2(Ah) - 12(Ah)^2\big] - 9Ah + 3\big\} \,/\, 24(Ah)^2\left[\cosh^2(Ah) - 1\right] \end{aligned} \tag{D.9}$$

$$\begin{aligned} b_2 = e^{2Ah}\big\{e^{-4Ah}\left(-6Ah-3\right) + e^{-2Ah}\left[16(Ah)^2\cosh(Ah)\sinh(Ah)\right] \\ - 6Ah + 3\big\} \,/\, 12(Ah)^2\left[\cosh^2(Ah) - 1\right] \end{aligned} \tag{D.10}$$

$$\begin{aligned} b_3 = e^{2Ah}\big\{e^{-4Ah}\left(9Ah+3\right) + e^{-2Ah}\big[-16(Ah)^2\cosh(Ah)\sinh(Ah) \\ + 24(Ah)^2\cosh^2(Ah) - 12(Ah)^2\big] + 3Ah - 3\big\} \,/\, 24(Ah)^2\left[\cosh^2(Ah) - 1\right] \end{aligned} \tag{D.11}$$

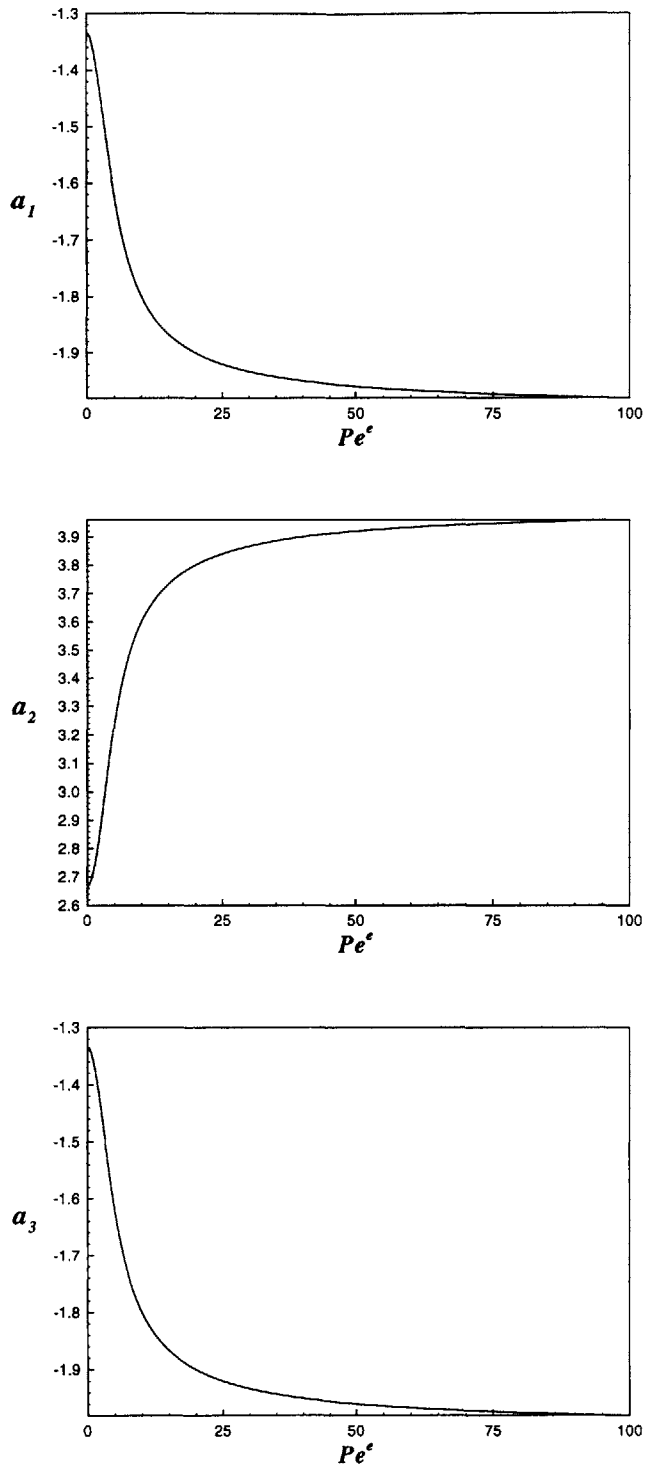

Figure D-1: a_j coefficients as a function of the element Peclet number.

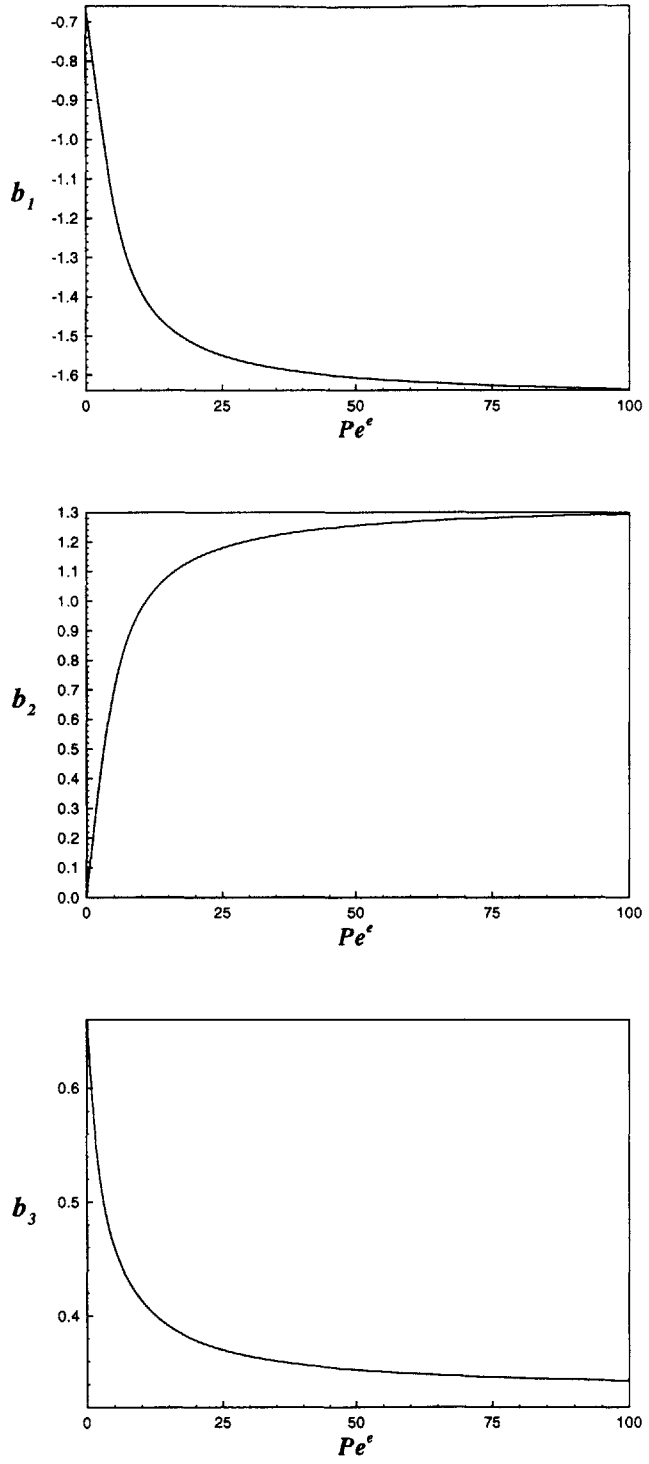

Figure D-2: b_j coefficients as a function of the element Peclet number.

Next, we present the discrete equation relating five nodal variables. Again, we consider the case of unit distance between nodes and flow in the positive x direction.

$$\left(\frac{1}{\mathrm{Pe}}\,e_1 + f_1\right)\theta_{i-2} + \left(\frac{1}{\mathrm{Pe}}\,e_2 + f_2\right)\theta_{i-1} + \left(\frac{1}{\mathrm{Pe}}\,e_3 + f_3\right)\theta_i + \left(\frac{1}{\mathrm{Pe}}\,e_4 + f_4\right)\theta_{i+1} + \left(\frac{1}{\mathrm{Pe}}\,e_5 + f_5\right)\theta_{i+2} = 0 \tag{D.12}$$

where the coefficients e_j, f_j $(j = 1, \ldots, 5)$ are functions of the element Peclet number and represent effects from diffusion and advection respectively.

For the case of advection dominated flows, $\mathrm{Pe}^e \to \infty$, the discrete equation becomes

$$\theta_i = -\,\theta_{i-2} + 2\,\theta_{i-1} \tag{D.13}$$

which reveals a positive weight of 2.0 for the adjacent upstream node, a negative weight of 1.0 for the alternate upstream node, and no contributions from the downstream nodes. For the case of pure diffusion, $\mathrm{Pe}^e \to 0$, the test functions collapse to the quadratic functions and we recover the classic Bubnov-Galerkin quadratic approximation

$$\theta_i = \frac{1}{14}\left(-\,\theta_{i-2} + 8\,\theta_{i-1} + 8\,\theta_{i+1} - \theta_{i+2}\right) \tag{D.14}$$

Expressions for the coefficients e_j are:

$$e_1 = -e^{2Ah}\left\{e^{-4Ah}\left(-Ah - 1\right) + e^{-2Ah}\left[4Ah\cosh(Ah)\sinh(Ah) + 4Ah\cosh^2(Ah) - 4Ah\right] - 3Ah + 1\right\} / 8Ah\left[\cosh^2(Ah) - 1\right] \tag{D.15}$$

$$e_2 = -e^{2Ah}\left\{e^{-4Ah}\left(2Ah + 1\right) + 2Ah - 1\right\} / 4Ah\left[\cosh^2(Ah) - 1\right] \tag{D.16}$$

$$e_3 = e^{2Ah}\left\{e^{-4Ah}\left(4Ah + 2\right) + e^{-2Ah}\left[8Ah\cosh^2(Ah) - 8Ah\right] + 4Ah - 2\right\} / 8Ah\left[\cosh^2(Ah) - 1\right] \tag{D.17}$$

$$e_4 = -e^{2Ah}\left\{e^{-4Ah}\left(2Ah + 1\right) + 2Ah - 1\right\} / 4Ah\left[\cosh^2(Ah) - 1\right] \tag{D.18}$$

$$e_5 = e^{2Ah}\{e^{-4Ah}(3Ah+1) + e^{-2Ah}[4Ah\cosh(Ah)\sinh(Ah) - 4Ah\cosh^2(Ah) + 4Ah] + Ah - 1\} / 8Ah\left[\cosh^2(Ah) - 1\right] \quad \text{(D.19)}$$

and for the coefficients f_j:

$$f_1 = e^{2Ah}\{e^{-4Ah}(-3Ah-3) + e^{-2Ah}[16(Ah)^2\cosh(Ah)\sinh(Ah) + 16(Ah)^2\cosh^2(Ah) - 4(Ah)^2] - 9Ah + 3\} / 48(Ah)^2\left[\cosh^2(Ah) - 1\right] \quad \text{(D.20)}$$

$$f_2 = -e^{2Ah}\{e^{-4Ah}(-6Ah-3) + e^{-2Ah}[16(Ah)^2\cosh(Ah)\sinh(Ah) + 16(Ah)^2\cosh^2(Ah) - 16(Ah)^2] - 6Ah + 3\} / 24(Ah)^2\left[\cosh^2(Ah) - 1\right] \quad \text{(D.21)}$$

$$f_3 = e^{2Ah}\{e^{-4Ah}(-12Ah-6) + e^{-2Ah}\left[32(Ah)^2\cosh(Ah)\sinh(Ah)\right] - 12Ah + 6\} / 48(Ah)^2\left[\cosh^2(Ah) - 1\right] \quad \text{(D.22)}$$

$$f_4 = -e^{2Ah}\{e^{-4Ah}(-6Ah-3) + e^{-2Ah}[16(Ah)^2\cosh(Ah)\sinh(Ah) - 16(Ah)^2\cosh^2(Ah) + 16(Ah)^2] - 6Ah + 3\} / 24(Ah)^2\left[\cosh^2(Ah) - 1\right] \quad \text{(D.23)}$$

$$f_5 = e^{2Ah}\{e^{-4Ah}(-9Ah-3) + e^{-2Ah}[16(Ah)^2\cosh(Ah)\sinh(Ah) - 16(Ah)^2\cosh^2(Ah) + 4(Ah)^2] - 3Ah + 3\} / 48(Ah)^2\left[\cosh^2(Ah) - 1\right] \quad \text{(D.24)}$$

Bibliography

[1] I. Christie, O.F. Griffith, A.R. Mitchell, and O.C. Zienkiewicz. Finite element methods for second-order differential equations with significant first-order derivatives. *Int. J. Numer. Methods Engrg.*, 10:1389–1396, 1976.

[2] J.C. Heinrich, P.S. Huyakorn, and O.C. Zienkiewicz. An upwind finite element scheme for two-dimensional convective transport equation. *Int. J. Numer. Methods Engrg.*, 11:131–143, 1977.

[3] A.N. Brooks and T.J.R. Hughes. Streamline Upwind/Petrov-Galekin formulation for convection dominated flows with particular emphasis on the incompressible Navier-Stokes equations. *Comput. Methods Appl. Mech. Engrg.*, 32:199–259, 1982.

[4] T.J.R. Hughes, L.P. Franca, and G.M. Hulbert. A new finite element formulation for computational fluid dynamics: VIII the Galerkin/Least-squares method for advective-diffusive equations. *Comput. Methods Appl. Mech. Engrg.*, 73:173–189, 1989.

[5] D. Hendriana and K.J. Bathe. On upwind methods for parabolic finite elements in incompressible flows. *Int. J. Numer. Methods Engrg.*, 47:317–340, 2000.

[6] F. Brezzi, L.P. Franca, and A. Russo. Further considerations on residual-free bubbles for advective-diffusive equations. *Comput. Methods Appl. Mech. Engrg.*, 166:25–33, 1998.

[7] F. Brezzi, D. Marini, and A. Russo. Applications of the pseudo residual-free bubbles to the stabilization of convection-diffusion problems. *Comput. Methods Appl. Mech. Engrg.*, 166:51–63, 1998.

[8] K.J. Bathe. The inf-sup condition and its evaluation for mixed finite element methods. *Computers and Structures*, 79:243–252, 971, 2000.

[9] K.J. Bathe. *Finite Element Procedures.* Prentice Hall, New Jersey, 1996.

[10] J.H. Spurk. *Fluid Mechanics.* Springer-Verlag, Berlin, 1997.

[11] Alexander Rauh. Remarks on unsolved basic problems of the Navier-Stokes equations. In *Proceedings of Conference: Let's Face Chaos through Nonlinear Dynamics*, Maribor, Slovenia, 1996.

[12] J.T. Oden and J.N. Reddy. *An Introduction to the Mathematical Theory of Finite Elements.* John Wiley and Sons, New York, 1976.

[13] R. Temam. *The Navier-Stokes equations.* North-Holland, Amsterdam, 1978.

[14] O.A. Ladyzhenskaya. *The Mathenatical Theory of Viscous Incompressible Flow.* Gordon and Breach, New York, 1963.

[15] C.J. Chen and H.C. Chen. Finite analytic numerical method for unsteady two-dimensional Navier-Stokes equations. *Journal of Computational Physics*, 53:209–226, 1984.

[16] H.C. Chen, V.C. Patel, and S. Ju. Solution of Reynolds-Averaged Navier-Stokes equations for three-dimensional incompressible flows. *Journal of Computational Physics*, 88(2):305–336, 1990.

[17] Y.J. Jang, H.C. Chen, and J.C. Han. Flow and heat transfer in a rotating square channel with 45 deg angled ribs by Reynolds Stress turbulence model. *Journal of Turbomachinery*, 123:124–132, 2001.

[18] H.C. Chen. Submarine flows studied by second-moment closure. *Journal of Engineering Mechanics*, 121(10):1136–1146, 1995.

[19] F. Brezzi and D. Marini. Subgrid phenomena and numerical schemes. In *Proceedings of the International Symposium on Mathematical Modeling and Numerical Simulation in Continuum Mechanics*, Yamaguchi, 2000.

[20] F. Brezzi. Recent results in the treatment of subgrid scales. In *Actes du 32eme Congres d'Analyse Numerique*, Port d'Albret, 2000.

[21] Lloyd A. Trefethen. *Spectral Methods in Matlab.* Siam, Philadelphia, PA, 2000.

[22] P.J. Davis and P. Rabinowitz. *Methods of Numerical Integration.* Academic Press, New York, 1984.

[23] A.R. Krommer and C.W. Ueberhuber. *Computational Integration.* Siam, Philadelphia, PA, 1998.

[24] K.J. Bathe and J.P. Pontaza. A flow-conditioned-based interpolation mixed finite element procedure for high Reynolds number fluid flows. Computers and Structures, to appear.

[25] K.J. Bathe, D. Hendriana, F. Brezzi, and G. Sangalli. Inf-sup testing of upwind methods. *Int. J. Numer. Methods Engrg.*, 48:745–760, 2000.

[26] G.H. Golub and C.F. Van Loan. *Matrix Computations.* Johns Hopkins University Press, Baltimore, Maryland, 1996.

[27] U. Ghia, K.N. Ghia, and C.T. Shin. High-Re solution for incompressible flow using the Navier-Stokes equations and the multigrid method. *Journal of Computational Physics*, 48:387–411, 1982.

[28] R.L. Sani and P.M. Gresho. Resume and remarks on the open boundary contidion minisymposium. *Int. J. Numer. Methods in Fluids*, 18:983–1008, 1994.

[29] M.S. Engelman and M.A. Jamnia. Transient flow past a circular cylinder: A benchmark solution. *Int. J. Numer. Methods in Fluids*, 11:985–1000, 1990.

[30] P.M. Gresho and R.L. Sani. *Incompressible Flow and the Finite Element Method.* John Wiley and Sons, New York, 1998.

[31] T.J. Chung. *Applied Continuum Mechanics.* Cambridge University Press, New York, 1996.

[32] M.C. Richmond, H.C. Chen, and V.C. Patel. Equations of laminar and turbulent flows in general curvilinear coordinates. IIHR Report 300, Iowa Institute of Hydraulic Research, The University of Iowa, February 1986.